

**Studies on Fabrication of Silicon Thin Films
Using Plasma Enhanced Chemical Vapor Deposition
and Behaviors of Radicals**

ABE Yusuke

2013

Nagoya University

Department of Electrical Engineering and Computer Science

Chapter 1 Introduction

1.1 Trend in solar cells 1

 1.1.1 Background of photovoltaic generation 1

 1.1.2 Brief history of solar cells 2

1.2 Thin-film silicon solar cells 5

 1.2.1 Introduction of thin-film silicon solar cells 5

 1.2.2 Amorphous silicon 7

 1.2.3 Microcrystalline silicon 9

1.3 Plasma process of thin-film silicon solar cells 11

 1.3.1 Growth of a-Si:H 15

 1.3.2 Growth of $\mu\text{c-Si:H}$ 18

 1.3.3 High-rate deposition of $\mu\text{c-Si:H}$ 22

1.4 Diagnostics for activated species in the plasma 23

 1.4.1 Measurement for atomic radicals 23

 1.4.2 Measurement for molecular radicals 25

 1.4.3 Measurement for polymeric radicals 27

 1.4.4 Measurement for radical temperatures 30

 1.4.5 Measurement for radicals in SiH_4/H_2 plasma 32

1.5 Purposes and construction of this thesis 33

1.6 References 36

**Chapter 2 Plasma Diagnostic Techniques and Film
Characterization Methods**

2.1 Introduction 45

2.2 Plasma diagnostic techniques 46

Contents

2.2.1 Theory of absorption spectroscopy	46
2.2.2 VUVAS using micro-discharge hollow cathode lamp (MHCL)	48
2.2.3 VUVLAS using tunable VUV laser system	51
2.2.4 Cavity ring-down spectroscopy (CRDS)	54
2.2.5 Optical emission spectroscopy (OES)	56
2.2.6 Microwave interferometer	60
2.3 Film characterization methods	61
2.3.1 Raman spectroscopy	61
2.3.2 X-Ray diffraction (XRD)	64
2.3.3 Fourier transform infrared spectroscopy (FTIR)	66
2.3.4 Electron spin resonance (ESR)	70
2.3.5 Transmission electron microscopy (TEM)	73
2.4 References	76

Chapter 3 Investigation of Surface Loss Probability of H Radicals in SiH₄/H₂ Plasma

3.1 Introduction	79
3.2 Experimental details	81
3.3 Results	83
3.3.1 Surface loss kinetics of H radicals in the afterglow of SiH ₄ /H ₂ plasma	83
3.3.2 H radical densities in SiH ₄ /H ₂ plasmas	88
3.3.3 Surface loss probability of H radicals in SiH ₄ /H ₂ plasma	89
3.3.4 Surface analysis of thin films deposited on chamber wall	92
3.3.5 Measurement of VUV radiation from SiH ₄ /H ₂ plasma	94
3.3.6 Dependence of the absolute density and surface loss probability of H radicals on the temperature of the chamber wall	96

Contents

3.4 Discussion	98
3.5 Conclusion	100
3.6 References	101
Chapter 4	Investigation of H and SiH₃ Radicals in Microcrystalline Silicon Deposition
4.1 Introduction	104
4.2 Experimental details	106
4.3 Results and discussion	109
4.3.1 Measurement of H radicals	109
4.3.2 Investigation of the behavior of the H radical density on the basis of the calculation	113
4.3.3 Measurement of SiH ₃ radicals	117
4.3.4 Film deposition characteristic	121
4.3.5 Relation between flux of radicals and film deposited property	124
4.4 Conclusion	128
4.5 References	129
Chapter 5	Fabrication of Microcrystalline Silicon Thin Film by H Radical-Injection Plasma
5.1 Introduction	131
5.2 Experimental details	134
5.3 Results and discussion	138
5.3.1 Plasma diagnostics	139
5.3.2 Film deposition characteristics	142

Contents

5.4 Conclusion	153
5.5 References	155

Chapter 6 Conclusions and Future Works

6.1 Conclusion of present research	157
6.2 Scopes for future works	160

Acknowledgements	162
-------------------------------	-----

List of Papers	165
-----------------------------	-----

Chapter 1 Introduction

1.1 Trend in Solar Cells

1.1.1 Background of photovoltaic generation

The global warming by emission CO₂ is one of critical environmental issues. Kyoto Protocol to the United Nations Framework Convention on Climate Change was adopted in 1997 and it entered into force in 2005. The major feature of the Kyoto Protocol is that it sets binding targets for 37 industrialized countries and the European community for reducing greenhouse gas emissions. These reductions amount to an average of five percent against 1990 levels over the five-year period 2008-2012.¹ Post-Kyoto Protocol which is about the period after the end of 2012 has been discussed at Ad Hoc Working Group on Long-term Cooperative Action under the Convention (AWG-LCA), the Ad Hoc Working Group on Further Commitments for Annex I Parties under the Kyoto Protocol (AWG-KP), and United Nations Climate Change Conference. In order to realize the reduction of greenhouse gas emissions, renewable energy is absolutely imperative.

In this context, photovoltaic powers have attracted much attention as a one of the renewable energy. Photovoltaic power generation, which employs solar cells as energy conversion devices, is a promising form of clean energy that does not emit greenhouse gases. However, the actual CO₂ emission per kilowatt hour is nonzero because energy is consumed in the manufacture of solar cells and the installation of photovoltaic systems. Moreover, the reduction of CO₂ emissions per kilowatt hour resulting from the use of photovoltaic systems depends on the power source structure used in their manufacture and installation. CO₂ emission due to nuclear power generation is very small, and therefore, the reduction of CO₂ emissions per kilowatt hour due to the use of photovoltaic

systems depends on the proportions of thermal and nuclear power generation. In the case of Japan, assuming the basic unit of lifecycle CO₂ emission due to photovoltaic power generation to be 0.05 kg-CO₂/kWh, the reduction of CO₂ emission per kilowatt hour achieved by installing photovoltaic systems is calculated to be approximately 0.3 kg-CO₂/kWh [= 0.35 (the average of lifecycle CO₂ emission due to other power generations) – 0.05].² In 2010, cumulative installed photovoltaic power generation capacity and the amount of CO₂ emission of Japan were 3.6×10^9 kWh and 1.26×10^{12} kg, respectively, therefore the reduction of CO₂ is still only 0.086% of CO₂ emission. To reduce CO₂ more than 1%, a cumulative installed capacity of 50 GW is necessary. The research and development are indispensable to install such large-scale photovoltaic power generations, especially the immediate challenge in the technological development of photovoltaic power generation is to lower the cost of electricity generation.³

1.1.2 Brief history of solar cells

The photovoltaic effect was first experimentally demonstrated by Alexandre-Edmond Becquerel in 1839.⁴ In this experiment, silver-chloride was placed in an acidic solution and illuminated while connected to platinum electrodes, thus generating photovoltage and photocurrent. In 1883, the first solid state solar cell was built by Charles Fritts, who coated the semiconductor selenium with an extremely thin layer of gold to form the junctions.⁵ The device was only around 1% efficient.

The first practical solar cell was developed in 1954 at Bell Laboratories by Dary Chapin, Calvin Souther Fuller, and Gerald Petarson.⁶ They used a silicon p-n junction in which a thin layer of p-layer was formed over an n-type base. The device realized 6% efficient.

Chapter 1

In the 1970s, thin films of Si and a whole range of new semiconductor materials (CIS, CdTe, InP, Zn₃P₂, Cu₂Se, WSe₂, GaAs, ZnSiAs) were developed. They are almost all the alternative materials used by today's new PV industry, including polycrystalline and amorphous silicon, and organic semiconductors.

In the early 1980s, Allen M. Barnett developed the polycrystalline Si thin film cell;⁷ while Martin Green replaced the silicon serigraphy with a silicon solar cell with greater surface area to catch the sun's rays with tiny, laser-etched grooves in which the wires (contacts) that carry the electric current are buried, leading to 20% efficient cells.⁸

In 1994, microcrystalline silicon cell was reported⁹. In 2007, Sanyo corp. achieved an efficiency of 22% at the research level with its HIT solar cells.¹⁰ The HIT (heterojunction with intrinsic thin layer) solar cell is composed of a single thin crystalline silicon wafer surrounded by ultra-thin amorphous silicon layers.

Table 1.1 shows various solar cells with different features, including their type, conversion efficiency, and future prospects of their application.³

Chapter 1

Table 1.1 Conversion efficiency, annual production volume, and future prospects for application to power generation of various solar cells.

Solar cell material	Product-level module conversion efficiency (%)	R&D-level module conversion efficiency (%)	R&D-level small-area cell conversion efficiency (%)	Total world production in 2007 (MW)	Future prospects for application to power generation
Bulk solar cell					
1. Single crystal Si	13-18	22.9 (778 cm ²)	25.0 (4 cm ²)	1,355	25 GW manufacturing capacity in 2010
2. Polycrystalline Si	13-15	15.5 (1017 cm ²)	20.4 (1 cm ²)	1,837	
3. GaInP/GaAs/Ge Triple junction	—	—	41.1 (0.05 cm ²) 454 suns	—	
Thin-film solar cell					
4. a-Si	6-7	6-8	9.5 (1 cm ²)	168	4.8 GW manufacturing capacity in 2010
5. a-Si/ μ c Si double junction	9-10	12-13	15.0 (1 cm ²)	Sum of 4. and 5.	
6. Cu(InGa)Se ₂	10-11	13-15 (900 cm ²)	19.4 (1 cm ²)	40	1.3 GW manufacturing capacity in 2010
7. CdTe	10-11	11-12 (40 \times 120 cm ²)	16.7 (1 cm ²)	219	The production of CdTe solar cells by First Solar was 504 MW in 2008 and will reach 1 GW in 2010
8. Dye-sensitized	—	8.4 (17 cm ²)	10.4 (1 cm ²)	—	Immediate goal of consumer use
9. Organic semiconductor	—	2.05 (223 cm ²)	5.15 (1 cm ²)	—	Immediate goals of improving conversion efficiency and reliability

1.2 Thin-film silicon solar cells

1.2.1 Introduction of thin-film silicon solar cells

Thin-film silicon solar cells are fabricated by the deposition of thin silicon films (1–3 μm) at low temperatures (around 200°C) on various substrate materials. Such thin-film silicon solar cells require a far lower amount of silicon material than the wafer-based crystalline silicon solar cells; this means that they have, on a medium-term time scale, a more pronounced cost reduction potential than the latter. Furthermore, As shown in Fig. 1.1, the complete traditional process of wafer-based crystalline silicon solar cells involves more than two dozen separate steps to prepare and process silicon ingots, wafers, cells, and circuit assemblies before a module is complete.¹¹ Thin-film module production, on the other hand, requires only half as many process steps as crystalline silicon with simplified materials handling. Therefore, ‘energy payback time’, i.e., the time required for the photovoltaic solar module to ‘pay back’, to the user, the quantity of energy invested during its fabrication, are lower in the case of thin-film silicon solar cells than for wafer-based crystalline silicon solar cells.¹² Compared with other thin-film solar cell technologies, thin-film silicon has the advantage of constituting an industrially mature technology and of being based on raw materials which are present in abundance in the earth’s crust. Their stabilized efficiency is, however, at this moment still rather limited. Improving the conversion efficiency is necessary for more widespread use of thin-film silicon solar cells.

There are two forms of thin-film silicon material that can be used for constituting such a solar cell: hydrogenated amorphous silicon (a-Si:H) and hydrogenated microcrystalline silicon ($\mu\text{c-Si:H}$).

Chapter 1

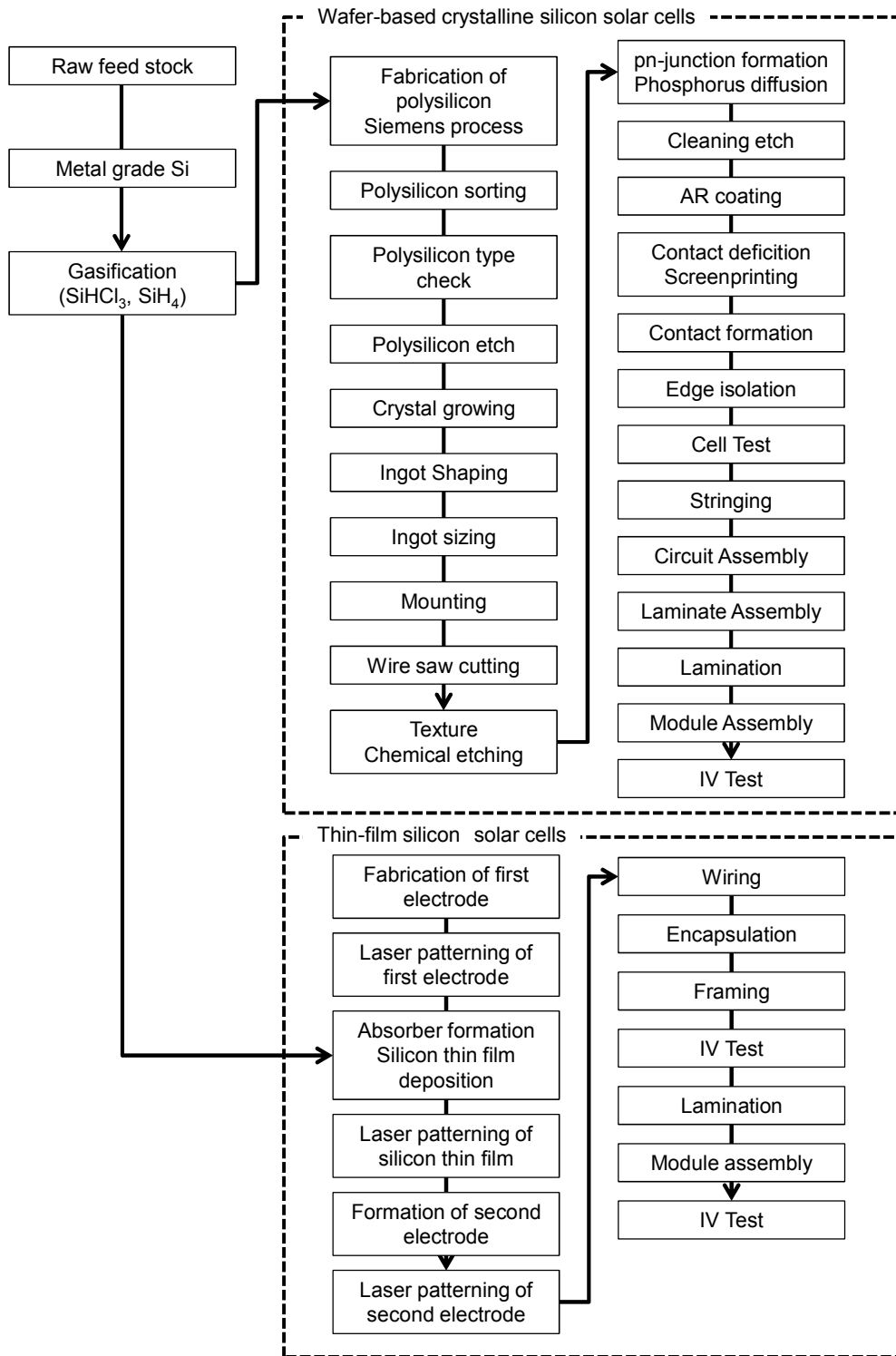


Fig. 1.1 Process sequence for manufacturing wafer-based crystalline silicon modules and process sequence for manufacturing thin-film silicon modules.^{11,13,14}

1.2.2 Amorphous silicon¹⁵

a-Si:H layers were first deposited by R. Chittick. He was experimenting with silane (SiH_4) plasmas and accidentally obtained a-Si:H layers in a remote part of his plasma reactor. Chittick's results were taken up by W. E. Spear and co-workers at Dundee University, who published¹⁶ the first systematic study on plasma-enhanced chemical vapour deposition (PECVD) with silane plus (optional) doping gases. Glow discharge decomposition of SiH_4 enables one to build actual semiconductor devices with a-Si:H layers. It is, however, not advisable to use p-n type diodes as solar cell structure, in the case of amorphous silicon, and this for three reasons:

- (1) The doping capability of a-Si:H is rather poor, the Fermi-level can be pushed only half way towards the conduction and valence band edges, even with heavy doping.
- (2) Doping has a detrimental effect on a-Si:H layer quality, because it leads to the creation of many additional silicon dangling-bonds, which are the main recombination centers in this material.
- (3) In a classical p-n type solar cell, carrier collection is obtained by minority carrier diffusion within the p- and n-layers. Fortunately, diffusion lengths in crystalline silicon wafers are sufficiently high (over 200 μm), to ensure a near-perfect carrier collection over the whole useful range of the solar cell thickness where significant optical absorption takes place. In a-Si:H layers, on the other hand, minority carrier diffusion lengths are extremely small (around 0.1 μm), and it becomes impossible to base the collection of photogenerated carriers on diffusion alone.

Because of these three reasons p-i-n diodes are always used for a-Si:H solar cells. The corresponding structure is shown schematically in Fig 1.2. In such a p-i-n cell the main part of light absorption and photogeneration of carriers will take place in the intrinsic part of the solar cell. The p-i-n-type a-Si:H solar cell was introduced in 1977 by

D. Carlson et al. at RCA Laboratories, Princeton, New Jersey, USA.¹⁷

In the first years after their introduction, p-i-n-type amorphous silicon solar cells made rapid progress in reaching higher efficiencies. By 1982, a-Si:H solar cells with (initial) efficiencies over 10% had been obtained.¹⁸ However, a-Si:H solar cells suffer from a light-induced degradation effect (the so-called Staebler-Wronski effect) and stabilize only at lower efficiency values.

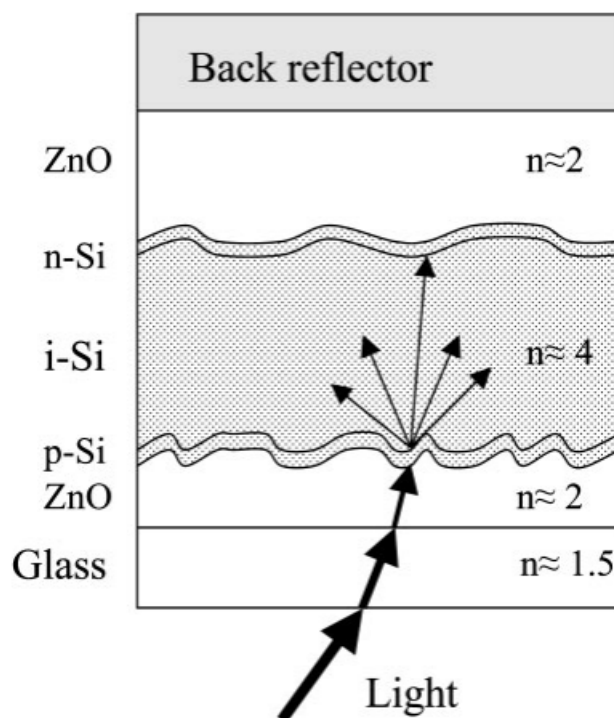


Fig. 1.2 Schematic sketch of a typical p-i-n thin-film silicon solar cell, as used both for a-Si:H and for μ c-Si:H. The values for n indicated here give approximate values of the optical index of refraction, an important parameter for light trapping considerations.¹⁵

1.2.3 Microcrystalline silicon¹⁵

$\mu\text{c-Si:H}$ layers were first produced by Veprek and Marecek in 1968 in Prague¹⁹ by a low-temperature plasma-assisted deposition process. Usui and Kikuchi showed in 1979 that doping of $\mu\text{c-Si:H}$ layers is possible;²⁰ it is indeed more easily achieved than that of a-Si:H layers.

Because of the poor quality of the first $\mu\text{c-Si:H}$ layers^{20,21} (i.e., because of their relatively high defect density) and because of the n-type character of most layers produced, even without addition of doping gases, it was originally believed that it would not be possible to make reasonable solar cells with an $\mu\text{c-Si:H}$ intrinsic layer acting as the main photoconversion layer. However, in 1996, J. Meier et al.²² at Neuchâtel University reported p-i-n-type fully microcrystalline thin-film silicon solar cells with an efficiency value of 7.7%. This was achieved by using a gas purifier to deposit an intrinsic layer with low oxygen content, as previously shown by U. Kroll et al.,^{23,24} and used for $\mu\text{c-Si:H}$ solar cells by P. Torres et al.²⁵ These $\mu\text{c-Si:H}$ solar cells generally do not suffer from a pronounced Staebler-Wronski effect. However, even though doping is far easier in $\mu\text{c-Si:H}$ than in a-Si:H, and even though doped $\mu\text{c-Si:H}$ layers do not have additional defects introduced by the doping process (as far as one can judge today), one still always uses the p-i-n-type configuration for fabricating $\mu\text{c-Si:H}$ cells, because the diffusion lengths in $\mu\text{c-Si:H}$ material are, just as in a-Si:H, far too low, and therefore drift-assisted collection is necessary.

Following the introduction of $\mu\text{c-Si:H}$ as novel solar cell material, microcrystalline/amorphous or 'micromorph' tandem solar cell was demonstrated to be a high efficiency thin-film silicon solar cell.²² As shown in Fig. 1.3, the spectral sensitivity of the micromorph tandem is larger than that of single junction because of two distinctly different gap energies (1.75 (a-Si:H) and 1.1 eV ($\mu\text{c-Si:H}$)). The a-Si:H (top cell) absorbs

visible light and $\mu\text{c-Si:H}$ (bottom cell) absorbs red and infrared light of the solar spectrum. Since the $\mu\text{c-Si:H}$ has an indirect band gap, the same as single-crystalline Si, thicker intrinsic $\mu\text{c-Si:H}$ films (1–3 μm) are required, compared to a-Si:H typically (200–400 nm). Therefore, the high-deposition technique of $\mu\text{c-Si:H}$ is critical issue for the cost reduction of the micromorph tandem solar cell.

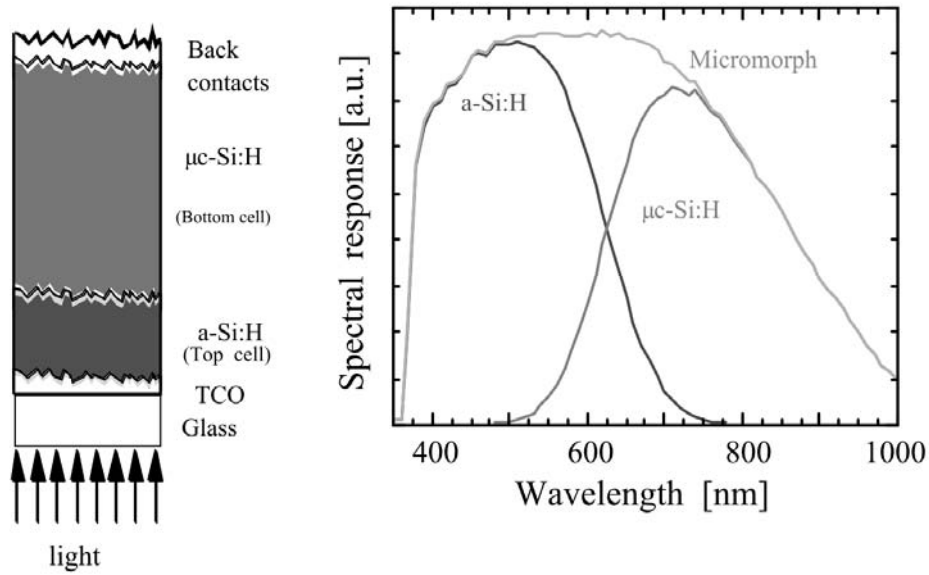


Fig.1.3 Schematic structure and corresponding typical spectral response of a micromorph tandem silicon solar cell.²⁶

1.3 Plasma process of thin-film silicon solar cells²⁷

Several methods have been proposed to fabricate device-grade a-Si:H or $\mu\text{c-Si:H}$ thin films. Reactive sputtering of crystalline-silicon targets with Ar+H₂ plasma,²⁸ mercury sensitized photo chemical vapor deposition (CVD) utilizing decomposition reaction of SiH₄ molecules with photo-excited Hg (Hg*),^{29,30} direct photo CVD method where high energy photons from Xe-resonance lamp or low pressure Hg lamp are used for direct excitation of SiH₄ molecules to their electronic excited states;³¹ hot-wire CVD method to decompose SiH₄ and H₂ by means of catalytic reactions on heated metal surface,³² and PECVD are also discussed. As compared to other methods, PECVD is widely used due to its high potential to fabricate high quality materials uniformly on a large area substrate.

The initial event for the growth of $\mu\text{c-Si:H}$ and a-Si:H is the decomposition process of source gases in SiH₄ and SiH₄/H₂-glow-discharge plasmas. Figure 1.4 shows a schematic illustration of the dissociation pathway of SiH₄ and H₂ through electronic excited states of those molecules by inelastic collisions with high energy electrons in the plasma. As the energy of electrons in the plasma varies from zero to several ten electron volts (eV), the ground-state electrons of the source gas molecules are excited into their electronic excited states almost simultaneously by inelastic collisions with energetic electrons. Electronic excited states of complicated molecules like SiH₄ are usually dissociating states, from which dissociation occurs spontaneously to SiH₃, SiH₂, SiH, Si, H₂ and H as shown in Fig. 1.4 depending on the stereochemical structure of excited states without emitting photons to return back to their ground state.³³

Dissociation of SiH₄ is caused by the impact of the electron with the energy of 8.75 eV or higher and H₂ molecule is also decomposed to atomic H (H radical) by the electron with the energy of 8.8 eV or higher. Therefore, the high-energy electrons in the

tail region of the electron-energy-distribution function contribute to the dissociation of these molecules. When the partial pressure of SiH_4 is low and an electron density is high, SiH_4 is highly dissociated, followed by depletion, which is so-called high SiH_4 -depletion condition. As a matter of course, excitation of groundstate electron to vacuum state gives rise to ionization event, generating new electron and ions to maintain the plasma.

Table 1.2 shows part of reaction-rate constants which were reported in literatures.³⁴⁻³⁶ Reactive species produced in the plasma experiences secondary reactions mostly with parent SiH_4 and H_2 molecules, forming a steady state. Steady-state densities of reactive species are basically determined by the balance between their generation rate and their annihilation rate. Therefore, highly reactive (short lifetime) species such as SiH_2 , SiH , and Si with SiH_4 and H_2 take much smaller value than SiH_3 (long lifetime species) that shows low reactivity with SiH_4 and H_2 in the steady-state plasma, although the generation rates of those species are not so different.

Among these species, the SiH_3 radical is recognized as the dominant film precursor for a-Si:H and $\mu\text{c-Si:H}$.^{37,38} The H radical is considered to play important roles in the case of $\mu\text{c-Si:H}$ growth.³⁹ The contribution of short lifetime species to film growth leads to enhance the creation of dangling-bond defects in the film. In addition, the nano-particles generation is started by an insertion reaction of the short lifetime species such as SiH_2 into SiH_4 forming Si_2H_6 . The nano-particle generation can affect the electrode and chamber wall conditions and can induce unwelcome long-term changes in the plasma parameters through electron attachment. Furthermore, the formed nano-particles increase the maintenance frequency of the deposition systems.

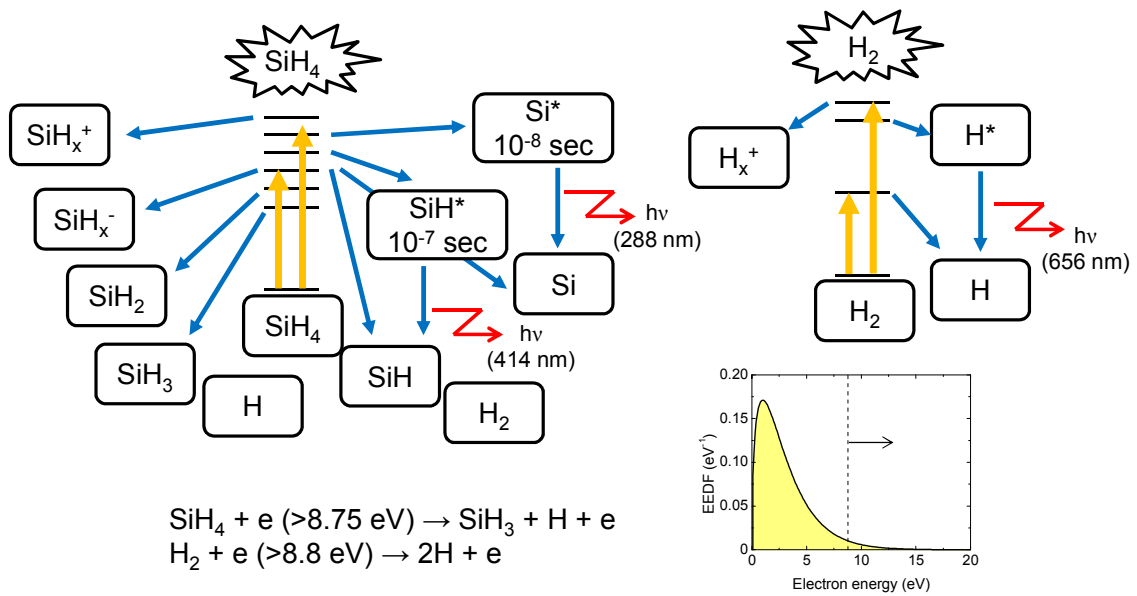


Fig. 1.4 Schematic illustration of the dissociation processes of SiH_4 and H_2 molecules to a variety of chemical species in the plasma through their electronic-excited states. Typical electron-energy-distribution function (EEDF) in the plasma with assuming electron temperature (T_e) as 2 eV is also shown.

Chapter 1

Table 1.2 Selected reaction rate constants for SiH₄ plasma

	Reaction	Rate Constant	Reference
Electron impact	$e + \text{SiH}_4 \rightarrow \text{SiH}_3 + \text{H} + e$	$7.7\text{E-}7 T_e^{-1} \exp(-10.6/T_e)$	35
	$e + \text{SiH}_4 \rightarrow \text{SiH}_2 + 2\text{H} + e$	$1.6\text{E-}7 T_e^{-1} \exp(-10.6/T_e)$	35
	$e + \text{SiH}_4 \rightarrow \text{SiH}_3^- + \text{H}$	$1.5\text{E-}11 \exp(-9/T_e)$	36
	$e + \text{SiH}_4 \rightarrow \text{SiH}_2^- + \text{H}_2 + e$	$9\text{E-}12 \exp(-9/T_e)$	36
	$e + \text{SiH}_4 \rightarrow \text{SiH}_3^+ + \text{H} + 2e$	$3.3\text{E-}9 \exp(-12/T_e)$	36
	$e + \text{SiH}_4 \rightarrow \text{SiH}_2^+ + \text{H}_2 + 2e$	$4.7\text{E-}9 \exp(-12/T_e)$	36
Neutral-neutral reactions	$\text{SiH}_4 + \text{H} \rightarrow \text{SiH}_3 + \text{H}_2$	$2.8\text{E-}11 \exp(-1250/T)$	34
	$\text{SiH}_4 + \text{SiH}_2 \rightarrow \text{Si}_2\text{H}_6^*$	1E-11	36
	$\text{Si}_2\text{H}_6^* \rightarrow \text{Si}_2\text{H}_4 + \text{H}_2$	5E6/s	36
	$\text{Si}_2\text{H}_6^* + \text{SiH}_4 \rightarrow \text{Si}_2\text{H}_6 + \text{SiH}_4$	1E-10	36
	$\text{SiH}_4 + \text{SiH}_3 \rightarrow \text{Si}_2\text{H}_5 + \text{H}_2$	$2.94\text{E-}12 \exp(-1006/T)$	35
	$\text{SiH}_4 + \text{SiH} \rightarrow \text{Si}_2\text{H}_5^*$	$6.9\text{E-}10 [1-1/(1+0.33P)]$	34
	$\text{SiH}_3 + \text{SiH}_3 \rightarrow \text{SiH}_2 + \text{SiH}_4$	2.99E-11	35
	$\text{SiH}_2 + \text{H}_2 \rightarrow \text{SiH}_4^*$	$3.0\text{E-}12 [1+1/(1+0.03P)]$	34
Ion-neutral reactions	$\text{SiH}_3^+ + \text{SiH}_4 \rightarrow \text{Si}_2\text{H}_5^+ + \text{H}_2$	0.6E-10	34
	$\text{SiH}_2^+ + \text{SiH}_4 \rightarrow \text{SiH}_3^+ + \text{SiH}_3$	11.3E-10	34

Note: T_e in eV and T in K. The notation E-x means 10^{-x} .

1.3.1 Growth of a-Si:H

SiH₃ radicals reaching the film-growing surface start to diffuse on the surface. During surface diffusion, SiH₃ abstracts surface-covering bonded hydrogen, forming SiH₄ and leaving dangling-bond on the surface (growth-site formation). Toward the dangling-bond site on the surface, another SiH₃ diffuses to find the site and to make Si–Si bond (film growth) as schematically shown in Fig. 1.5. This surface-reaction scheme for the film growth has been proposed on the basis of two experimental results.⁴⁰ Fig. 1.6 shows a general concept of surface-reaction process. A part of unity-flux density of SiH₃ is reflected as it is (reflection probability). Remaining part of SiH₃ is adsorbed on the surface and it changes its form as follows; (1) SiH₃ abstracts surface-covering bonded H forming SiH₄ or two SiH₃ radicals are encountered on the surface forming Si₂H₆ (recombination probability β), and (2) surface-diffusing SiH₃ sticks to the dangling-bond site forming Si–Si bond (sticking probability s). Total loss probability (α) is given by the sum of recombination probability and sticking probability ($\beta + s$), and reflection probability is expressed as $(1 - \alpha)$.

The density of dangling bond defect is one of important parameters in silicon thin films for device applications. Structural properties in the resulting film is basically determined by the steady-state growing-surface properties, in general, for the thin film growth process, because the surface at an instant is involved into the bulk at the next instant by the successive film growth. Steady-state-number density of surface dangling-bond is determined by the balance between the generation rate of dangling bonds and annihilation rate of them. SiH₃ radicals can find stable low potential sites on the surface through diffusion followed by sticking to the dangling-bond site. The sticking of SiH₃ radicals contributes to both reducing and creating the dangling-bond defect on the surface, as shown in Fig.1.5. On the other hand, the sticking SiH _{\leq 1} species to the

surface creates dangling-bond defects.

Since the insertion reactions of short lifetime species $\text{SiH}_{x \leq 2}$ into Si-H bonds have high reactivity, they are unable to diffuse on the surface. The sticking reactions of SiH_2 arriving on the film surface are also shown in Fig. 1.5. The contribution of the $\text{SiH}_{x \leq 2}$ to film growth, therefore, leads to enhanced creation of the dangling-bond defects on the film-growing surface, and hence, results in a high dangling-bond-defect density of the resulting film, on the assumption that the surface dangling-bond defects become statistically incorporated in the film.⁴¹

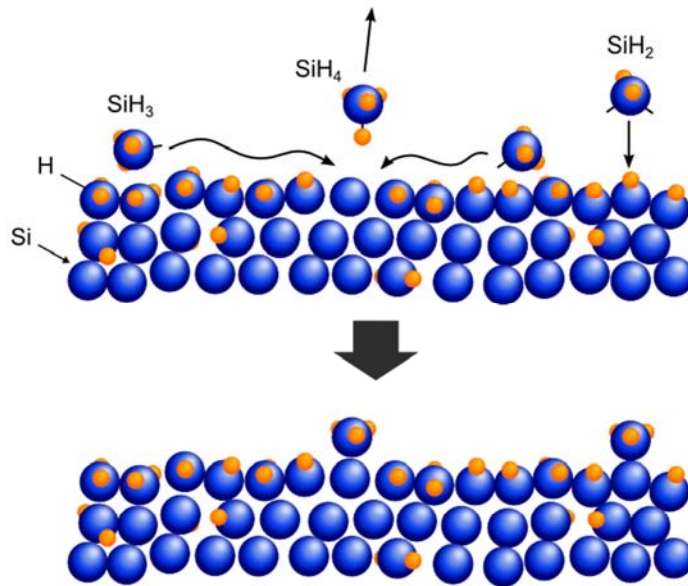


Fig. 1.5 Schematic illustration for the surface-growth process of a-Si:H in the case that dominant film precursor is SiH₃. Large sphere and small sphere represent Si and H, respectively.

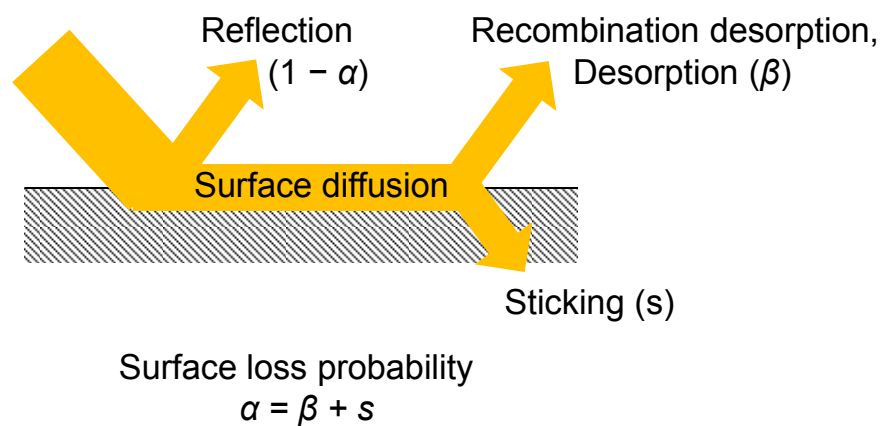


Fig. 1.6 General concept of surface-reaction process

1.3.2 Growth of $\mu\text{c-Si:H}$

H radicals reaching the film-growing surface play an important role for the growth of $\mu\text{c-Si:H}$. This has also been indicated in the $\mu\text{c-Si:H}$ -formation map drawing on the space between electric power density (radio frequency RF of 13.56 MHz in this case) applied to the plasma and H_2 -dilution ratio R in the source gas materials at constant substrate temperature during film growth as shown in Fig. 1.7.³⁹

In order to explain specific phenomena in the formation process of $\mu\text{c-Si:H}$, three models have been proposed; (1) surface-diffusion model,³⁹ (2) etching model,⁴² and (3) chemical-annealing model.⁴³

Surface-diffusion model is schematically illustrated in Fig. 1.8. Sufficient amount of H radical flux from the plasma realizes a full surface coverage by bonded H and also produces local heating through hydrogen-exchanging reactions on the film-growing surface. These two actions enhance the surface diffusion of film precursors (SiH_3). As a consequence, SiH_3 adsorbed on the surface can find energetically favorable sites, leading to a formation of atomically ordered structure (nucleus formation). After the formation of nucleus, epitaxial-like crystal growth takes place with an enhanced surface diffusion of SiH_3 .^{39,44}

Etching model has been proposed based on the experimental fact that film-growth rate is reduced with an increase of H_2 -dilution ratio R. A concept of the etching model is schematically shown in Fig. 1.9. H radicals reaching the film-growing surface break Si-Si bonds, preferentially weak bonds involved in the amorphous network structure, leading to a removal of Si atoms weakly bonded to another Si. This site is replaced with a new film precursor SiH_3 , creating rigid and strong Si-Si bond, giving rise to an ordered structure.^{42,44}

Chemical-annealing model has been proposed to explain the experimental fact that crystal formation is observed during hydrogen-plasma treatment in a layer-by-layer growth by an alternating sequence of thin amorphous film growth and H₂-plasma treatment. Several monolayers of amorphous silicon are deposited and these layers are exposed to H radicals produced in the H₂ plasma. These procedures are repeated alternately for several ten times to fabricate the proper thickness for evaluation of film structure. The absence of remarkable reduction of film thickness during the H₂-plasma treatment is hard to be explained by the etching model and the chemical-annealing model has been proposed as schematically shown in Fig. 1.10. During the H₂-plasma treatment, many H radicals are permeating in the subsurface (growth zone), giving rise to a crystallization of amorphous network through the formation of a flexible network with a sufficient amount of H radicals in the sub-surface region without remarkable removal process of Si atoms.^{43,44} These three models have been carefully examined, and validity for each model has been discussed.^{44,45}

Ionic species impinging to the film-growing surface of $\mu\text{c-Si:H}$ have the negative effect. It has been reported that the crystallinity of Si thin films decreased with increasing energy of ionic species impinging to the film-growing surface.⁴⁶

In the case of $\mu\text{c-Si:H}$, short lifetime species are recognized as the cause of dangling-bond defect as same as a-Si:H. Moreover, a collision of crystals growing from different nuclei influences the dangling-bond-defect density in $\mu\text{c-Si:H}$, which is different from the case of a-Si:H.⁴⁷

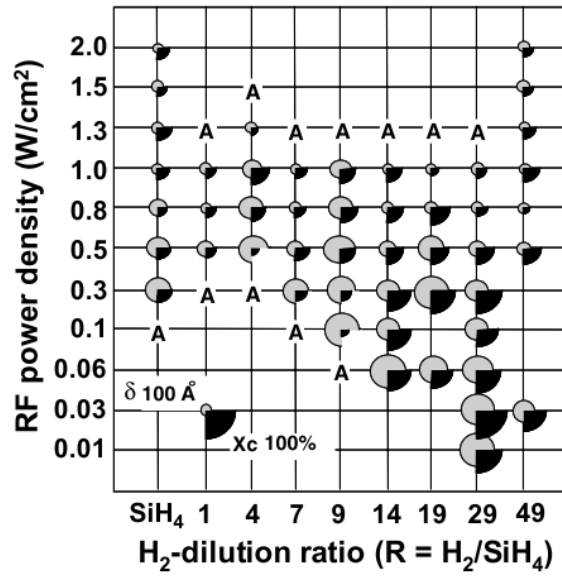


Fig. 1.7 Crystal size (three-quarter gray circles: δ) and volume % (quarter solid circles: X_c) of microcrystallites in the resulting films mapped out on the RF power density/hydrogen-dilution ratio plane.³⁹

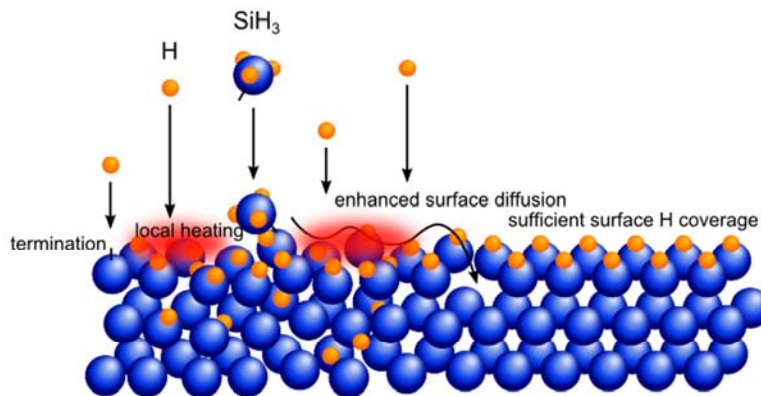


Fig. 1.8 Surface-diffusion model for $\mu\text{c-Si:H}$ formation.

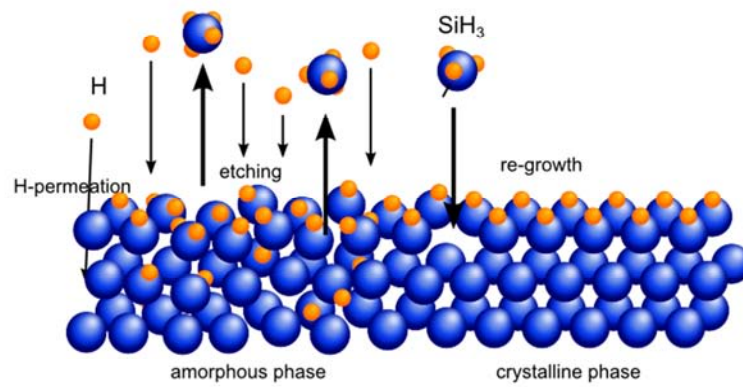


Fig. 1.9 Etching model for $\mu\text{c-Si:H}$ formation.

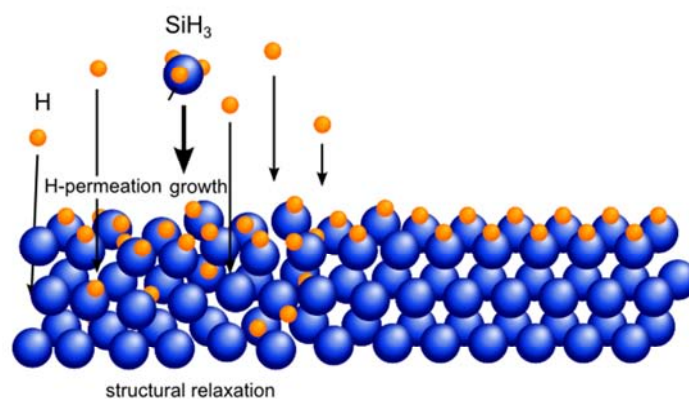


Fig. 1.10 Chemical-annealing model for $\mu\text{c-Si:H}$ formation.

1.3.3 High-rate deposition of $\mu\text{c-Si:H}$

In order to apply $\mu\text{c-Si:H}$ to solar cells, intrinsic $\mu\text{c-Si:H}$ active layer needs thickness more than $2\ \mu\text{m}$ to absorb sufficient sunlight. Therefore, high-rate deposition technique of high quality $\mu\text{c-Si:H}$ is strongly required for the cost reduction of solar cells.

In previous studies, a growth rate of ca. $2\ \text{nm/s}$ has been achieved using capacitively coupled plasma (CCP) with with a high input power of very-high-frequency (VHF as power-source frequency), a high working pressure (ca. $1000\ \text{Pa}$), and a narrow electrode gap. The high pressure and the high input power of VHF-power source provide a high-electron density, which leads to the efficient generation of a film precursor. The high pressure also suppresses high ion energy which causes the formation of defect in films. In addition, the high electron density is effective to achieve SiH_4 depletion, even at a relatively high working pressure. SiH_4 depletion is useful for the survival of H radicals, because SiH_4 is a H radical scavenger.

When increasing the film-growth rate ($>2\ \text{nm/s}$), optoelectronic properties in the resulting $\mu\text{c-Si:H}$ are severely deteriorated through an increase of defect density.^{48,49} It is considered that the defect density in the resulting $\mu\text{c-Si:H}$ is strongly dependent on the contribution ratio of short lifetime species such as $\text{SiH}_{x\leq 2}$ to film growth. A high depletion of SiH_4 causes an increase in the contribution of short-lifetime species. Moreover, increasing pressure reduces electrode spacing between cathode and anode to produce stable plasma in the CCP reactor, causing non-uniform plasma production and non-uniform film growth. Therefore, the high-rate deposition technique which does not deteriorate the film quality of $\mu\text{c-Si:H}$ is strongly required.

1.4 Diagnostics for activated species in the plasma

Activated species was very important in determining the performances of the plasma process. Therefore, the information on behaviors of these species in the gas phase is essential to understanding the plasma chemistries and hereby controlling the plasma processing. In reactive plasmas, many species have been investigated so far by using various diagnostics techniques.

1.4.1 Measurement for atomic radicals

Table 1.3 shows measurement techniques for atomic radicals.

Optical emission spectroscopy (OES) is one of the most popular techniques to measure the activated species in plasmas, since OES does not require the special laser equipment which is expensive.

Relative densities of species can be measured by using the actinometric OES (AOES) method in reactive plasmas.⁵⁰ The detail procedure is described in Chapter 2. Using the AOES, the detection of fluorine (F) atoms has been made with reliability in the etching plasma processing. The validity of AOES has been investigated extensively by using the established measurement method for F atom density.⁵¹⁻⁵⁶

The hydrogen (H) atom densities have been derived from OES using two line Balmer lines (BOES) where the emission intensities of Balmer α (H_α 656.3 nm) and Balmer β (H_β 486.1 nm) are compared.⁵⁷ This method is based on the fact that the upper level of Balmer lines is populated both by electron impact with ground state atoms and ground state molecules. For this method, the availability of reliable cross-sections of direct excitation and dissociative excitation of two lines are very important. In general, however, the knowledge of the cross-sections is insufficient and so it is necessary to

estimate the electron energy distribution function (EEDF) close to threshold accurately.

Optical absorption spectroscopy is a powerful tool to obtain the information about the absolute density of radicals directly in the plasmas. This technique does not disturb the plasma and does not need the procedure of calibration for estimating the absolute density. The Si atom densities in the parallel-plate RF and ECR SiH₄ plasmas were measured by ultraviolet absorption spectroscopy (UVAS) using the incoherent hollow cathode lamp, which is a very compact light source.^{58,59} Hiramatsu et al. have measured Si atom densities in the parallel-plate SiH₄ plasma employing UVAS with a ring dye laser which has the narrow linewidth.⁶⁰

Tachibana and Kamisugi have developed the vacuum ultraviolet laser absorption spectroscopy (VUVLAS) for the measuring the F atoms in the plasma,⁶¹ in which coherent VUV emissions at 95–96 nm have been obtained by two-photon resonance four wave frequency mixing technique using Xe gas. This method is very reliable and extended to the measurement of the densities of C atoms,⁶² H atoms, nitrogen (N) atoms, and oxygen (O) atoms⁶³ in the ground state. Umemoto et al. have measured H atoms in Cat-CVD with SiH₄/H₂ by VUVLAS with the phase-match third harmonic generation technique.⁶⁴ Takeda et al. determined the flux of exited O atom [O(¹D₂)] using phase-matched frequency tripling.⁶⁵ These methods basically need the specialized skill to operate the dye laser system and the sophisticated techniques such as frequency mixing and phase-matching, and so on.

The VUV absorption spectroscopy (VUVAS) using resonance fluorescence emission in the VUV region has been proposed to measure F atom densities in the etching plasmas.⁵¹ However, the self-absorption exists generally in the light source and it causes the distortion of line shape of the probe emission considerably from Gaussian profile. Therefore, this technique has some issues to be solved in measuring the absolute densities of F atoms in the plasma.

Takashima et al. have developed a reliable measurement technique for atomic radicals in the reactive plasmas employing the VUVAS with a high pressure microdischarge hollow cathode lamp (MHCL). This emission line profile does not involve a large Doppler broadening due to excited atomic radicals and the distortion of the line shape does not occur. Moreover, this measurement system is very compact. This technique is successfully applied to the measurement of the absolute density of H atoms in reactive plasmas employing SiH₄ and CH₄, and extended to the measurements of the absolute densities of O, C, and N atoms with various kind of plasma processing.⁶⁶⁻⁷³

Two-photon absorption laser induced fluorescence (TALIF) technique has been applied to the measurement of H atoms in H₂ plasmas,⁷⁴⁻⁷⁷ N atom in N₂ plasma,⁷⁸ and O atom in O₂ plasmas⁷⁹⁻⁸¹ and O₂/CF₄ plasmas.⁸² This technique has potentially a high temporal, spatial resolution and a wide dynamic range, but the calibration procedure for obtaining the absolute scale requires many assumptions. Moreover, the laser used in TALIF sometimes causes the dissociation of feed gases and other species in the plasma.

1.4.2 Measurement for molecular radicals

Table 1.4 shows the measurement techniques of molecular radicals. Molecular radicals such as CF_x (x = 1-3), SiH_x (x = 1-3), and CH_x (x = 1-3) are so important that their behaviors and their gas phase kinetics should be measured and clarified for controlling the plasma processing. Infrared diode laser absorption spectroscopy (IRLAS) has been applied to the measurement of the absolute density of radicals in reactive plasmas. CH₃, CF, and CF₂ radicals were measured by UVAS using a deuterium lamp or a Xe arc lamp.⁸³⁻⁸⁵ In the case of measurement of rotation-vibration transitions in the ground state with IRLAS, the sensitivity of the absorption is relative low compared with that of other methods detecting the electronic transitions. However, neutral non-emissive

radicals in the electronic ground state such as CF_3 , SiH_3 , and CH_3 , which had never been measured in the past by various optical measurement methods, were successfully measured by IRLAS. CF_x ($x = 1-3$) radical in C_2F_6 plasmas,⁸⁶ CHF_3 plasmas,^{87,88} and C_4F_8 plasmas,^{89,90} SiH and SiH_3 in SiH_4 plasmas,^{91,92} and CH_3 in CH_4 and CH_3OH plasmas^{93,94} have been reported previously. Intracavity laser absorption spectroscopy (ICLAS) was developed where the plasma was placed inside the laser resonator for getting a long absorption length and low-density SiH_2 radicals.⁹⁵

Recently, to improve the detection limit of radicals in the plasma, the cavity ring-down spectroscopy (CRDS) has been applied to the measurement of the molecular radical densities in reactive plasmas with high sensitivity.⁹⁶⁻¹⁰⁰ It realized the increase of the sensitivities of detection with pulse light sources. The sensitivity was significantly greater than those with the conventional absorption measurements employing the continuous light sources. This technique led to the development of the novel measurement systems such as phase-shift CRDS,¹⁰¹ Fourier transform CRDS,¹⁰² and cavity enhanced magnetic rotation spectroscopy¹⁰³ and extended to the detection of a lot of important radicals such as SiH , SiH_3 and CH radicals in reactive plasmas.

LIF has been frequently applied to the measurement of spatial distribution of radicals in reactive plasmas. Surface reaction rates and sticking probabilities have been also measured by using the LIF.¹⁰⁴ CF and CF_2 radicals in C_2F_6 , C_4F_8 , and CHF_3 plasmas,¹⁰⁵⁻¹⁰⁹ SiH and SiH_2 radicals in SiH_4 plasmas,^{110,111} SiF and SiF_2 radicals in SiF_4 plasmas,¹¹²⁻¹¹⁴ and CH radical in CH_4 plasmas¹¹⁵ have been reported previously.

Appearance mass spectroscopy (AMS) was developed for measuring the absolute density of several kinds of radicals such as CF_x ($x = 1-3$),¹¹⁶ and CH_x ($x = 1-3$)¹¹⁷ but had experimental difficulties in reliable measurement of radicals of relatively high sticking coefficient such as SiH_x ($x = 1-3$). Kuroda et al. proposed modified AMS to measure SiH_3 with a higher degree of accuracy.¹¹⁸

1.4.3 Measurement for polymeric radicals

The large neutral radicals have been attracted in the processes with fluorocarbon and silane gas based plasmas. Electron attachment mass spectroscopy (EAMS) has been applied to the investigation of the fluorocarbon plasmas.^{119,120} The large neutral molecules and radicals are transferred into negative ions by attachment of low-energy electrons and subsequently the negative ions are detected by the mass spectrometer. As the formation process of negative ions contains the dissociative attachment process, the direct measurement of large molecular radicals using EAMS is very difficult. However, it enables us to measure the behaviors of large molecular radicals in the plasma.

Nakamura et al. have developed the ion attachment mass spectroscopy (IAMS) for measuring the large neutral molecules and radicals. In this method, the neutral species are ionized by attachment of Li^+ ion. The ion attachment energy is so low that the target species seldom suffer the decomposition even if they are unstable dissociative radicals. Unstable polymeric species in C_4F_8 plasmas has been measured by this method.¹²¹

Table 1.3 Various techniques for measurement of atomic radicals.

Measurement methods	Measured Radicals	Gases	Reference
Optical emission spectroscopy (OES)			
Actinometric OES (AOES)	F	CF ₄	50
OES due to two Balmer lines (BOES)	H	H ₂	57
Optical absorption spectroscopy (OAS) with incoherent light sources			
Ultraviolet absorption spectroscopy (UVAS)	Si	SiH ₄	58–60
Vacuum ultraviolet absorption spectroscopy (VUVAS)	H	H ₂ , SiH ₄ , CH ₄	66–68
	O	O ₂	72,73
	N	N ₂	71
	F	C ₄ F ₈	51
OAS with coherent light sources			
Vacuum ultraviolet laser absorption spectroscopy (VUVLAS)	H	H ₂ , SiH ₄	64
	O	O ₂	63,65
	N	N ₂	63,70
	F	CHF ₃ , CF ₄ , C ₂ F ₆	61
	C	CHF ₃ , CF ₄ , C ₂ F ₆	62
Two-photon absorption laser induced fluorescence (TALIF)	H	H ₂	74–77
	N	N ₂	78
	O	O ₂ , CF ₄ /O ₂	79–82

Table 1.4 Various techniques for measurement of molecular radicals.

Measurement methods	Measured Radicals	Gases	Reference
Optical absorption spectroscopy			
(OAS) with incoherent light sources			
Ultraviolet absorption spectroscopy (UVAS)	CH ₃	CH ₄ /H ₂	83
	CF, CF ₂	C ₄ F ₈ /C ₂ H ₂ F ₂ /Ar	84,85
OAS with coherent light sources			
Infrared diode laser absorption spectroscopy (IRLAS)	CF, CF ₂ , CF ₃	C ₂ F ₆ , CHF ₃ , C ₄ F ₈	86–90
	SiH, SiH ₃	SiH ₄	91,92
	CH ₃	CH ₄ , CH ₃ OH	93,94
Intracavity laser absorption spectroscopy (ICLAS)	SiH ₂	SiH ₄	95
Cavity ring down spectroscopy (CRDS)	SiH ₃ , SiH, Si	SiH ₄	97,98,122
	CH ₃ , CH	CH ₄ , C ₂ H ₂	99,100
Laser-induced fluorescence spectroscopy (LIF)	CF, CF ₂	C ₂ F ₆ , C ₄ F ₈ , CHF ₃	105–109
	SiH, SiH ₂	SiH ₄	110,111
	SiF ₂	SiF ₄	112–114
	CH	CH ₄	115
Appearance mass spectroscopy (AMS)	CF, CF ₂ , CF ₃	CF ₄	116
	CH, CH ₂ , CH ₃	CH ₄	117
	SiH ₃	SiH ₄	118

1.4.4 Measurement for radical temperatures

Various diagnostics techniques have been applied to the measurement of temperature of species, as shown in Table 1.5. The measured radical temperatures generally mean translational one. However, molecular radicals have translational, rotational, vibrational, and excitation temperatures. In the previous study, Doppler broadening of absorption,^{60,123–127} or fluorescence^{128–131} were investigated to obtain the translational temperatures of radicals. On the other hand, analyses of rotational and vibrational spectra of absorption,^{37,88,117,132–136} emission,^{137–146} or fluorescence¹⁴⁴ were carried out to investigate the rotational and vibrational temperatures. Popular measurement technique for obtaining the radical temperature is the analysis of the rotational and vibrational band shapes by using OES and Fourier transform infrared spectroscopy. The translational temperature of radical is a very important factor to obtain the information of surface reaction of the radicals on the substrate. The chemisorbed flux of radicals incident on the substrate is defined as

$$\Gamma_{ads} = s\Gamma, \quad (1.1)$$

where s and Γ are the sticking coefficient and the radical flux incident on the substrate, respectively. The flux of radicals Γ incident on the solid surface is given by

$$\Gamma = \frac{1}{4} n \sqrt{\frac{8kT}{\pi m}} \quad (1.2)$$

where n , m , and k are the absolute density of radical, the mass, and Boltzmann constant, respectively. T is the translational temperature of the radical. Therefore, the translational temperature of radicals is a key parameter to determine the process feature in the plasma process, and the measurement of Doppler broadening by using the coherent light source is the most powerful technique to measure the translational temperature of selected species

directly.

Table 1.5 Various techniques for measurement of radical temperatures.

Method		Species	Reference
Rotational and vibrational spectra	Absorption	CF, CF ₂ , CF ₃ , CF ₄	84,88,132–134
		SiH ₃	37,135
		N ₂ O	136
	Optical emission	N ₂	137–140
		N ₂ ⁺	141,142
		C ₂ , CO, SiF, CN, CF	143,144
		CCl	144
		SiH	146
	Fluorescence	CH	145
		CCl	144
Doppler broadening	Absorption	CF, CF ₂ , CF ₄	124,125
		Si	126–128
		H	123
	Fluorescence	Ar ⁺ ,	128
		Fe	129
		SiH ₂	130
		CF	131

1.4.5 Measurement for radicals in SiH₄/H₂ plasma

As described in 1.3.2, the H radical is an important species in SiH₄/H₂ plasma for deposition of $\mu\text{c-Si:H}$. In order to have a better understanding of the behavior of the H radical in plasmas, the Balmer α (H α , 656.3 nm) emission has been often measured. However, the optical emission intensity does not always correspond to the density of ground-state H atoms. It has been reported that the absolute density of H radicals in SiH₄ plasmas was measured by employing the TALIF technique. However, in the TALIF method, the calibration of the absolute H radical density is usually difficult. Moreover, the laser employed in TALIF sometimes causes the dissociation of feed gases and other species in the plasmas, leading to extra H radical formation. Thus, in this study, the absolute density and translational temperature of H radicals has been measured by employing VUVAS and VUVLAS techniques.

The SiH₃ is the dominate film precursor for a-Si:H and $\mu\text{c-Si:H}$. The density of SiH₃ radicals has been measured by optical absorption spectroscopy and mass spectroscopy because the SiH₃ radical is a non-emissive species. In this study, the CRDS technique has been used to measure the density of SiH₃ radicals since the CRDS technique gives us the information of not only SiH₃ radicals but also nano-particles.¹²²

1.5 Purposes and construction of this thesis

The advantages of thin-film silicon solar cells and the plasma process are described. As mentioned above, thin-film silicon solar cells have not only cost reduction potential but also low energy payback time. The micromorph tandem solar cell is a promising high efficiency thin-film silicon solar cell, however thicker intrinsic $\mu\text{-Si:H}$ films (1–3 μm) are required. Therefore, the high-rate-deposition technique of high quality $\mu\text{-Si:H}$ is critical issue for the cost reduction of the micromorph tandem solar cell. To realize the high-rate-deposition technique, a novel deposition method should be developed based on understanding the plasma gas-phase and film properties resulting from PECVD.

The purposes of this study are to clarify the relation between behaviors of radicals in plasma and properties of deposited $\mu\text{-Si:H}$ thin films and to develop high-rate-deposition method of $\mu\text{-Si:H}$ thin films. As described in 1.3, radicals play very important role in the deposition of $\mu\text{-Si:H}$ thin films, however the quantitative information of radicals, especially H radicals, is not sufficient. To understand the relation between radicals and film property, the surface loss probability of H radicals was estimated by VUVAS, additionally H and SiH_3 radicals in capacitively coupled plasma are were measured by VUVLAS and CRDS. For development of high-rate-deposition method, H-radical-injection PECVD was proposed and the effect on the contribution of the thin-film deposition was evaluated.

In Chapter 2, theories of plasma diagnostics such as VUVAS, VUVLAS, CRDS and microwave interferometer were described. Theories of film characterization technique such as Raman spectroscopy, X-ray diffraction (XRD), Fourier transform infrared absorption spectroscopy (FTIR) and Electron spin resonance used as measurement methods of silicon thin film were introduced.

Chapter 1

In Chapter 3, the surface loss probability of H radicals was investigated in SiH₄/H₂ plasma using VUVAS. The surface loss probability was calculated from the decay curve of the H radical density in the plasma afterglow, and increased with the SiH₄ flow rate. Silicon thin films deposited on the chamber wall were analyzed to investigate the relation between the surface loss probability and the surface condition. From these results, surface loss mechanisms of H radicals were discussed.

In Chapter 4, the properties of thin-film silicon grown by PECVD were investigated with respect to the flux ratio of hydrogen radical to film precursor. The absolute density and translational temperature of H radicals in SiH₄/H₂ capacitively coupled plasma were measured using vacuum ultraviolet laser absorption spectroscopy. The effective flux of H radicals to the surface reactions was estimated from the results and the surface loss probability obtained in Chapter 3. The effective flux of film precursor for deposition was estimated from the deposition rate and the flux of SiH₃ radicals was estimated from the measurement of CRDS. The growth speed of nano-particles was also given by CRDS. From these results, the critical flux ratio of H radicals to film precursors to obtain film properties suitable for the i-layer of a solar cell was clarified. Moreover, the contribution ratio of SiH₃ to film precursors and the generation of nano-particles were discussed.

In Chapter 5, the development of a PECVD with H-radical-injection (RI-PECVD) for the high-rate deposition of $\mu\text{c-Si:H}$ thin films. As described in 1.3.3, the higher-rate-deposition (>2 nm/s) obtained by the high pressure and the high input power has problems such as the degradation of film quality and non-uniform film growth. Furthermore, the results of Chapter 4 have indicated that achieving the sufficient H radical density is crucial issue for the high-rate deposition of $\mu\text{c-Si:H}$ and the growth speed of nano-particles is significantly increased by increase in the pressure. In this study, the RI-PECVD has been developed to increase the deposition rate without increasing

Chapter 1

the pressure and input power. The RI-PECVD system has a H₂ plasma as a radical source in addition to a deposition plasma (SiH₄/H₂ plasma) and potential to increase deposition rate without increasing the pressure and the input power. The plasma parameters and resultant growth characteristics obtained with the RI-PECVD system were compared with those obtained using a conventional PECVD system. The absolute density of H radicals was measured by VUVLAS to evaluate the effect of RI-PECVD for controlling the H radical density. It has been demonstrated that RI-PECVD system enables to increase the H radical density and enhance the crystallization of silicon thin films and it is effective to increase deposition rate with keeping the crystallinity of $\mu\text{c-Si:H}$.

Finally, the results in the present study are summarized and future scope is described in Chapter 6.

1.6 References

- ¹ Kyoto Protocol, http://unfccc.int/kyoto_protocol/items/2830.php, (accessed 11/12/2012)
- ² M. Konagai, Y. Masafumi, and K. Michio, *Taiyo Denchi no Kiso to Oyo, [Basic and Application of Solar Cells]* (Baifukan, 2010).
- ³ M. Konagai, *Jpn. J. Appl. Phys.* **50**, 030001 (2011).
- ⁴ E. Becquerel, *Comptes Rendus* **9**, 561 (1839).
- ⁵ C. E. Fritts, *American Journal of Science* **26**, 465 (1883).
- ⁶ D. M. Chapin, C.S. Fuller, and G.L. Pearson, *J. Appl. Phys.* **25**, 676 (1954).
- ⁷ A. M. Barnett, R. B. Hall, D. Fardig, and J. Culik, in *Tech. Digest 2nd Int. PVSEC* (Beijing, China, 1986), p. 167.
- ⁸ C. M. Chong, S. R. Wenham, and M. A. Green, *Appl. Phys. Lett.* **52**, 407 (1988).
- ⁹ J. Meier, R. Flückiger, H. Keppner, and A. Shah, *Appl. Phys. Lett.* **65**, 860 (1994).
- ¹⁰ Y. Tsunomura, Y. Yoshimine, M. Taguchi, T. Baba, T. Kinoshita, H. Kanno, H. Sakata, E. Maruyama, and M. Tanaka, *Sol. Energy Mater. Sol. Cells* **93**, 670 (2009).
- ¹¹ M. Pagliaro, G. Palmisano, and R. Ciriminna, *Flexible Solar Cells* (Wiley-VCH, Weinheim, 2008).
- ¹² National Renewable Energy Laboratory Report No. NREL/FS-520-24619.
- ¹³ Y. Tawada and H. Yamagishi, *Sol. Energy Mater. Sol. Cells* **66**, 95 (2001).
- ¹⁴ S. W. G. Vitae, R. P. Vitae, and D. B. Vitae, *Comprehensive Renewable Energy* (Elsevier, 2012).
- ¹⁵ A. V. Shah, H. Schade, M. Vanecek, J. Meier, E. Vallat-Sauvain, N. Wyrsh, U. Kroll, C. Droz, and J. Bailat, *Prog. Photovolt: Res. Appl.* **12**, 113 (2004).
- ¹⁶ W. E. Spear and P. G. Le Comber, *Philos. Mag.* **33**, 935 (1976).

- ¹⁷ D. E. Carlson, C. R. Wronski, J. I. Pankove, P. J. Zanzucchi, and D. L. Staebler, *RCA Review* **38**, 211 (1977).
- ¹⁸ A. Catalano, R. V. D'Aiello, J. Dresner, B. Faughnan, A. Firester, J. Kane, H. Schade, G. Schwartz, Z.E. Smith, and A. Triano, in *16th IEEE Photovoltaic Specialists Conference* (San Diego, 1982), pp. 1421–1422.
- ¹⁹ S. Vepřek and V. Mareček, *Solid-State Electronics* **11**, 683 (1968).
- ²⁰ S. Usui and M. Kikuchi, *J. Non-Cryst. Solids* **34**, 1 (1979).
- ²¹ W. E. Spear, G. Willeke, P. G. Le Comber, and A. G. Fitzgerald, *Le Journal De Physique Colloques* **42**, 257 (1981).
- ²² J. Meier, P. Torres, R. Platz, S. Dubail, U. Kroll, J. A. A. Selvan, N. P. Vaucher, C. Hof, D. Fischer, H. Keppner, A. Shah, K.-D. Ufert, P. Giannoulès, and J. Koehler, *Proceedings of the Materials Research Society Symposium* **420**, 3 (1996).
- ²³ U. Kroll, J. Meier, H. Keppner, S. D. Littlewood, I. E. Kelly, P. Giannoulès, and A. Shah, *Proceedings of the Materials Research Society Symposium* **377**, 39 (1995).
- ²⁴ U. Kroll, *J. Vac. Sci. Technol. A* **13**, 2742 (1995).
- ²⁵ P. Torres, J. Meier, R. Flückiger, U. Kroll, J. a. A. Selvan, H. Keppner, A. Shah, S.D. Littlewood, I.E. Kelly, and P. Giannoulès, *Appl. Phys. Lett.* **69**, 1373 (1996).
- ²⁶ A Shah, *Sol. Energy Mater. Sol. Cells* **78**, 469 (2003).
- ²⁷ A. Matsuda, *J. Non-Cryst. Solids* **338-340**, 1 (2004).
- ²⁸ T. Moustakas, *Semiconductors and Semimetals 21A* (Academic Press, New York, 1984), p. 55.
- ²⁹ T. Saitoh, S. Muramatsu, T. Shimada, and M. Migitaka, *Appl. Phys. Lett.* **42**, 678 (1983).
- ³⁰ T. Fuyuki, K.-Y. Du, S. Okamoto, S. Yasuda, T. Kimoto, M. Yoshimoto, and H. Matsunami, *J. Appl. Phys.* **64**, 2380 (1988).

- ³¹ Y. Mishima, M. Hirose, Y. Osaka, K. Nagamine, Y. Ashida, N. Kitagawa, and K. Isogaya, *Jpn. J. Appl. Phys.* **22**, L46 (1983).
- ³² A. H. Mahan, B. P. Nelson, S. Salamon, and R. S. Crandall, *MRS Proceedings* **219**, (1991).
- ³³ M. Tsuda, S. Oikawa, and K. Sato, *J. Chem. Phys.* **91**, 6822 (1989).
- ³⁴ J. Perrin, O. Leroy, and M. C. Bordage, *Contrib. Plasma Phys.* **36**, 3 (1996).
- ³⁵ E. Meeks, *J. Vac. Sci. Technol. A* **16**, 544 (1998).
- ³⁶ M. A. Lieberman and A. J. Lichtenberg, *Principles of Plasma Discharges and Materials Processing*, Second edition (John Wiley & Sons, Inc., New York, 2005).
- ³⁷ N. Itabashi, N. Nishiwaki, M. Magane, S. Naito, T. Goto, A. Matsuda, C. Yamada, and E. Hirota, *Jpn. J. Appl. Phys.* **29**, L505 (1990).
- ³⁸ J. Perrin, M. Shiratani, P. Kae-Nune, H. Videlot, J. Jolly, and J. Guillon, *J. Vac. Sci. Technol. A* **16**, 278 (1998).
- ³⁹ A. Matsuda, *J. Non-Cryst. Solids* **59-60**, 767 (1983).
- ⁴⁰ A. Matsuda, K. Nomoto, Y. Takeuchi, A. Suzuki, A. Yuuki, and J. Perrin, *Surf. Sci.* **227**, 50 (1990).
- ⁴¹ G. Ganguly and A. Matsuda, *Physical Review B* **47**, 3661 (1993).
- ⁴² C. C. Tsai, G. B. Anderson, R. Thompson, and B. Wacker, *J. Non-Cryst. Solids* **114**, 151 (1989).
- ⁴³ K. Nakamura, K. Yoshino, S. Takeoka, and I. Shimizu, *Jpn. J. Appl. Phys.* **34**, 442 (1995).
- ⁴⁴ A. Matsuda, *Thin Solid Films* **337**, 1 (1999).
- ⁴⁵ K. Saitoh, M. Kondo, M. Fukawa, T. Nishimiya, W. Futako, I. Shimizu, and A. Matsuda, *MRS Proceedings* **507**, 843 (1998).
- ⁴⁶ M. Kondo, M. Fukawa, L. Guo, and A. Matsuda, *J. Non-Cryst. Solids* **266-269**, 84 (2000).

- ⁴⁷ S. Hamma and P. Roca i Cabarrocas, *Sol. Energy Mater. Sol. Cells* **69**, 217 (2001).
- ⁴⁸ Y. Sobajima, T. Higuchi, J. Chantana, T. Toyama, C. Sada, A. Matsuda, and H. Okamoto, *Physica Status Solidi (c)* **4**, 521 (2010).
- ⁴⁹ C. Niikura, M. Kondo, and A. Matsuda, *J. Non-Cryst. Solids* **338-340**, 42–46 (2004).
- ⁵⁰ J. W. Coburn and M. Chen, *J. Appl. Phys.* **51**, 3134 (1980).
- ⁵¹ K. Sasaki, Y. Kawai, and K. Kadota, *Appl. Phys. Lett.* **70**, 1375 (1997).
- ⁵² P. D. Hanish, *J. Vac. Sci. Technol. A* **13**, 1802 (1995).
- ⁵³ J.-S. Jenq, J. Ding, J. W. Taylor, and N. Hershkowitz, *Plasma Sources Sci. Technol.* **3**, 154 (1994).
- ⁵⁴ V. M. Donnelly, D. L. Flamm, W. C. Dautremont-Smith, and D. J. Werder, *J. Appl. Phys.* **55**, 242 (1984).
- ⁵⁵ R. A. Gottscho and V. M. Donnelly, *J. Appl. Phys.* **56**, 245 (1984).
- ⁵⁶ Y. Kawai, K. Sasaki, and K. Kadota, *Jpn. J. Appl. Phys.* **36**, L1261 (1997).
- ⁵⁷ L. St-Onge and M. Moisan, *Plasma Chemistry and Plasma Processing* **14**, 87 (1994).
- ⁵⁸ M. Sakakibara, M. Hiramatsu, and T. Goto, *J. Appl. Phys.* **69**, 3467 (1991).
- ⁵⁹ Y. Yamamoto, M. Hori, and T. Goto, *J. Vac. Sci. Technol. A* **14**, 1999 (1996).
- ⁶⁰ M. Hiramatsu, M. Sakakibara, M. Mushiga, and T. Goto, *Meas. Sci. Technol.* **2**, 1017 (1991).
- ⁶¹ K. Tachibana and H. Kamisugi, *Appl. Phys. Lett.* **74**, 2390 (1999).
- ⁶² N. Tanaka and K. Tachibana, *J. Appl. Phys.* **92**, 5684 (2002).
- ⁶³ K. Tachibana, *Plasma Sources Sci. Technol.* **11**, A166 (2002).
- ⁶⁴ H. Umemoto, K. Ohara, D. Morita, Y. Nozaki, A. Masuda, and H. Matsumura, *J. Appl. Phys.* **91**, 1650 (2002).
- ⁶⁵ K. Takeda, S. Takashima, M. Ito, and M. Hori, *Appl. Phys. Lett.* **93**, 021501 (2008).
- ⁶⁶ S. Takashima, M. Hori, T. Goto, A. Kono, M. Ito, and K. Yoneda, *Appl. Phys. Lett.* **75**, 3929 (1999).

Chapter 1

- ⁶⁷ S. Takashima, M. Hori, T. Goto, and K. Yoneda, *J. Appl. Phys.* **89**, 4727 (2001).
- ⁶⁸ S. Takashima, M. Hori, T. Goto, A. Kono, and K. Yoneda, *J. Appl. Phys.* **90**, 5497 (2001).
- ⁶⁹ H. Ito, K. Teii, M. Ishikawa, M. Ito, M. Hori, T. Takeo, T. Kato, and T. Goto, *Jpn. J. Appl. Phys.* **38**, 4504 (1999).
- ⁷⁰ S. Takashima, S. Arai, M. Hori, T. Goto, A. Kono, M. Ito, and K. Yoneda, *J. Vac. Sci. Technol. A* **19**, 599 (2001).
- ⁷¹ S. Tada, S. Takashima, M. Ito, M. Hori, T. Goto, and Y. Sakamoto, *J. Appl. Phys.* **88**, 1756 (2000).
- ⁷² H. Nagai, M. Hiramatsu, M. Hori, and T. Goto, *Rev. Sci. Instrum.* **74**, 3453 (2003).
- ⁷³ J. P. Booth, O. Joubert, J. Pelletier, and N. Sadeghi, *J. Appl. Phys.* **69**, 618 (1991).
- ⁷⁴ K. Tachibana, *Jpn. J. Appl. Phys.* **33**, 4329 (1994).
- ⁷⁵ J. Jolly and J. P. Booth, *J. Appl. Phys.* **97**, 103305 (2005).
- ⁷⁶ L. Chérigier, U. Czarnetzki, D. Luggenhölscher, V. Schulz-von der Gathen, and H. F. Döbele, *J. Appl. Phys.* **85**, 696 (1999).
- ⁷⁷ B. L. Preppernau, *J. Vac. Sci. Technol. A* **8**, 1673 (1990).
- ⁷⁸ S. Mazouffre, C. Foissac, P. Supiot, P. Vankan, R. Engeln, D. C. Schram, and N. Sadeghi, *Plasma Sources Sci. Technol.* **10**, 168 (2001).
- ⁷⁹ E. J. H. Collart, J. A. G. Baggerman, and R. J. Visser, *J. Appl. Phys.* **78**, 47 (1995).
- ⁸⁰ A. D. Tserepi and T. A. Miller, *Journal of Applied Physics* **77**, 505 (1995).
- ⁸¹ J. Matsushita, K. Sasaki, and K. Kadota, *Jpn. J. Appl. Phys.* **36**, 4747 (1997).
- ⁸² R. E. Walkup, K. L. Saenger, and G. S. Selwyn, *J. Chem. Phys.* **84**, 2668 (1986).
- ⁸³ B. A. Cruden and M. Meyyappan, *J. Appl. Phys.* **97**, 084311 (2005).
- ⁸⁴ J. Luque, E. A. Hudson, and J. P. Booth, *J. Chem. Phys.* **118**, 622 (2003).
- ⁸⁵ N. Bulcourt, J. P. Booth, E. A. Hudson, J. Luque, D. K. W. Mok, E. P. Lee, F. T. Chau, and J. M. Dyke, *The Journal of Chemical Physics* **120**, 9499 (2004).

- ⁸⁶ W. L. Perry, K. Waters, M. Barela, and H. M. Anderson, *J. Vac. Sci. Technol. A* **19**, 2272 (2001).
- ⁸⁷ K. Miyata, M. Hori, and T. Goto, *J. Vac. Sci. Technol. A* **15**, 568 (1997).
- ⁸⁸ M. E. Littau, M. J. Sowa, and J. L. Cecchi, *J. Vac. Sci. Technol. A* **20**, 1603 (2002).
- ⁸⁹ K. Miyata, M. Hori, and T. Goto, *Jpn. J. Appl. Phys.* **36**, 5340 (1997).
- ⁹⁰ K. Miyata, K. Takahashi, S. Kishimoto, M. Hori, and T. Goto, *Jpn. J. Appl. Phys.* **34**, L444 (1995).
- ⁹¹ N. Itabashi, K. Kato, N. Nishiwaki, T. Goto, C. Yamada, and E. Hirota, *Jpn. J. Appl. Phys.* **27**, L1565 (1988).
- ⁹² Y. Yamamoto, H. Nomura, T. Tanaka, M. Hiramatsu, M. Hori, and T. Goto, *Jpn. J. Appl. Phys.* **33**, 4320 (1994).
- ⁹³ S. Naito, M. Ikeda, N. Ito, T. Hattori, and T. Goto, *Jpn. J. Appl. Phys.* **32**, 5721 (1993).
- ⁹⁴ M. Ikeda, K. Aiso, M. Hori, and T. Goto, *Jpn. J. Appl. Phys.* **34**, 3273 (1995).
- ⁹⁵ K. Tachibana, T. Shirafuji, and Y. Matsui, *Jpn. J. Appl. Phys.* **31**, 2588 (1992).
- ⁹⁶ A. O'Keefe and D. A. G. Deacon, *Rev. Sci. Instrum.* **59**, 2544 (1988).
- ⁹⁷ M. G. H. Boogaarts, P. J. Böcker, W. M. M. Kessels, D. C. Schram, and M. C. M. van de Sanden, *Chemical Physics Letters* **326**, 400 (2000).
- ⁹⁸ W. M. M. Kessels, J. P. M. Hoefnagels, M. G. H. Boogaarts, D. C. Schram, and M. C. M. van de Sanden, *J. Appl. Phys.* **89**, 2065 (2001).
- ⁹⁹ P. Zalicki, Y. Ma, R. N. Zare, E. H. Wahl, J. R. Dadamio, T.G. Owano, and C. H. Kruger, *Chemical Physics Letters* **234**, 269 (1995).
- ¹⁰⁰ R. Engeln, K. G. Y. Letourneur, M. G. H. Boogaarts, M. C. M. van de Sanden, and D. C. Schram, *Chemical Physics Letters* **310**, 405 (1999).
- ¹⁰¹ R. Engeln, G. von Helden, G. Berden, and G. Meijer, *Chemical Physics Letters* **262**, 105 (1996).

Chapter 1

- ¹⁰² R. Engeln and G. Meijer, *Rev. Sci. Instrum.* **67**, 2708 (1996).
- ¹⁰³ R. Engeln, G. Berden, R. Peeters, and G. Meijer, *Rev. Sci. Instrum.* **69**, 3763 (1998).
- ¹⁰⁴ N. M. Mackie, V. A. Ventura, and E. R. Fisher, *The Journal of Physical Chemistry B* **101**, 9425 (1997).
- ¹⁰⁵ G. A. Hebner, *J. Appl. Phys.* **89**, 900 (2001).
- ¹⁰⁶ P. J. Hargis, *Appl. Phys. Lett.* **40**, 779 (1982).
- ¹⁰⁷ K. Ninomiya, K. Suzuki, S. Nishimatsu, and O. Okada, *J. Vac. Sci. Technol. A* **4**, 1791 (1986).
- ¹⁰⁸ J. P. Booth, G. Hancock, N. D. Perry, and M. J. Toogood, *J. Appl. Phys.* **66**, 5251 (1989).
- ¹⁰⁹ C. Suzuki, K. Sasaki, and K. Kadota, *J. Appl. Phys.* **82**, 5321 (1997).
- ¹¹⁰ A. Kono, N. Koike, K. Okuda, and T. Goto, *Jpn. J. Appl. Phys.* **32**, L543 (1993).
- ¹¹¹ H. Nomura, K. Akimoto, A. Kono, and T. Goto, *J. Phys. D: Appl. Phys.* **28**, 1977 (1995).
- ¹¹² C. W. Watson and K. G. McKendrick, *Chem. Phys.* **187**, 87 (1994).
- ¹¹³ A. C. Stanton, A. Freedman, J. Wormhoudt, and P. P. Gaspar, *Chemical Physics Letters* **122**, 190 (1985).
- ¹¹⁴ M. Nakamura, M. Hori, T. Goto, M. Ito, and N. Ishii, *Jpn. J. Appl. Phys.* **40**, 4730 (2001).
- ¹¹⁵ K. Tachibana, T. Mukai, A. Yuuki, Y. Matsui, and H. Harima, *Jpn. J. Appl. Phys.* **29**, 2156 (1990).
- ¹¹⁶ Y. Hikosaka, M. Nakamura, and H. Sugai, *Jpn. J. Appl. Phys.* **33**, 2157 (1994).
- ¹¹⁷ H. Sugai and H. Toyoda, *J. Vac. Sci. Technol. A* **10**, 1193 (1992).
- ¹¹⁸ T. Kuroda, M. Ikeda, T. Ishijima, and H. Toyoda, *Jpn. J. Appl. Phys.* **50**, 08JB05 (2011).
- ¹¹⁹ E. Stoffels, W.W. Stoffels, and K. Tachibana, *Rev. Sci. Instrum.* **69**, 116 (1998).

- ¹²⁰ K. Teii, M. Hori, M. Ito, T. Goto, and N. Ishii, *J. Vac. Sci. Technol. A* **18**, 1 (2000).
- ¹²¹ M. Nakamura, Y. Hirano, Y. Shiokawa, M. Takayanagi, and M. Nakata, *J. Vac. Sci. Technol. A* **24**, 385 (2006).
- ¹²² T. Nagai, A. H. M. Smets, and M. Kondo, *Jpn. J. Appl. Phys.* **47**, 7032 (2008).
- ¹²³ D. Wagner, B. Dikmen, and H. F. Döbele, *Rev. Sci. Instrum.* **67**, 1800 (1996).
- ¹²⁴ M. Nakamura, M. Hori, T. Goto, M. Ito, and N. Ishii, *J. Appl. Phys.* **90**, 580 (2001).
- ¹²⁵ M. Haverlag, *J. Vac. Sci. Technol. A* **14**, 380 (1996).
- ¹²⁶ T. Ohta, M. Hori, T. Ishida, T. Goto, M. Ito, S. Kawakami, and N. Ishii, *Jpn. J. Appl. Phys.* **42**, L1532 (2003).
- ¹²⁷ T. Tanaka, M. Hiramatsu, M. Nawata, A. Kono, and T. Goto, *J. Phys. D: Appl. Phys.* **27**, 1660 (1994).
- ¹²⁸ G. A. Hebner, *J. Appl. Phys.* **80**, 2624 (1996).
- ¹²⁹ K. Shibagaki, N. Nafarizal, and K. Sasaki, *J. Appl. Phys.* **98**, 043310 (2005).
- ¹³⁰ A. Kono, S. Hirose, K. Kinoshita, and T. Goto, *Jpn. J. Appl. Phys.* **37**, 4588 (1998).
- ¹³¹ H. Abada, P. Chabert, J. P. Booth, J. Robiche, and G. Cartry, *J. Appl. Phys.* **92**, 4223 (2002).
- ¹³² M. Haverlag, *J. Vac. Sci. Technol. A* **9**, 327 (1991).
- ¹³³ M. Magane, N. Itabashi, N. Nishiwaki, T. Goto, C. Yamada, and E. Hirota, *Jpn. J. Appl. Phys.* **29**, L829 (1990).
- ¹³⁴ K. Maruyama, A. Sakai, and T. Goto, *J. Phys. D: Appl. Phys.* **26**, 199 (1993).
- ¹³⁵ N. Itabashi, K. Kato, N. Nishiwaki, T. Goto, C. Yamada, and E. Hirota, *Jpn. J. Appl. Phys.* **28**, L325 (1989).
- ¹³⁶ T. A. Cleland and D. W. Hess, *J. Appl. Phys.* **64**, 1068 (1988).
- ¹³⁷ V. M. Donnelly and M. V. Malyshev, *Appl. Phys. Lett.* **77**, 2467 (2000).
- ¹³⁸ R. A. Porter and W. R. Harshbarger, *J. Electrochem. Soc.* **126**, 460 (1979).

Chapter 1

- ¹³⁹ E. M. van Veldhuizen, T. Bisschops, E. J. W. van Vliembergen, and J. H. M. C. van Wolput, *J. Vac. Sci. Technol. A* **3**, 2205 (1985).
- ¹⁴⁰ A. Chelouah, E. Marode, G. Hartmann, and S. Achat, *J. Phys. D: Appl. Phys.* **27**, 940 (1994).
- ¹⁴¹ H. H. Brömer and F. Spieweck, *Zeitschrift Für Physik* **184**, 481 (1965).
- ¹⁴² B. A. Cruden, M. V. V. S. Rao, S. P. Sharma, and M. Meyyappan, *J. Appl. Phys.* **91**, 8955 (2002).
- ¹⁴³ M. Oshima, *Jpn. J. Appl. Phys.* **17**, 1157 (1978).
- ¹⁴⁴ G. P. Davis and R. A. Gottscho, *J. Appl. Phys.* **54**, 3080 (1983).
- ¹⁴⁵ J. Luque, M. Kraus, A. Wokaun, K. Haffner, U. Kogelschatz, and B. Eliasson, *J. Appl. Phys.* **93**, 4432 (2003).
- ¹⁴⁶ S. Stamou, D. Mataras, and D. Rapakoulias, *J. Phys. D: Appl. Phys.* **31**, 2513 (1998).

Chapter 2 Plasma Diagnostic Techniques and Film Characterization Methods

2.1 Introduction

Plasma processing has been used for the manufacturing of solar cell devices. In order to improve conversion efficiency and reduce production cost, the deposition process realizing the more high film quality and the more high deposition rate have been required. Approaches to understand plasma deposition processes are categorized to plasma diagnostic and surface characterization.

In this chapter, the experimental systems, diagnostic techniques of plasma and film analysis method are described. Vacuum ultraviolet absorption spectroscopy (VUVAS), vacuum ultraviolet laser absorption spectroscopy (VUVLAS), cavity ring-down spectroscopy (CRDS) were used for measurement of radical densities in plasma. In order to obtain information of the crystallinity, crystalline orientation and defect density of deposited films, Raman spectroscopy, X-ray diffraction (XRD) and electron spin resonance (ESR) were employed. Post-deposition oxidation of films was evaluated by Fourier-transform infrared spectroscopy (FTIR). The microstructure of films was observed by transmission electron microscopy (TEM). On the basis of analysis resulting from these measurements, it could be expected to realize the development of sophisticated plasma deposition for the next generation process.

2.2 Plasma diagnostic techniques

2.2.1 Theory of absorption spectroscopy

Optical measurement techniques such as absorption spectroscopy and emission spectroscopy are very powerful for detecting the behaviors of activated species without the disturbance of process plasmas. Recently, these techniques have employed the light in the optical range between vacuum ultraviolet (VUV) and infrared (IR) for probing atomic and molecular radicals. If the parallel light from a source passes through an absorption cell, such as plasma, the intensity of the transmitted light is given as follows¹,

$$I(\nu) = I_0(\nu) \exp[-k(\nu)L], \quad (2.1)$$

where ν is the frequency, $I(\nu)$ and $I_0(\nu)$ are the intensities of the transmitting light and the incident light, respectively. L is the absorption path length, and $k(\nu)$ is the absorption coefficient as a function of frequency ν .

The broadening of the absorption coefficient, that is, the broadening of the absorption line-profile is due to the causes as follows,

- (1) Natural broadening due to the finite lifetime of the excited state.
- (2) Doppler effect broadening due to the motions of the atoms.
- (3) Lorentz broadening due to collisions with foreign gases.
- (4) Holtsmark broadening due to collisions with other absorption atoms of the same kind.
- (5) Stark effect broadening due to collisions with electrons and ions.

However, in this study the Doppler broadening should be taken into account, because collision frequency, the density of the electron and absorbing atoms of the same kind

should be low.

Here, we consider that a parallel beam of the light of frequency ν passed through a layer of atoms bounded by the planes at the length of dL . Suppose there are N_1 normal atoms per cm^3 of which dN_1 are capable of absorbing the frequency range between ν and $\nu+d\nu$, and N_u excited atoms of which dN_u are capable of emitting this frequency range. Neglecting the effect of spontaneous re-emission in view of the fact that it takes place in all direction, the decrease in energy of the beam is given by

$$-[I(\nu)]d\nu = dN_1 dL \rho(\nu) B_{lu} h\nu - dN_u dL \rho(\nu) B_{ul} h\nu, \quad (2.2)$$

where B_{lu} and B_{ul} are Einstein B coefficient from ground state l to excited state u and from u to l, respectively. h is Planck's constant, and $\rho(\nu)$ is the radiation energy density given by $I(\nu)=c\rho(\nu)$, (c : light velocity). Rewriting Eq. (2.2), we obtain

$$-\frac{1}{I(\nu)} \frac{d[I(\nu)]}{dL} d\nu = \frac{h\nu}{c} (B_{lu} dN_1 - B_{ul} dN_u). \quad (2.3)$$

Recognizing that the left-hand term is $k(\nu)d\nu$ as defined by Eq. (2.1), Eq. (2.3) becomes

$$k(\nu)d\nu = \frac{h\nu}{c} (B_{lu} dN_1 - B_{ul} dN_u). \quad (2.4)$$

Integrating over the whole absorption line, neglecting the slight variation in ν throughout the line,

$$\int k(\nu)d\nu = \frac{h\nu_0}{c} (B_{lu} N_1 - B_{ul} N_u), \quad (2.5)$$

where ν_0 is the frequency at the center of the line. Here we use the Einstein A coefficient.

$$\begin{aligned} \int k(\nu)d\nu &= \frac{c^2}{8\pi\nu_0^2} \frac{g_u}{g_l} AN_1 \left(1 - \frac{g_l N_u}{g_u N_1}\right) \\ &\cong \frac{c^2}{8\pi\nu_0^2} \frac{g_u}{g_l} AN_1 \quad (N_u \ll N_1), \end{aligned} \quad (2.6)$$

where g_l and g_u are the statistical weights of the lower and upper level, respectively.

Therefore, by measuring $I_0(\nu)$ and $I(\nu)$, $k(\nu)$ is decided and we can estimate the density N_1 .

The intensity of measured light is the integrated value over the frequency

$$I_0 = \int e_0 f_0(\nu) d\nu, \quad (2.7)$$

$$I_a = \int e_0 f_0(\nu) \{1 - \exp[-k_0 f_a(\nu)L]\} d\nu, \quad (2.8)$$

where I_0 and I_a are the intensities of the incident light and the absorption, respectively, $f_0(\nu)$ is the emission line-profile function for the light source, e_0 is the emission intensity of the light source at a center frequency of $f_0(\nu)$, $f_a(\nu)$ is the absorption line-profile function, and k_0 is the absorption coefficient at the center frequency of $f_a(\nu)$. The intensity of absorbed light $A(k_0L)$ is given by the following equation.

$$A(k_0L) = 1 - \frac{I_a}{I_0} = \frac{\int f_0(\nu) \{1 - \exp[-k_0 f_a(\nu)L]\} d\nu}{\int f_0(\nu) d\nu}, \quad (2.9)$$

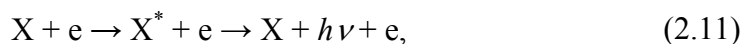
From $A(k_0L)$ obtained by measurement, k_0 is determined by assuming the line-profile function $f_0(\nu)$ and $f_a(\nu)$. Then, the number density of state 1, N_1 , is estimated by using Eq. (2.6) as

$$N_1 = \frac{8\pi\nu_0^2}{c^2} \frac{g_l}{g_u} \frac{1}{A} k_0 \int f_a(\nu) d\nu. \quad (2.10)$$

2.2.2 VUVAS using micro-discharge hollow cathode lamp (MHCL)

Recently, the measurement system of absolute densities of atomic H, N and O radicals in the ground state using the VUVAS with micro-discharge hollow cathode lamp (MHCL) as a light source has been developed.²⁻⁴ Transition lines used for measuring the absolute densities of H, N and O radicals are Lyman α at 121.6 nm, $^4P_{5/2} - ^4S^{\circ}_{3/2}$, $^4P_{3/2} - ^4S^{\circ}_{3/2}$ and $^4P_{1/2} - ^4S^{\circ}_{3/2}$ at 120.0 nm and $^3S^{\circ} - 2p^4 \ ^3P_2$ at 130.217 nm, $3s \ ^3S^{\circ} - 2p^4$

3P_1 130.487 nm and $3s\ ^3S^0-2p^4\ ^3P_0$ 130.604 nm, respectively. Each emission of these transition lines can be obtained by the H_2 , N_2 and O_2 plasma, respectively. However, these emissions are caused by two major processes.⁵⁻⁷ One is the direct excitation of ground state atomic radicals by the electron impact.



where X is the atomic radical of interest, X^* is X atoms in the excited state. The other is the dissociative excitation of ground state of X_2 by the electron impact.



Reaction (2.11) is responsible for the production of slow excited X^* atoms. Reaction (2.12) can produce fast excited X atoms which produce a large Doppler broadening. Therefore, the structure of the atomic radical emission line profile consists of a two-component velocity distribution arising from two different excitation processes as shown in Eqs. (2.11) and (2.12). It is difficult to estimate the emission line profile, which involves a two-component velocity distribution.

In the view of problem above in the measurement of absolute atomic radical density, a high pressure MHCL as a light source for VUVAS has been developed. The specific merits of the MHCL we expect are as follows,

- (1) The emission line profile will not involve a large Doppler shift due to the fast excited atomic radical arising from dissociative excitation of molecules, since they should be thermalized before they emit light.
- (2) The size of the hollow cathode is as small as 0.1 mm diameter, resulting in a high current density in the cathode, which is favorable for attaining a high dissociation degree of molecules and obtaining spectrally pure atomic radical emission.
- (3) A point-source-like emission from a micro-hollow can be efficiently coupled to the entrance slit of a monochromator using an appropriate lens system.
- (4) The lamp is compact and is operated with an inexpensive dc power source.

Chapter 2

The cathode and anode consist of a plate with 0.5 mm thickness with a through-hole hollow of 0.1 mm in diameter. Helium (250 sccm) and helium gas containing a small amount of H₂ and N₂ gas (5 sccm) were used. The MHCL was operated at a total pressure of 0.1 MPa. Figure 2.1 shows the image view of the MHCL.

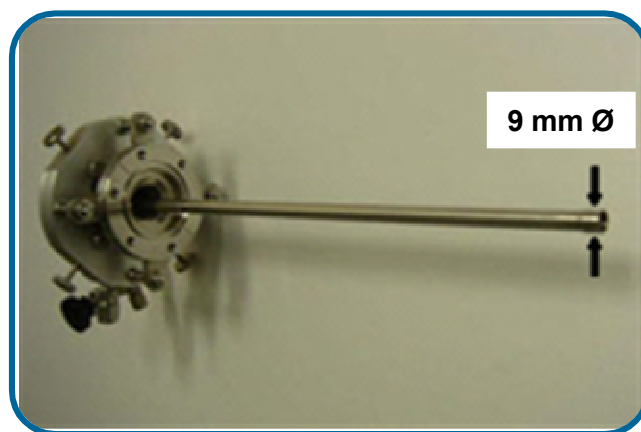


Fig. 2.1 Image view of MHCL

2.2.3 VUVLAS using tunable VUV laser system

A non-linear frequency mixing technique in gases is a well-established method for the generation of optical radiation in the spectral region of the VUV at wavelength from 100 to 200 nm. Pioneering works in the field were published more than 30 years ago⁸⁻¹³.

In this study, we used the non-linear mixing technique for generating the tunable VUV laser radiation. Figure 2.2 shows a schematic diagram of two-photon resonant four-wave frequency mixing technique. In this technique, two-photon resonant line is used for exciting to intermediate state. In Chapter 4 and 5, VUVLAS technique was applied for measuring absolute concentrations of ground state atomic H radical in the SiH₄/H₂ plasma. We used the two-photon resonant four-wave frequency mixing technique ($\omega_{\text{VUV}} = 2\omega_1 - \omega_2$) in krypton (Kr) gas for generating the tunable VUV laser radiation. Therefore, the two-photon resonance 4p-5p[1/2, 0] of Kr was used for exciting to the intermediate state in this conversion technique. Two dye lasers (COHERENT ScanMatePro), which are pumped by XeCl excimer laser (COHERENT COMPexPro 201 XeCl) radiation, generate the laser radiations of frequency ω_1 and ω_2 . The wavelength λ_1 of ω_1 was 212.56 nm which was generated by frequency doubling the dye laser output in the BBO1 and the wavelength λ_2 of ω_2 was ~844 nm. These laser radiations were focused on the Kr gas in a cell (20 Torr) with a lens (f=40 cm) through the quartz window. In this case, due to the adjustment of the frequency of ω_1 to an exact two-photon resonance, the photoionization current of Kr gas was monitored. In the measurement of absolute ground state atomic H radical concentration, the second dye laser was operated to generate $\lambda_2=844.6$ nm which correspond to the resonance line (Lyman α) of ground state.

Figure 2.3 shows the schematic illustration of the effect of the background absorption in the cases of that (a) background absorption of molecules or radicals

Chapter 2

produced in plasma is higher than the source gas and (b) background absorption of molecules or radicals produced in plasma is lower than the source gas. In both cases, by scanning the laser wavelength λ , we can obtain the absorption line profile without any effect of background absorption.¹⁴

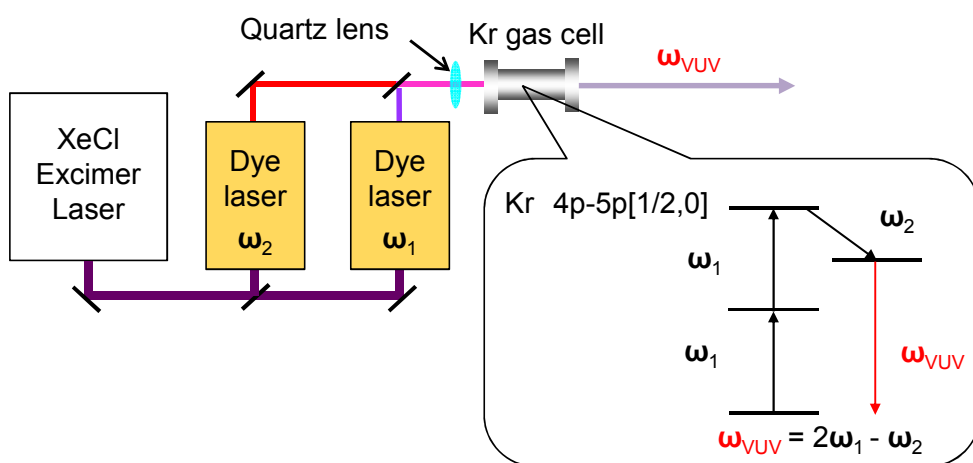


Fig. 2.2 Schematic diagram of two-photon resonant four-wave frequency mixing technique.

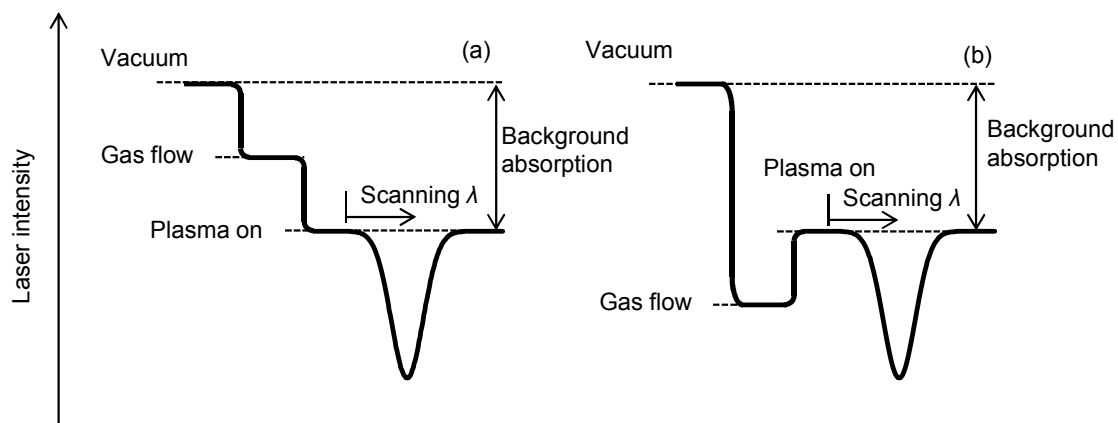


Fig. 2.3 Schematic illustration of behavior of laser intensity (a) background absorption of molecules or radicals produced in plasma is higher than that of source gas (b) background absorption of molecules or radicals produced in plasma is lower than that of source gas.

2.2.4 Cavity ring-down spectroscopy (CRDS)

CRDS is a very powerful technique for detecting small fractional absorbing species. The availability of the cavity ring down technique in the last decade¹⁵ enables an important step forward in the in situ detection of key radicals in low-temperature plasma processing^{16–20}. The highly sensitive CRD technique which was demonstrated by O’Keefe and Deacon is based on the measurement of the rate of absorption of a light pulse confined in a closed optical cavity²¹.

Figure 2.4 shows the schematic illustration of CRDS. The optical cavity consists of two highly reflective plano-concave mirrors. The light intensity leaking out of the cavity is represented by

$$I_t = I_0 \exp\left(-\frac{t}{\tau}\right), \quad (2.13)$$

and the ring-down time τ is given by

$$\tau = \frac{l/c}{L_{\text{tot}}} = \frac{l/c}{L_0 + L_{\text{abs}} + L_{\text{sca}}}, \quad (2.14)$$

where l is the cavity length, c is the light velocity, L_{tot} is the total cavity loss, L_0 is the primary cavity loss, L_{abs} is the cavity loss due to light absorption by species in the cavity, and L_{sca} is the cavity loss due to light scattering at species in the cavity. In the absence of any absorbing or scattering species between the cavity mirrors, τ is determined by L_0 , which only depends on the small transmittance and diffraction loss of the mirrors

$$L_0 = 1 - R, \quad (2.15)$$

where R is reflection ratio of the mirrors or $(1-R)$ is the effective transmittance of the mirrors. The $L_{\text{abs},i}$ and $L_{\text{sca},i}$ of species i distributed over a width d are given by

$$L_{\text{abs}} = k_i(\nu)d_{\text{abs},i} = N_{\text{abs},i}\sigma_{\text{abs},i}(\nu)d_{\text{abs},i} \quad (2.16)$$

and

$$L_{\text{sca}} = N_{\text{sca},i}\sigma_{\text{sca},i}d_{\text{sca},i} \quad (2.17)$$

respectively, where $N_{\text{abs},i}$ and $N_{\text{sca},i}$ are the densities of the absorbing and scattering species of type i , and $\sigma_{\text{abs},i}(\nu)$ and $\sigma_{\text{sca},i}$ are the cross sections for light absorbing and scattering at species of type i , respectively. The cavity loss, defined in this paper as $(L_{\text{tot}}-L_0)$, reflects the light losses at species and is described by

$$L_{\text{tot}} - L_0 = \sum_i L_{\text{abs},i} + \sum_i L_{\text{sca},i} \quad (2.18)$$

SiH_3 radicals absorb light via the $\tilde{A}^2 A'_1 \leftarrow \tilde{X}^2 A_1$ transition. This is a broadband featureless absorption spectrum ranging from ~ 200 to ~ 260 nm. In this study, the density of SiH_3 radicals was estimated from

$$N(\text{SiH}_3) = L_{\text{abs}} / \sigma_{\text{SiH}_3} d, \quad (2.19)$$

where σ_{SiH_3} is $\sigma_{\text{abs},i}(\nu)$ for SiH_3 radicals of at $1.9 \times 10^{-17} \text{ cm}^2$ at 220 nm.

In this study, the laser light pulse was obtained by optical parametric oscillator laser (Spectra Physics, versaScan500MB) pumping by 355 nm pulses generated by the frequency-tripled output of a Nd:YAG laser (Spectra Physics, Quanta-Ray PRO).

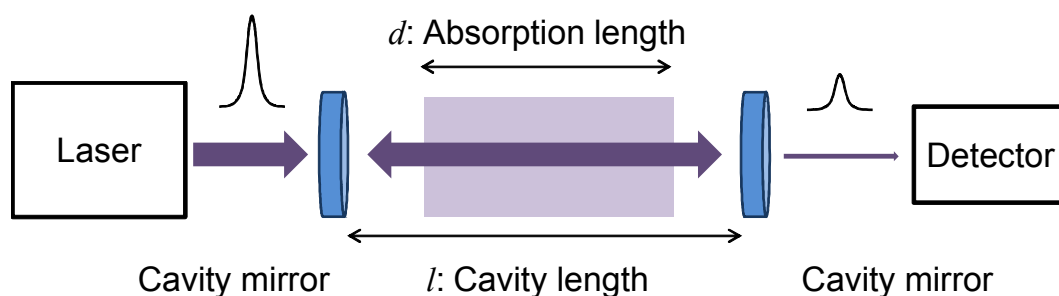


Fig. 2.4 Schematic illustration of CRDS.

2.2.5 Optical emission spectroscopy (OES)

Many optical emissions originating from excited species (e.g. atomic and molecular radicals) are generally observed in the plasma. Specific species is identified by the photon energy of the optical emission. Excited species are generated by various processes such as electron collision, dissociation, impact of other excited species, photon absorption, etc. Generally, excitation by electron impact frequently occurs in the plasma. Electron impact excitation of the ground state is given by



where X is the species of interest. De-excitation is followed by the emission of a photon from the excited state as,



The intensity of the optical emission due to the transition from an excited state to the ground state is given by

$$I_x \propto n_e n_X \int \sigma_X(\varepsilon) \nu(\varepsilon) f_e(\varepsilon) d\varepsilon = k_{eX} n_e n_X, \quad (2.22)$$

where n_e is the electron density, n_X is the concentration of X , $\sigma_X(\varepsilon)$ is the collision cross section for the electron impact excitation of X as a function of electron energy ε , $\nu(\varepsilon)$ is the electron velocity and $f_e(\varepsilon)$ is the electron energy distribution function (EEDF). $k_{eX}(\varepsilon)$ is the excitation rate coefficient for X^* by the electron impact on X . Under the condition where k_{eX} and n_e are kept constant, the emission intensity is proportional to the concentration of species. However, both of them are affected by the experimental conditions and are generally so difficult to be kept constant when external parameters, such as input power, working pressure, are varied in the plasma processing. Thereby, optical emission spectroscopy (OES) technique is widely used as a monitoring tool in various plasma processes. Moreover, in order to compare those emission intensities with the concentration of species, it is necessary to assume that emissions from excited states chosen are proportional to the concentration of the same species in the ground state.

Therefore, the special technique such as actinometric optical emission spectroscopy (AOES) is frequently applied to estimate relative concentration of species in the ground state.^{22–28}

Optical emission spectra are generally measured by using a spectrometer. Usually, a monochromator with a photomultiplier tube (PMT) and multi-channel spectrometer with a charged coupled device (CCD) array are used. In a monochromator the light intensity is detected through the exit slit by PMT, as shown in Fig. 2.5(a). On the other hand, in a multi-channel spectrometer the light intensity is detected by each pixel of CCD, as shown in Fig. 2.5(b). The advantage of the multi-channel spectrometer is that it can measure a wide range (several ten nm) of wavelength simultaneously; however, the defect of the multi-channel spectrometer is that the resolution is restricted by the size of the pixel of CCD. The resolution of spectrometer sometimes limits the accuracy of measurements.

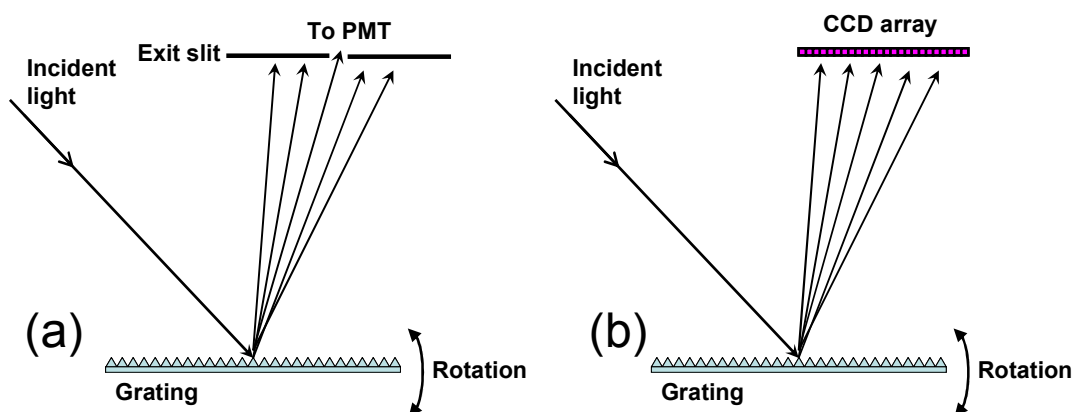


Fig. 2.5 The schematic illustration of (a) monochromator and (b) multi-channel spectrometer.

A spectral line measured by a spectrometer has a certain width. The full width at half maximum (FWHM) of the spectral line is determined by various factors such as natural broadening, Doppler broadening, pressure broadening, Stark broadening, and instrumental broadening (instrumental function). The natural broadening giving a Lorentzian line shape, however, is generally very small and negligible. Doppler broadening depends on the temperature of the species of interest. Doppler broadening gives a Gaussian line shape as,

$$f_D(\nu) = \exp \left[- \left\{ 2\sqrt{\ln 2} \frac{(\nu - \nu_0)}{\Delta\nu_D} \right\}^2 \right], \quad (2.23)$$

with

$$\Delta\nu_D = \frac{2\nu_0}{c} \sqrt{\frac{2RT \ln 2}{M}}, \quad (2.24)$$

where $\Delta\nu_D$ is the FWHM of the Doppler broadening, ν_0 is the center frequency, c is the velocity of light, R is the gas constant, T is the gas temperature, M is the mass number. Pressure broadening depends on pressure around the species of the interest gives a Lorentzian function as,

$$f_P(\nu) = \frac{\Delta\nu_P}{2 \left\{ 4(\nu - \nu_0)^2 + \left(\frac{\Delta\nu_P}{2} \right)^2 \right\}}, \quad (2.25)$$

with

$$\Delta\nu_P = \frac{1}{\pi} z = \frac{1}{\pi} n \sigma \sqrt{\frac{8RT}{\pi\mu}}, \quad (2.26)$$

where ν_P is the FWHM of the pressure broadening, z is the collision frequency, n is the concentration of the species, σ is the collision cross section, μ is the reduced mass. Stark broadening depends on the electric field caused by charged particles such as electrons and ions. The actual spectrum is determined from the convolution of the

Chapter 2

various broadening mechanisms. The convolution of Gaussian and Lorentzian functions results in a Voigt profile. Voigt function is given by,

$$f_V(\nu) = \frac{a}{\pi} \int \frac{\exp(-y^2)}{a^2 + (\omega + y)^2} dy, \quad (2.27)$$

with

$$a = \frac{\Delta \nu_L}{\Delta \nu_G} \sqrt{\ln 2}, \quad (2.28)$$

and

$$\omega = \frac{2(\nu - \nu_0) \sqrt{\ln 2}}{\Delta \nu_G}, \quad (2.29)$$

where $\Delta \nu_L$ is the FWHM of the Lorentz broadening, $\Delta \nu_G$ is the FWHM of the Gaussian broadening.

2.2.6 Microwave Interferometer

Microwave interferometer, the most common wave diagnostics technique, has been used to measure plasma density by propagation measurement. Spatial resolution inferior to probe measurement such as Langmuir probe, however, time response is faster and the propagation measurement does not disturb plasmas. The principle of its use is that change in phase shift across a region with and without plasma can be measured. This in turn can be related to the change in propagation constant and hence to the plasma frequency.

Since the propagation constant of a wave is dependent on the plasma frequency of electron is given by

$$\omega_{pe} = \sqrt{\frac{e^2 n_e}{\epsilon_0 m_e}}, \quad (2.30)$$

propagation measurement have been used to measure plasma density. Here, e , n_e , m_e , and ϵ_0 are charge of electron (1.6×10^{-19} C), electron density, mass of electron (9.1×10^{-31} kg), and permittivity (or dielectric function) of a plasma (8.854×10^{-12} F/m), respectively. The change in phase shift is given by

$$\Delta\phi = k_0 \int_0^l \left[1 - \frac{\omega_p^2(x)}{\omega^2} \right]^{1/2} dx - l, \quad (2.31)$$

where $k_0 = \omega/c$ is the free space propagation constant, and l is the wave propagates across a region of length. It is often possible to choose the diagnostics frequency sufficiently high compared to plasma frequency that square root can be expanded. The free space part of the phase shift the conveniently cancels leaving

$$\Delta\phi = k_0 \int_0^l \frac{\omega_p^2(x)}{\omega^2} dx = \frac{k_0 e^2}{2\epsilon_0 m \omega^2} \int_0^l n(x) dx, \quad (2.32)$$

In this approximation, we see that the line integral of the density can be directly measured in term of a phase shift.²⁹

2.3 Film characterization methods

2.3.1 Raman spectroscopy

C. V. Raman discovered Raman scattering or the Raman effects in liquids in 1928^{30,31}, and then G. Landsberg and L. Mandelstam found Raman scattering in crystals³². When light is scattered from an atom or molecule, most photons are elastically scattered, such that the scattered photons have the same energy (frequency) and wavelength as the incident photons, which is called Rayleigh scattering as shown in Fig. 2.6(a). However, a very small amount of the scattered light is scattered by an excitation, with the scattered photons having a different frequency from the incident photons, which effect is called Raman scattering. There are two types of Raman scattering; Stokes scattering and anti-Stokes scattering. In Stokes scattering, molecule absorbs energy, and photon of lower energy generates a Stokes line on the red side of the incident spectrum as shown in Fig. 2.6(b). On the other hand, in anti-Stokes scattering, a molecule loses energy, and incident photons are shifted to the blue side of the spectrum, thus generating an anti-Stokes line as shown in Fig. 2.6(c).

Raman spectroscopy employs the Raman effect for materials analysis. The frequency of light scattered from a molecule may be changed based on the structural characteristics of the molecular bonds. A monochromatic light source like laser is required for illumination. Because Raman spectroscopy is sensitive against silicon nanostructure as shown in Fig.2.7,³³ it has been powerfully used for analysis of a-Si:H and $\mu\text{c-Si:H}$. The Raman shift of crystalline structures of silicon is well known. The spectra of $\mu\text{c-Si:H}$ include three peaks corresponding to crystalline (520 cm^{-1}), defective crystalline (510 cm^{-1}), and amorphous (480 cm^{-1}) phases. In this study, the Raman spectra were decomposed into these peaks and the crystalline factor ϕ_c , was calculated as follows:³⁴

$$\phi_c = \frac{I_{520} + I_{510}}{I_{520} + I_{510} + I_{480}}, \quad (2.33)$$

where I_k is the area under the Gaussian curve centered at k , and k is the Raman shift.

During Raman spectroscopy measurement, laser light enters to the sample. The scattered light passes through a double monochromator to remove Rayleigh scattering. The light of Raman-shifted wavelength is detected by a photodetector. A commercial instrument of Raman spectroscopy usually consists of a laser illumination and microscope. Laser power is normally kept below 5 mW because high power injection would cause the sample heating and specimen decomposition. Ar⁺ laser is widely used as a light source, whose wavelengths are 514.5, 488.0, and 457.9 nm. In this study, 514.5 nm laser was used as the excitation source (Renishaw inVia ReflexStreamline).

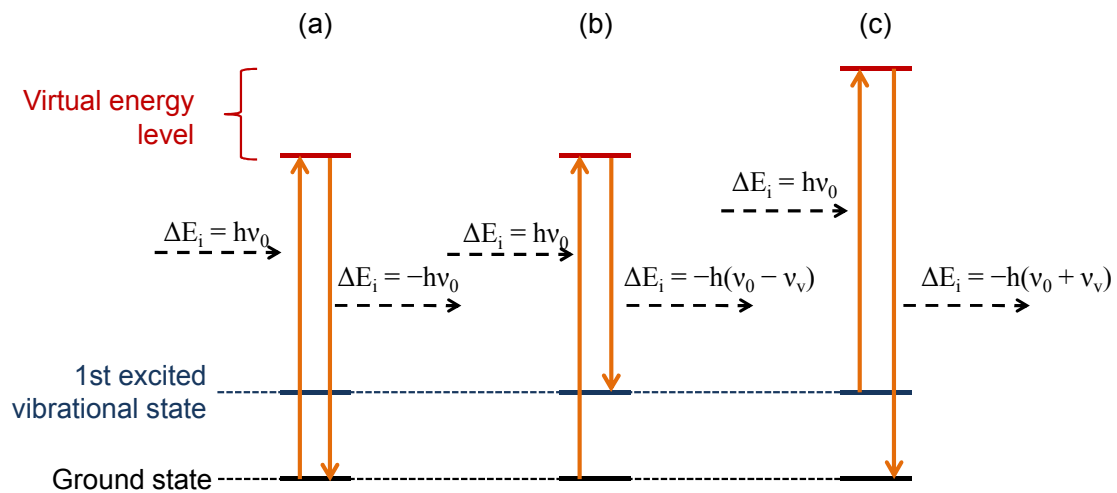


Fig. 2.6 The different possibilities of light scattering. (a) Rayleigh scattering, (b) Stokes scattering, and (c) anti-Stokes scattering.

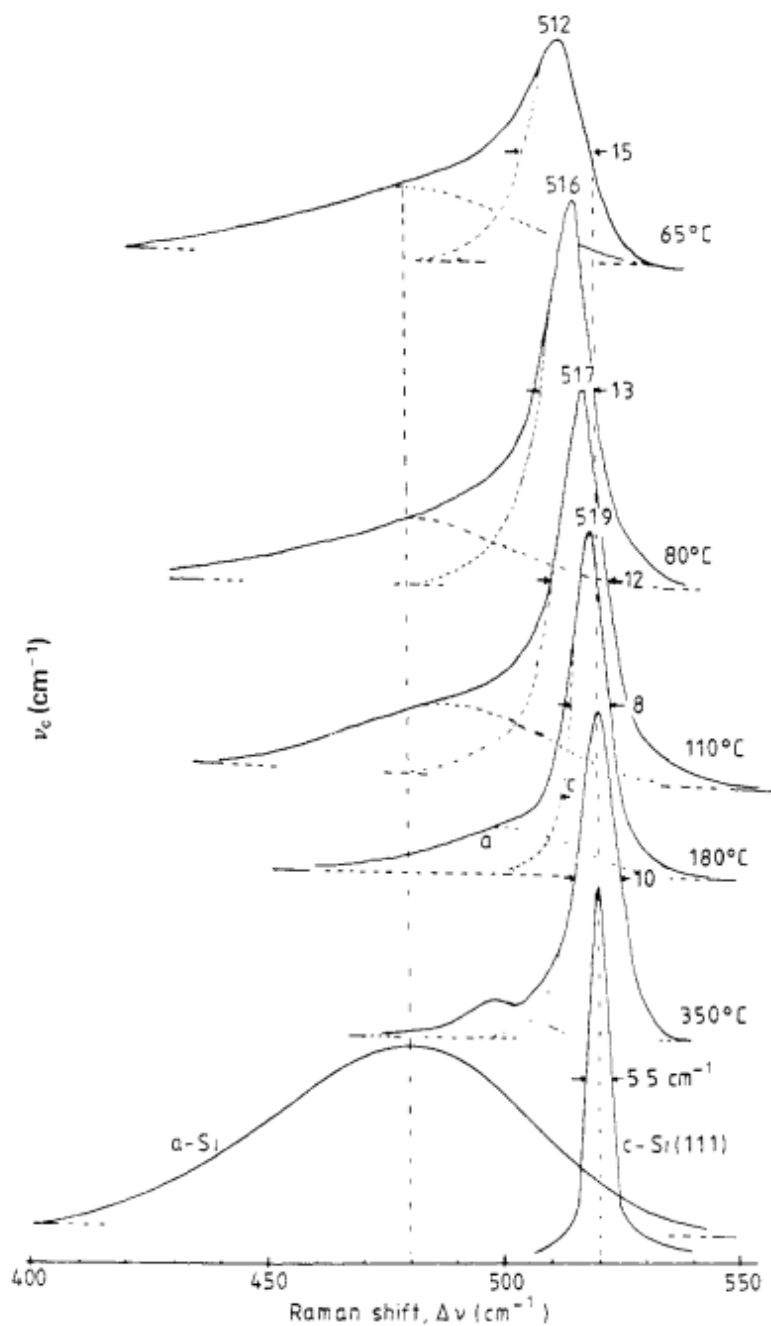


Fig. 2.7 Raman spectra of microcrystalline silicon films deposited at various temperatures between 65 and 350°C. The sample at 180°C was deposited on a single-crystal Si (111) wafer and the others on amorphous metals and quartz. The Raman spectra of single-crystal (c-Si(111)) and amorphous silicon are also shown for comparison.³³

2.3.2 X-Ray diffraction (XRD)³⁵

X-ray diffraction (XRD) is a non-destructive technique for identifying a crystal structure such as crystalline phases, orientation and grain size. It requires little sample preparation and gives structure information over entire materials. Consider a perfect crystal arranged to diffract monochromatic X-rays of wavelength λ from lattice planes spaced d . The X-rays are incident on the sample and reflected at an angle θ , as shown in Fig. 2.8. The X-rays scattered from adjacent planes will combine constructively when the θ results in a path-length difference that is an integer multiple n of λ as below equation, which is the Bragg's law.

$$2d \sin \theta = n\lambda \quad (2.34)$$

In the case of silicon, the observed diffraction peaks are predominately (111), (220), and (311). XRD analysis in the θ - 2θ scan geometry using the CuK α line (Rigaku SmartLab) was employed. Table 2.1 shows the lattice spacing, the diffraction angle and intensity ratio of each lattice planes.

The grain size can be estimated from the width of a diffraction peak, via Scherrer's equation:

$$D_{hkl} = \frac{k\lambda}{\beta \cos \theta}, \quad (2.35)$$

where D_{hkl} is grain size of (hkl) lattice plane, β is width of a diffraction peak, and k is constant which is 0.9 (width is full-width at half-maximum) or 1 (width is integral width).

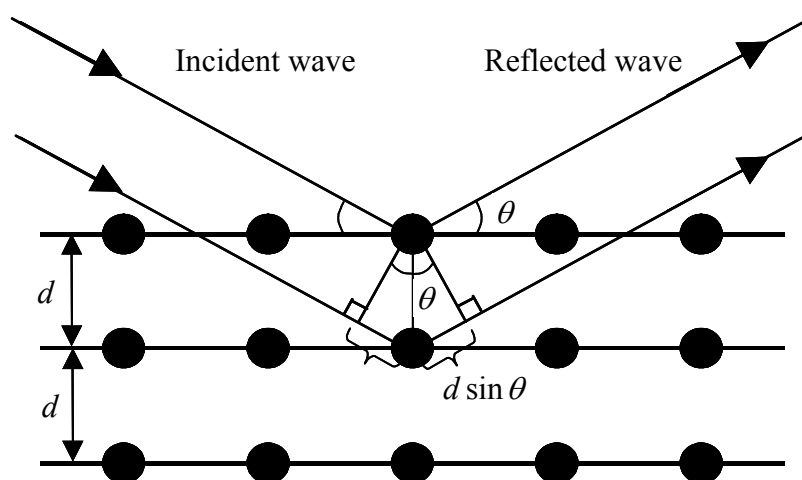


Fig. 2.8 Schematic illustration of the Bragg's law.

Table. 2.1 Lattice spacing, the diffraction angle and intensity ratio of silicon.

Diffraction plane	Lattice spacing (\AA)	Diffraction angle 2θ (degree)	Intensity ratio (%)
(111)	3.138	28.4	100
(220)	1.920	47.3	67.0
(311)	1.638	56.1	39.9

2.3.3 Fourier transform infrared spectroscopy (FTIR)

Fourier Transform Infrared Spectroscopy (FTIR) allows us to detect infrared (IR) absorption and reflection properties of materials.³⁶⁻³⁸ FTIR is widely used to evaluate for a chemical bonding such as C–H, C–F, C–N, C–O, Si–H, Si–O–Si,³⁹⁻⁴³ and so on. The foundations of FTIR were laid in the latter part of the nineteenth century by Michelson,⁴⁴ Raleigh,⁴⁵ Rubens and Wood,⁴⁶ von Baeyer,⁴⁷ and others who recognized the relationship of an interferogram to its spectrum by a Fourier transformation. It was not until the advent of computers and the fast Fourier algorithm that interferometry began to be applied to spectroscopic measurements in the 1970s. FTIR is based on a Michelson interferometer, which consists of a beam splitter, a fixed mirror and a moving mirror (scanning mirror).⁴⁸ Light from the source (see Fig. 2.9) is separated into two parts and then recombines at the beam splitter after reflection by the two mirrors as shown in Fig. 2.10. The transmission factor and the reflection coefficient of beam splitter are T_0 and R_0 , respectively. Light I_0 (wave number ν) from the infrared source is collimated and directed onto a beam splitter. The light intensity reaching the detector is the sum of the two beams. In the case of $L_1 = L_2$ (L_1 : distance between beam splitter and fixed mirror M_1 , L_2 : distance between beam splitter and fixed mirror M_2), the light intensity of $2I_0T_0R_0$, enters the detector. When M_1 is moved, the optical path lengths are unequal and an optical path difference δ is introduced. If M_1 is moved a distance, the retardation is $\delta = 2x$ since the light has to travel an additional distance x to reach the mirror and the same distance to reach the beam splitter. The light intensity $I_{\text{obs}}(x)$ reaching the detector depends on the value of x that can be described by the equation

$$I_{\text{obs}}(x) = 2R_0T_0I_0[1 + \cos(2\pi\nu x)]. \quad (2.36)$$

when $R_0, T_0 = 0.5$, Eq. (2.36) is

$$I_{\text{obs}}(x) = \frac{I_0}{2}[1 + \cos(2\pi\nu x)]. \quad (2.37)$$

Consider the light have the wave number ν_1 – ν_2 and the intensity $I_0(\nu)$. When the source emits more than one frequency, Eq. (2.37) is replaced by the integration

$$I_{\text{obs}}(x) = \int_{\nu_1}^{\nu_2} \frac{I_0(\nu)}{2} [1 + \cos(2\pi\nu x)] d\nu. \quad (2.38)$$

Direct current from the interference output signal of Eq. (2.38) is subtracted.

$$F(x) = \frac{1}{2} \int_{\nu_1}^{\nu_2} I_0(\nu) \cos(2\pi\nu x) d\nu. \quad (2.39)$$

Due to the path difference between the two beams, an interference pattern is generated. The output beam from interferometer is recorded as a function of path difference, and is called the interferogram (see Fig. 2.8). When Eq. (2.39) is generalize

$$F(x) = \int_{-\infty}^{\infty} I_0(\nu) \exp(2\pi\nu i) d\nu. \quad (2.40)$$

The incident radiation $I_0(\nu)$ is obtained by the Fourier transform of the interferogram actually measured.

$$F(x) = \frac{1}{2} \int_{-\infty}^{\infty} F(\nu) \exp(2\pi\nu i) dx. \quad (2.41)$$

The IR spectrum can be obtained by calculating the Fourier transform of the interferogram.

There are two primary advantages to using FTIR as compared to a dispersive spectrometer, Fellgett's advantage (Multiplex advantage) and Jacquinot's advantage (Throughput advantage). Generally, the signal-to-noise ratio (SNR) is proportional to the number of scans or measurement time T ($\text{SNR} \propto \sqrt{T}$). In a broadband spectrum, the number of spectral elements n between the frequency range ν_1 and ν_2 can be defined as $n = (\nu_2 - \nu_1) / \Delta\nu$. In a dispersive spectrometer, a particular spectral element is recorded in a time t , so that the total time required is $T = nt$. However, the FTIR spectrometer records information for all wavelengths in the spectrum simultaneously. During each scan, it records n times faster than a dispersive spectrometer with the same SNR. If the

Chapter 2

measurement time is the same, then the SNR will be increased by factor of \sqrt{n} . In a dispersive spectrometer the energy throughput is limited by the entrance and exit slits of the monochromator. Since the FTIR does not require slits, measurements at higher intensities are possible. To increase the resolution of a dispersive spectrometer, the slits must be narrowed. In an FTIR, the resolution is increased by increasing the mirror travel distance with no decrease in the energy throughput. In this study, IR absorption spectra were measured by FTIR spectrometer (Thermo Scientific, Nicolet-8700).

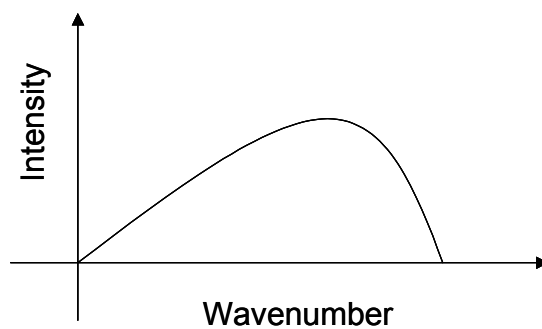


Fig. 2.9 Spectrum of light source.

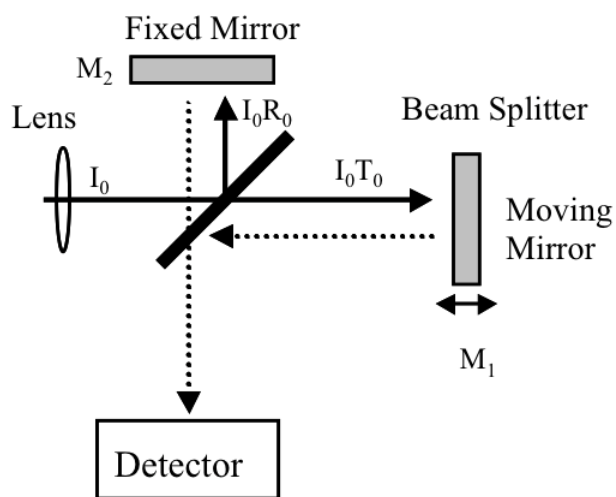


Fig. 2.10 Schematic diagram of FTIR.

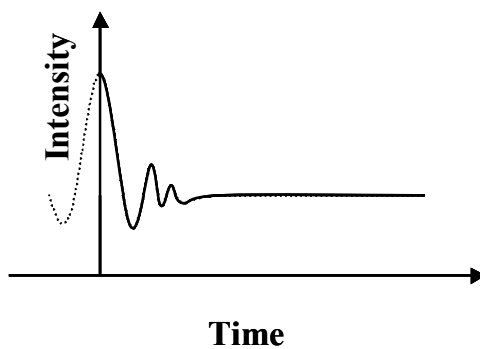


Fig. 2.11 Interferogram.

2.3.4 Electron spin resonance (ESR)^{49,50}

ESR is a technique to measure unpaired electrons which occupies molecular or atomic orbital singly in materials. Generally, two electrons occupy the same orbital, however unpaired electrons exist in some cases: d orbital of transition metal, f orbital of lanthanides, radicals and dangling bonds caused by a lattice defect of materials. The ESR enables us to study the density and the environment of unpaired electrons.

In the presence of an external magnetic field, the magnetic energy of the magnet depends on the direction of a magnetic moment. The potential energy of the magnet U is given by inner product of the magnetic moment $\boldsymbol{\mu}$ and the magnetic field \mathbf{H} and is represented by

$$U = -\boldsymbol{\mu} \cdot \mathbf{H} = \mu H \cos \theta. \quad (2.42)$$

Electron has the magnetic moment $\boldsymbol{\mu}_e$ and the magnitude is given by

$$|\boldsymbol{\mu}_e| = \frac{eh}{4\pi m} \equiv \mu_B, \quad (2.43)$$

where μ_B is the Bohr magneton, e is the elementary charge, h is the Planck constant and m is the electron mass. The energy is quantized and discrete because $\boldsymbol{\mu}_e$ is quite small. The energy of the magnetic moment $\boldsymbol{\mu}_e$ is

$$U = \mu_B H (2m_s), \quad (2.44)$$

where m_s is the magnetic quantum number and the values are $-1/2$ (parallel to the magnetic field) or $1/2$ (antiparallel to the magnetic field). Figure 2.12 shows U as a function of H with energy levels for $m_s = \pm 1/2$. The separation of energy in the presence of the magnetic field is called the Zeeman effect. Generally, a number of electrons exist in lower energy level ($m_s = -1/2$). Here, the electromagnetic wave of the appropriate frequency ν causes a transition from lower energy level to higher energy level when the energy of electromagnetic wave $h\nu$ is equal to the difference of lower and higher energy levels. This phenomenon is called electron spin resonance. The resonance condition is

represented by

$$h\nu = 2\mu_B H_0 \quad (2.45)$$

Electrons responds not only to the applied magnetic field but also to any local magnetic fields of atoms or molecules, therefore instead of the constant 2 in the right hand of Eq. (2.45) g -factor is used.

$$h\nu = g \mu_B H_0 \quad (2.46)$$

The Eq. (2.46) is called the resonance condition of ESR. In the case of general ESR equipment, the absorption of a microwave by electron is measured with keeping the ν of the microwave and satisfying the resonance condition by changing the applied magnetic field. ESR spectra are recorded as first derivatives as shown in Fig. 2.13. In this study, ESR measurements were conducted using a standard X-band (9 GHz) spectrometer (Bruker Biospin, EMX plus) with a microwave resonator (Bruker Biospin, ER4119HS-W1).

The absorption intensity of ESR (ESR signal) is proportional to the density of unpaired electrons in samples. The unpaired electron density of an objective sample N_x can be calibrated using a standard sample of which the unpaired electron density is known and following equation.

$$N_x = \frac{Q_x}{Q_{cal.}} \frac{I_x}{I_{cal.}} N_{cal.} \quad (2.47)$$

$N_{cal.}$ and $I_{cal.}$ are the unpaired electron density and the intensity of ESR signal of the standard sample, respectively. I_x is the intensity of ESR signal of the objective sample. Q_x and $Q_{cal.}$ are correction values which depend on the kind of samples and measurement condition. In this study, $\text{CuSO}_4 \cdot 5\text{H}_2\text{O}$ was used as the standard sample.

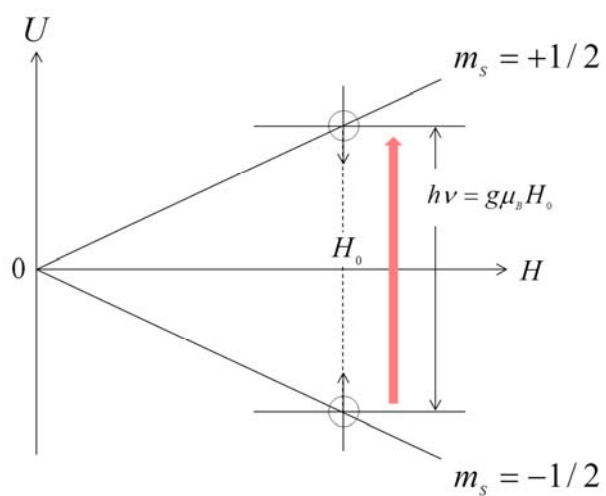


Fig. 2.12 Energy of the magnetic moment as a function of the magnetic field.

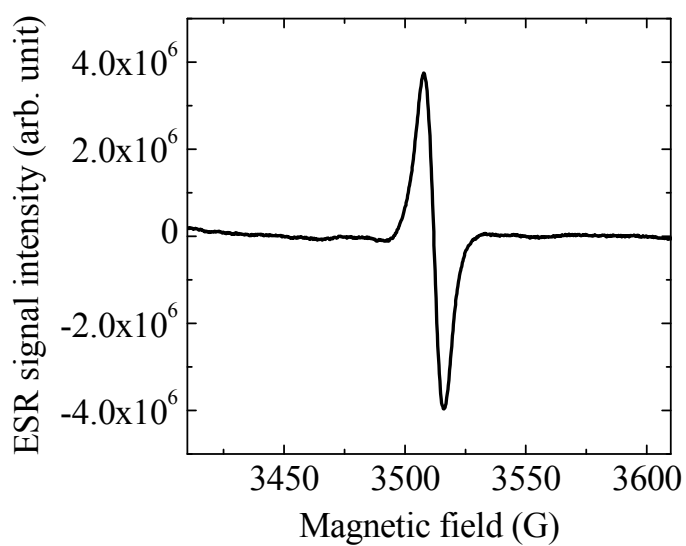


Fig. 2.13 ESR spectrum of $\mu\text{c-Si:H}$ thin film.

2.3.5 Transmission electron microscopy (TEM)

Transmission electron microscopy (TEM) is a microscopy technique whereby a beam of electrons is transmitted through an ultra thin specimen, interacting with the specimen as it passes through. TEM has been widely used for highly magnified sample images.⁴⁸ TEM is capable of imaging at a significantly higher resolution than light microscopes, owing to the small de Broglie wavelength of electrons. This enables the instrument's user to examine fine detail—even as small as a single column of atoms, which is tens of thousands times smaller than the smallest resolvable object in a light microscope. TEM forms a major analysis method in a range of scientific fields, in both physical and biological sciences. At present, extremely high resolution has been obtained in TEM to be 0.05 nm, contributing advances in aberration corrector design have been able to reduce spherical aberrations.^{51,52}

The TEM is, in principle, similar to optical microscope; both contain a series of lenses to magnify the sample. A schematic of a TEM is shown in Fig. 2.14. Electrons from an electron gun are accelerated to high voltage— typically 100 to 400 kV— and focused on the sample by the condenser lenses. The transmission ability to the sample increases with increasing the energy of the electron, and resolution also improves, because the de Broglie wave λ of the electron beam shorten by the high acceleration voltage as

$$\lambda = \frac{h}{\sqrt{2meV\left(1 + \frac{eV}{2mc^2}\right)}} = \frac{0.03878}{\sqrt{V(1 + 9.785 \times 10^{-4}V)}} (nm), \quad (2.48)$$

where h is Planck's constant, m and e are the mass of electrons and the charge of electron, respectively, V is the acceleration voltage (kV), and c is the velocity of light. The sample in the size of a few mm in diameter is placed on a small copper grid. The electron beam has a diameter of few microns. The sample must be sufficiently thin (a few

Chapter 2

tens to a few hundred nm) to be transparent to electrons. The transmitted and forward scattered electrons form a diffraction pattern in the back focal plane and a magnified image in the image plane. With additional lenses, either the image or the diffraction pattern is projected onto a fluorescent screen for viewing as well as electronic or photographic recording. The ability to form a diffraction pattern yields structural information.

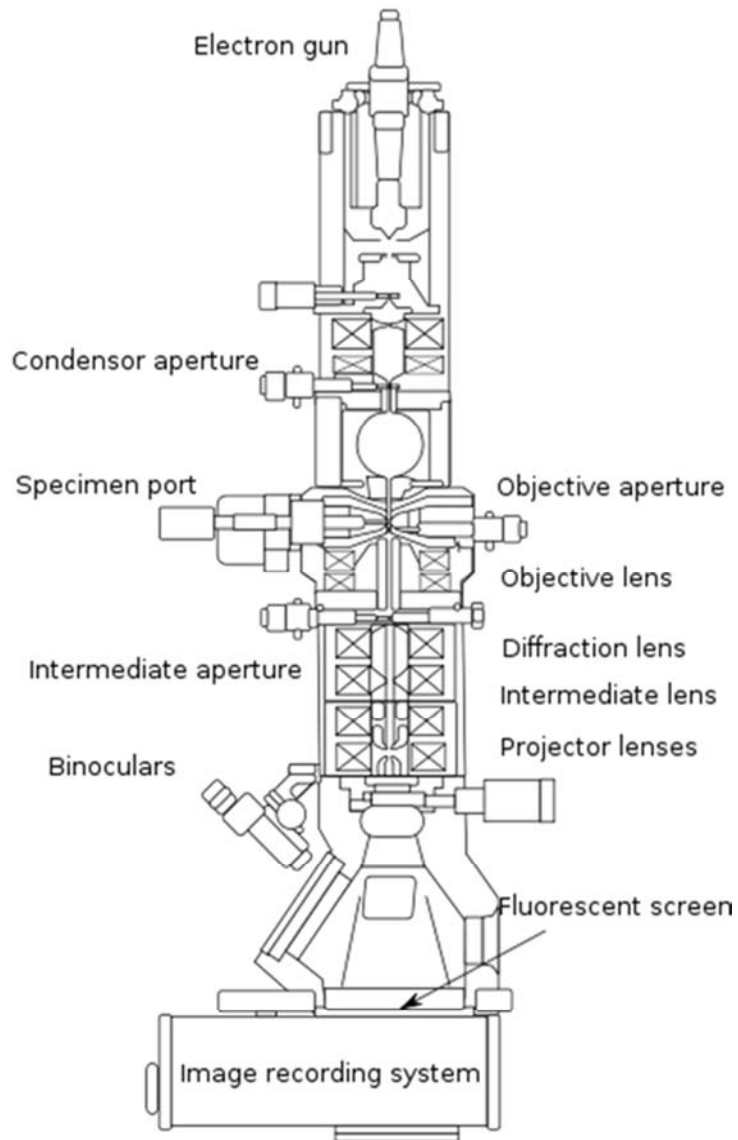


Fig. 2.14 Schematic of a TEM.

2.4 References

- ¹ A. C. G. Mitchell and M. W. Zemansky, *RESONANCE RADIATION AND EXCITED ATOMS* (Cambridge, London, 1961).
- ² S. Takashima, M. Hori, T. Goto, A. Kono, M. Ito, and K. Yoneda, *Appl. Phys. Lett.* **75**, 3929 (1999).
- ³ S. Takashima, S. Arai, M. Hori, T. Goto, A. Kono, M. Ito, and K. Yoneda, *J. Vac. Sci. Technol. A* **19**, 599 (2001).
- ⁴ H. Nagai, M. Hiramatsu, M. Hori, and T. Goto, *Rev. Sci. Instrum.* **74**, 3453 (2003).
- ⁵ R. S. Freund, *J. Chem. Phys.* **64**, 1122 (1976).
- ⁶ K. Ito, N. Oda, Y. Hatano, and T. Tsuboi, *Chem. Phys.* **21**, 203 (1977).
- ⁷ S. Djurović and J.R. Roberts, *J. Appl. Phys.* **74**, 6558 (1993).
- ⁸ G. New and J. Ward, *Phys. Rev. Lett.* **19**, 556 (1967).
- ⁹ J. Ward and G. New, *Phys. Rev.* **185**, 57 (1969).
- ¹⁰ S. E. Harris, *Appl. Phys. Lett.* **19**, 385 (1971).
- ¹¹ R. Miles and S. Harris, *IEEE J. Quantum Electron.* **9**, 470 (1973).
- ¹² A. Kung, J. Young, G. Bjorklund, and S. Harris, *Phys. Rev. Lett.* **29**, 985 (1972).
- ¹³ G. Hilber, A. Lago, and R. Wallenstein, *J. Opt. Soc. Am. B* **4**, 1753 (1987).
- ¹⁴ K. Tachibana and H. Kamisugi, *Appl. Phys. Lett.* **74**, 2390 (1999).
- ¹⁵ K. W. Busch and M. A. Busch, editors, *Cavity-Ringdown Spectroscopy* (American Chemical Society, Washington, DC, 1999).
- ¹⁶ A. Campargue, D. Romanini, and N. Sadeghi, *J. Phys. D: Appl. Phys.* **31**, 1168–1175 (1998).
- ¹⁷ E. Quandt, I. Kraemer, and H.F. Döbele, *Europhys. Lett.* **45**, 32 (1999).
- ¹⁸ R. Engeln, K. G. Y. Letourneur, M. G. H. Boogaarts, M. C. M. van de Sanden, and D. C. Schram, *Chem. Phys. Lett.* **310**, 405 (1999).

- ¹⁹ F. Grangeon, C. Monard, J. L. Dorier, A. A. Howling, C. Hollenstein, D. Romanini, and N. Sadeghi, *Plasma Sources Sci. Technol.* **8**, 448 (1999).
- ²⁰ J. P. Booth, G. Cunge, L. Biennier, D. Romanini, and A. Kachanov, *Chem. Phys. Lett.* **317**, 631 (2000).
- ²¹ A. O'Keefe and D. A. G. Deacon, *Rev. Sci. Instrum.* **59**, 2544 (1988).
- ²² J. W. Coburn and M. Chen, *J. Appl. Phys.* **51**, 3134 (1980).
- ²³ Y. Kawai, K. Sasaki, and K. Kadota, *Jpn. J. Appl. Phys.* **36**, L1261 (1997).
- ²⁴ R. E. Walkup, K. L. Saenger, and G. S. Selwyn, *J. Chem. Phys.* **84**, 2668 (1986).
- ²⁵ H. M. Katsch, A. Tewes, E. Quandt, A. Goehlich, T. Kawetzki, and H. F. Döbele, *J. Appl. Phys.* **88**, 6232 (2000).
- ²⁶ S. F. Durrant, *J. Vac. Sci. Technol. A* **13**, 2513 (1995).
- ²⁷ S. F. Durrant, *J. Vac. Sci. Technol. A* **16**, 509 (1998).
- ²⁸ A. Gicquel, M. Chenevier, K. Hassouni, A. Tserepi, and M. Dubus, *J. Appl. Phys.* **83**, 7504 (1998).
- ²⁹ M. A. Lieberman and A. J. Lichtenberg, *Principles of Plasma Discharges and Materials Processing*, Second edition (John Wiley & Sons, Inc., New York, 2005).
- ³⁰ C. V. Raman and K.S. Krishnan, *Nature* **121**, 501 (1928).
- ³¹ R. Singh, *Physics in Perspective* **4**, 399 (2002).
- ³² G. Landsberg and L. Mandelstam, *Die Naturwissenschaften* **16**, 557–558 (1928).
- ³³ Z. Iqbal and S. Veprek, *J. Phys. C: Sol. Stat. Phys.* **15**, 377 (2000).
- ³⁴ C. Droz, E. Vallat-Sauvain, J. Bailat, L. Feitknecht, J. Meier, and A. Shah, *Sol. Energy Mater. Sol. Cells* **81**, 61 (2004).
- ³⁵ B. Cullity, *Elements of X-ray Diffraction* (ADDISON-WESLEY, Reading, MA, 1956).
- ³⁶ P. R. Griffiths and J. A. de Haseth, *Fourier Transform Infrared Spectrometry* (Wiley, New York, 1986).
- ³⁷ M. Nitschke and J. Meichsner, *J. Appl. Polym. Sci.* **65**, 381 (1997).

- ³⁸ M. Tasumi, *FT-IR No Kiso to Jissai, [Basic and Actually of FT-IR]* (TOKYO KAGAKU DOZIN, Tokyo, 1998).
- ³⁹ Y. Gotoh and S. Kajiura, *J. Nucl. Mater.* **266-269**, 1051 (1999).
- ⁴⁰ J. Zhang, D. P. Wilkinson, H. Wang, and Z. S. Liu, *Electrochimica Acta* **50**, 4082 (2005).
- ⁴¹ J. Wei, *J. Appl. Phys.* **92**, 6525 (2002).
- ⁴² X. LI, K. HUANG, S. LIU, N. TAN, and L. CHEN, *T. Nonferr. Met. Soc. China* **17**, 195 (2007).
- ⁴³ A. Grill, V. Patel, K. P. Rodbell, E. Huang, M. R. Baklanov, K. P. Mogilnikov, M. Toney, and H. C. Kim, *J. Appl. Phys.* **94**, 3427 (2003).
- ⁴⁴ A. A. Michelson, *Phil. Mag. Series 5* **31**, 256 (1891).
- ⁴⁵ Lord Rayleigh, *Phil. Mag. Series 5* **34**, 407 (1892).
- ⁴⁶ H. Rubens and R. W. Wood, *Phil. Mag. Series 6* **21**, 249 (1911).
- ⁴⁷ H. Rubens and O. von Baeyer, *Phil. Mag. Series 6* **21**, 689 (1911).
- ⁴⁸ D. K. Schroder, *Semiconductor Materials and Device Characterization Third Edition* (Wiley, New York, 2006).
- ⁴⁹ N. M. Atherton, *Principles of Electron Spin Resonance* (Ellis Horwood, New York, 1993).
- ⁵⁰ J. Yamauchi, *Jikikyome-ESR, [Magnetic resonance-ESR]* (Saiensu-sha, Tokyo, 2006).
- ⁵¹ R. Erni, M. Rossell, C. Kisielowski, and U. Dahmen, *Phys. Rev. Lett.* **102**, 096101 (2009).
- ⁵² N. Tanaka, *Sci. Technol. Adv. Mater.* **9**, 014111 (2008).

Chapter 3 Investigation of Surface Loss Probability of H Radicals in SiH₄/H₂ Plasma

3.1 Introduction

Hydrogen (H) based plasmas are widely used in the deposition processes of various thin films, such as diamond-like hydrocarbon, hydrogenated amorphous silicon (a-Si:H) and hydrogenated microcrystalline silicon ($\mu\text{c-Si:H}$). Thin film silicon solar cells, in which the semiconductor layers are composed of a-Si:H or $\mu\text{c-Si:H}$ thin films deposited by plasma enhanced chemical vapor deposition (PECVD), are a promising technology for realizing low cost photovoltaics. H radicals are known to influence the properties of silicon (Si) thin films, and a sufficient supply of H radicals to the deposition surface is necessary for the crystallization of Si thin films.¹ Surface coverage,² etching reactions,³⁻⁵ and modification of the Si-Si network⁶ have been proposed as roles of H radicals on the surface during deposition. Therefore, understanding the behavior of H radicals in plasmas is critically important for the development of deposition processes. In addition, it is essential to realize a highly reliable process, because the process margin to obtain high quality $\mu\text{c-Si:H}$ thin films for solar cells is very narrow.⁷

The absolute densities of species in plasmas are affected by the surface conditions of the chamber wall, electrodes, and the substrate. One reason for this is the dependence of the surface loss probability of the species on the surface conditions.^{8,9} Estimation of the surface loss probability is important for controlling the density of species and for clarifying surface reactions. There have been a number of reports on surface loss probabilities for species including molecular radicals¹⁰⁻¹⁵ and atomic radicals¹⁶⁻¹⁹ using various diagnostic techniques, such as absorption spectroscopy and appearance mass spectroscopy. The surface loss probabilities of H radicals have also

Chapter 3

been investigated under various conditions,^{8,15,20–24} however, the surface loss probability of H radicals in SiH₄/H₂ plasma has, to our knowledge, been reported only once.²⁵

In this study, the surface loss probabilities of H radicals on Si thin films were estimated by measuring the decay time constants of H radicals in a SiH₄/H₂ mixture plasma afterglow. The decay time constants were measured using vacuum ultraviolet resonance absorption spectroscopy (VUVAS). The surface loss probabilities obtained in this study will facilitate the precise control for deposition processes of a-Si:H and μ c-Si:H thin films, and contribute to understanding the surface reactions that occur during deposition.

3.2 Experimental details

Figure 3.1 shows a schematic diagram of the experimental setup used to measure the absolute density of H radicals. The process chamber dimensions were $\varnothing 80 \times 170$ mm. An input power of 320 or 350 W with 13.56 MHz radio frequency (rf) was supplied to the inner antenna, which was coated with Al_2O_3 to prevent contamination and cooled by water. Pulsed rf power with a repetition frequency of 10 Hz (25 ms on, 75 ms off) was applied to generate the plasma to measure the decay of the H radical density in the plasma afterglow. The pressure was varied from 22 to 40 Pa. A microdischarge hollow cathode lamp (MHCL) was used as a VUV light source. The process chamber and VUVAS system were differentially pumped using two capillary plates; VUV transparent windows were located at the each end of each port for the VUV monochromator and MHCL. The absorption path length was 220 mm between capillary plates. In absolute density measurements using resonance lamp as a light source, the H_2 -MHCL, of which was known the emission-line profile, was used for an accurate measurement of H radical density.²⁶ The transition lines employed for measurement of the absolute radical densities were the Lyman α at 121.6 nm for absorption by H radicals. For measuring a background absorption, the N_2 -MHCL was used and the transition lines were $^4\text{P}_{5/2} - ^4\text{S}^{\circ}_{3/2}$, $^4\text{P}_{3/2} - ^4\text{S}^{\circ}_{3/2}$, and $^4\text{P}_{1/2} - ^4\text{S}^{\circ}_{3/2}$ at 120.0 nm of N atom.²⁷ The background absorption seems to be caused by SiH_4 molecules and higher radicals. Percentage of absorption observed under the conditions studied was from 9.0 to 55.0%, and that of background absorption was from 0 to 25.4%.

The temperature of the chamber wall that is made of stainless steel was controlled using a refrigerated and heating circulator and was monitored with a thermocouple. Si thin films deposited on the chamber wall were analyzed using a step profiler and Raman spectroscopy to investigate the relation between the surface loss probability and the surface condition of the chamber wall.

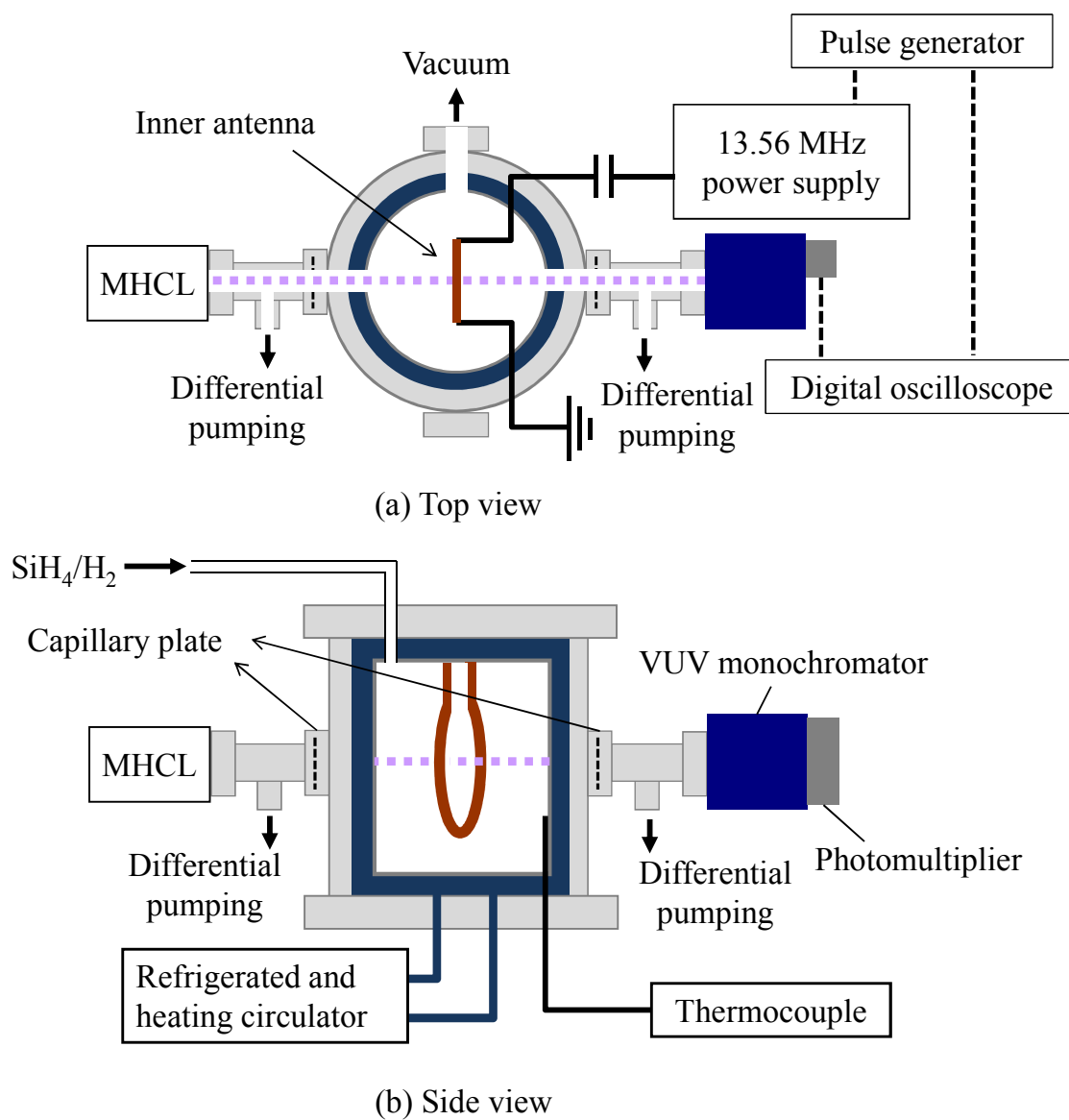
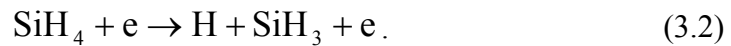


Fig. 3.1 Schematic diagram of the experimental apparatus used to measure the surface loss probability of H radicals in plasma afterglow employing a VUVAS system.

3.3 Results

3.3.1 Surface loss kinetics of H radicals in the afterglow of SiH₄/H₂ plasma

To clarify the loss kinetics of H radicals in the SiH₄/H₂ plasma, the H radical densities in the plasma afterglow were investigated. Before presenting the measured surface loss probabilities, the generation and loss mechanisms in the plasma should be discussed. The primary reaction in the plasma is caused by collisions between fast electrons and feed gases selected depending on the processes. The decomposition products consist of positive and negative ionic species and neutral species such as molecular species and neutral radicals. H radicals are produced by electron impact dissociation of H₂ and SiH₄:



On the other hand, the removal processes of H radicals are due to removal by pumping action, gas-phase recombination, and diffusion followed by the recombination at chamber walls. Accordingly, the behavior of the H radical density can be described by the following rate equation:

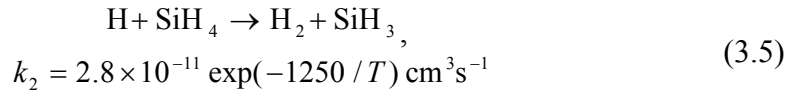
$$\begin{aligned} \frac{dN(\text{H})}{dt} = & \langle \sigma_{\text{H}_2} v_e \rangle n_e N(\text{H}_2) + \langle \sigma_{\text{SiH}_4} v_e \rangle n_e N(\text{SiH}_4) \\ & - \frac{N(\text{H})}{\tau_{\text{pump}}} - \frac{N(\text{H})}{\tau_d} - k_1 N^2(\text{H}) N(x) - k_2 N(\text{H}) N(\text{SiH}_4) \end{aligned} \quad (3.3)$$

where $N(\text{H})$, $N(\text{H}_2)$, $N(\text{SiH}_4)$ and $N(x)$ represent the H radical density, the H₂ density, the SiH₄ density and the density of other species x reacting with the H radicals, respectively, σ_{H_2} and σ_{SiH_4} are the generation cross-section of H radicals by one electron impact on H₂ and SiH₄, v_e is the thermal velocity of the electron, n_e is the electron density, τ_{pump} is the loss time by pump action, τ_d is the diffusion lifetime of H

radicals and k_x are the reaction rate constants between H radicals and the reaction species.

In the first case of removal by pumping, the residence time under the conditions employed was estimated to be 200 ms, which was sufficiently longer than the observed decay times (0.4–2.0 ms). Therefore, the pumping action is considered to be negligible as a possible loss mechanism.

For the second type of loss, the relevant gas-phase reactions were taken into consideration^{28,29}



The reaction constant of (3.4) is too small to account for the observed decay times; therefore, the loss of H radicals by three body recombination is considered to be negligible. In contrast, the reaction constant of (3.5) is relatively high and the loss of H radicals by reaction with SiH₄ should be considered as feasible.

H radicals that do not react with SiH₄ in the gas phase reach the chamber wall where subsequent reactions occur on the surface. These could include surface reactions such as physical adsorption and desorption, chemical adsorption and desorption, reactions of chemisorbed radicals, and the surface diffusion of physisorbed radicals.

Considering the loss mechanisms, the extinction of H radicals in the afterglow is given by:

$$\frac{dN(\text{H})}{dt} = -\frac{N(\text{H})}{\tau_d} - k_1 N^2(\text{H})N(x) - k_2 N(\text{H})N(\text{SiH}_4). \quad (3.6)$$

Solving this rate equation while neglecting the $k_1 N^2(\text{H})N(x)$ term gives a single exponential function for the decay of the radical concentration in the afterglow plasma:

$$N(\text{H}) = N_0(\text{H}) \exp[-(1/\tau_d + k_2 N(\text{SiH}_4))t], \quad (3.7)$$

where $N_0(\text{H})$ is the initial H radical density. The measured decay time constant τ_m , corresponds to losses by diffusion followed by reactions on the wall surface and reaction with SiH_4 :

$$\tau_m = \frac{1}{1/\tau_d + k_2 N(\text{SiH}_4)}. \quad (3.8)$$

From Eq. (3.8) the effective diffusion lifetime taking into account the surface loss probability according to the model of Chantry³⁰ is represented by:

$$\tau_d = \frac{1}{1/\tau_m - k_2 N(\text{SiH}_4)}. \quad (3.9)$$

Therefore, τ_d is calculated using τ_m , the reaction rate constant k_2 ($2.8 \times 10^{-11} \exp(-1250/T)$)²⁹ and the density of SiH_4 . The density of SiH_4 is estimated from the pressure and the gas mixture ratio of SiH_4 and H_2 . The dissociation ratio of SiH_4 in the plasma afterglow is not significantly influence on results shown here, because the term of $1/\tau_m$ is one or two orders higher in magnitude compared with the term of $k_2 N(\text{SiH}_4)$.

The diffusion lifetime τ_d is represented by

$$\tau_d = \frac{pA^2}{D}, \quad (3.10)$$

where p is pressure, A is an effective diffusion length, and D is the diffusion coefficient for H radicals. A simple approximation of A^2 was proposed by Chantry³⁰

$$A^2 = A_0^2 + l_0 \lambda, \quad (3.11)$$

where A_0 and l_0 are the geometric diffusion length and the volume to area ratio of the chamber, and λ is determined by a surface boundary condition and expressed by

$$\lambda = \frac{4D}{v} \left(\frac{1 - \alpha/2}{\alpha} \right), \quad (3.12)$$

where v is the velocity of H radicals given by $(8kT/\pi M)^{1/2}$ [T and M are the temperature and mass, respectively, and k is the Boltzmann constant], and α is the surface loss probability on the chamber wall. For a cylinder of radius R and height H , A_0 and l_0 are given by

$$\frac{1}{A_0^2} = \left(\frac{\pi}{H} \right) + \left(\frac{2.405}{R} \right)^2, \quad (3.13)$$

$$l_0 = \frac{RH}{2(R+H)}. \quad (3.14)$$

These expressions of A^2 are actually rigorous in two limiting cases: (i) high pressure and/or $\alpha \rightarrow 1$ where $A^2 = A_0^2$, and (ii) low pressure and/or $\alpha \rightarrow 0$ where $A^2 \approx l_0 4D/\nu\alpha$, and accounts for intermediate cases within a 10% error. From Eqs. (3.10), (3.11), and (3.12), τ_d is represented by the following equation

$$\tau_d = \frac{pA_0^2}{D} + \frac{2l_0(2-\alpha)}{\nu\alpha}. \quad (3.15)$$

Prior to experiments of the SiH₄/H₂ plasma, the surface loss probability of H radicals for the stainless steel covered with no Si film in a pure H₂ plasma was estimated. Figure 3.2 shows a typical decay curve of the H radical density on the stainless steel wall in the H₂ plasma afterglow at the RF power of 320 W, H₂ flow rate of 50 sccm and the pressure of 26 Pa. The decay curve of the hydrogen radical density was well fitted by a single exponential function, which suggests that three body recombination is negligible, as shown in Fig. 3.2. D was determined to be $3.1 \times 10^5 \text{ cm}^2 \text{ Pa s}^{-1}$ from the slope shown in Fig. 3.3, which corresponds well to the theoretical calculation ($3.1 \times 10^5 \text{ cm}^2 \text{ Pa s}^{-1}$ at gas temperature of 400 K) by Chapman-Enskog theory with a Lennard-Jones intermolecular potential.^{31,32} The surface loss probability on the stainless steel wall was estimated to be 0.12 on the basis of the decay time constants in Fig. 3.3 and Eq.(3.15). This value agreed well with previous reports.^{20,21}

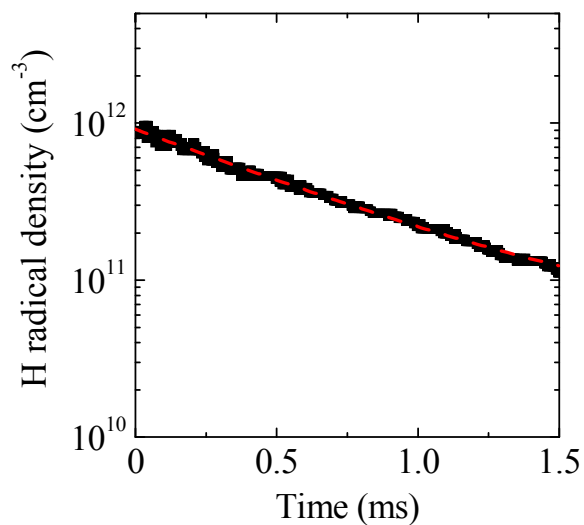


Fig. 3.2 Typical decay of the H radical density in the H₂ plasma afterglow when the chamber wall was covered with no Si film. The dashed lines are results of fitting with single exponential functions.

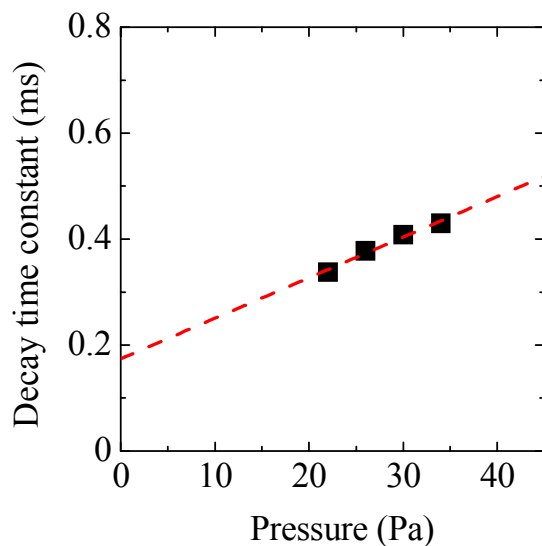


Fig. 3.3 Decay time constants of H radical density as a function of total pressure in H₂ plasma afterglow on stainless steel wall. The dashed line is result of fitting with linear function.

3.3.2 H radical densities in SiH₄/H₂ plasmas

Figure 3.4 shows the absolute H radical density as a function of the SiH₄ flow rate. The SiH₄/H₂ plasma was turned on at a SiH₄/H₂ flow rate of 1/100 sccm for 1 h prior to the measurement as a pre-treatment. Si thin films were deposited on the chamber wall when all measurements were carried out. The H₂ flow rate and the wall temperature were maintained at 100 sccm and ca. 310 K, respectively. The H radical density decreased significantly from 4.3×10^{12} to $6.8 \times 10^{11} \text{ cm}^{-3}$ with increase in the SiH₄ flow rate from 0 to 3 sccm. This is probably due to enhancement of the H radical loss by the introduction of SiH₄; the recombination reaction of H radicals with SiH₄ and surface loss to the chamber wall are considered to be the main loss mechanisms of H radicals in the SiH₄/H₂ plasma.

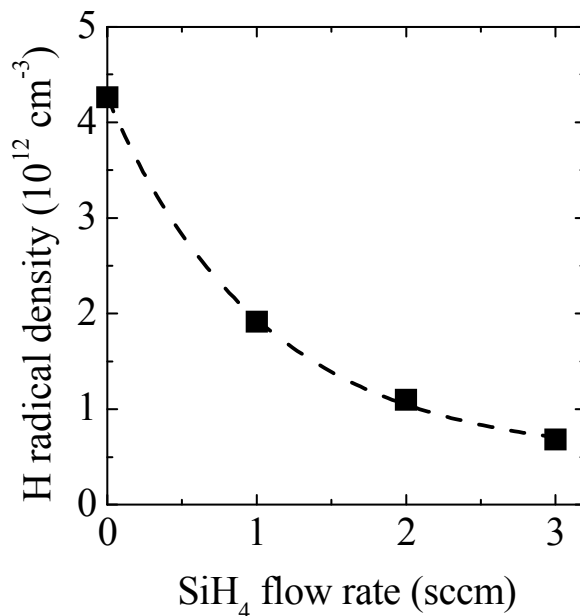


Fig. 3.4 H radical density as a function of the SiH₄ flow rate at a pressure of 40 Pa and an rf power of 350 W. The dashed line is guide to the eye.

3.3.3 Surface loss probability of H radicals in SiH₄/H₂ plasma

Figure 3.5 shows typical curves for the H radical density decay in the afterglow plasma produced by on-off modulated SiH₄/H₂ discharge at a pulsed rf power of 350 W, a pressure of 40 Pa, a SiH₄/H₂ gas flow of from 0–3/100 sccm and a wall temperature of 310 K. The H radical density decay curves could be well fitted with the exponential function, which suggests that three body recombination is negligible. Figure 3.6 shows the measured decay time constant of H radicals in the plasma afterglow as a function of the SiH₄ flow rate. The surface loss probability was calculated using the measured decay time constant, Eqs. (3.9) and (3.15). D for H radicals in the SiH₄/H₂ plasma is assumed to be almost the same as D in a pure H₂ plasma, because the flow rate of SiH₄ was less than that of H₂ by two orders of magnitude. The surface loss probability of H radicals as a function of the SiH₄ flow rate is shown in Fig. 3.7. The surface loss probability increased from 0.01 to 0.32 with increase in the SiH₄ flow rate, which indicates that the loss probability of H radicals is dependent on the surface conditions determined by incident species such as radicals and ions. Consequently, the surface loss probability is significantly changed by variation of the SiH₄ flow rate and the surface loss probability is considered to be influenced by the species generated from SiH₄.

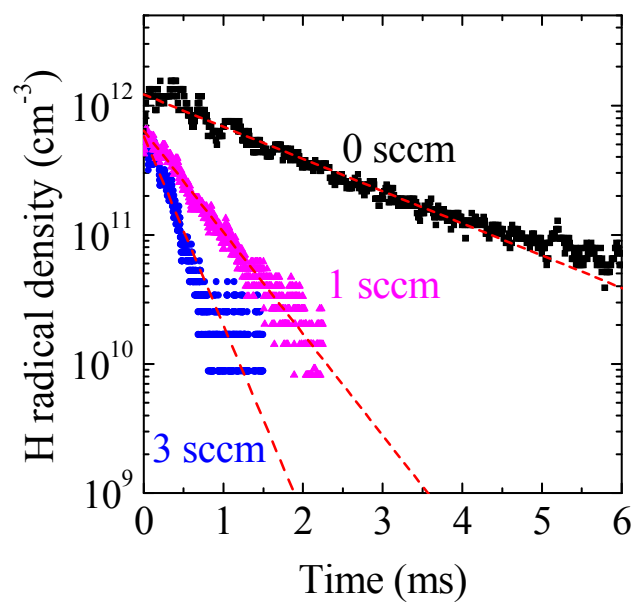


Fig. 3.5 Typical decay of the H radical density in the SiH₄/H₂ plasma afterglow. The dashed lines are results of fitting with single exponential functions.

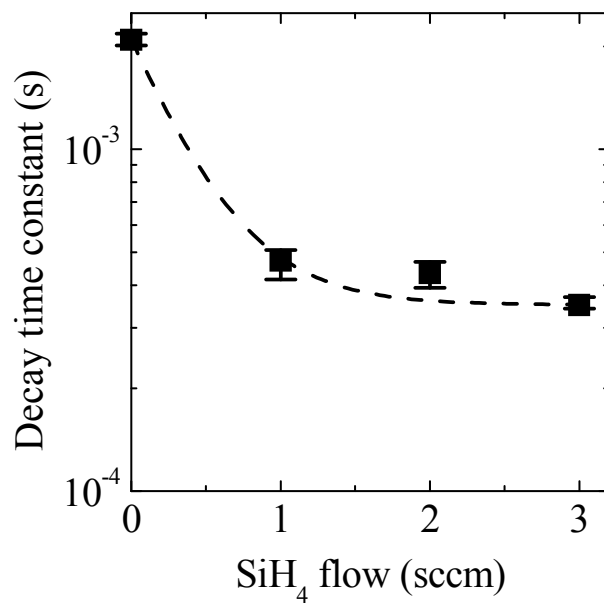


Fig. 3.6 Measured decay time constant of H radicals as a function of the SiH₄ flow rate. The dashed line is guide to the eye.

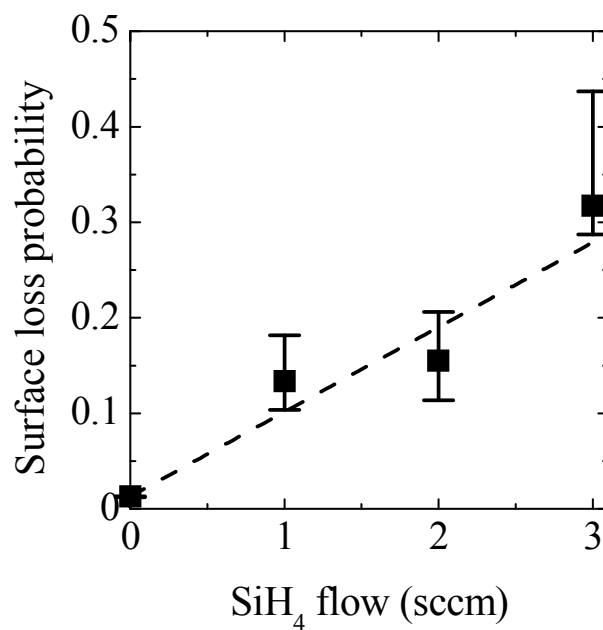


Fig. 3.7 Surface loss probability of H radicals as a function of the SiH₄ flow rate. The dashed line is guide to the eye.

3.3.4 Surface analysis of thin films deposited on chamber wall

Figure 3.8 shows an increase in the deposition rate with increase in the SiH₄ flow rate, which indicates that the density of film precursors increased with the SiH₄ flow rate. Figure 3.9 shows Raman spectra for the deposited films as a function of the SiH₄ flow rate. The spectra include three peaks corresponding to crystalline (520 cm⁻¹), defective crystalline (510 cm⁻¹), and amorphous (480 cm⁻¹) phases. The Raman spectra were decomposed into these peaks and the crystalline factor ϕ_c , was calculated as follows³³:

$$\phi_c = \frac{I_{520} + I_{510}}{I_{520} + I_{510} + I_{480}}, \quad (3.16)$$

where I_k is the area under the Gaussian curve centered at k , and k is the Raman shift. The ϕ_c decreased from 0.57 to 0 with increase in the SiH₄ flow rate, due to an increase of film precursors and a decrease of H radicals. The flux ratio of H radicals to film precursors is a key parameter for the resultant crystallinity of $\mu\text{c-Si:H}$.³⁴⁻³⁷ A sufficient supply of H radicals to the film growth surface enhances crystallization of the Si thin films.

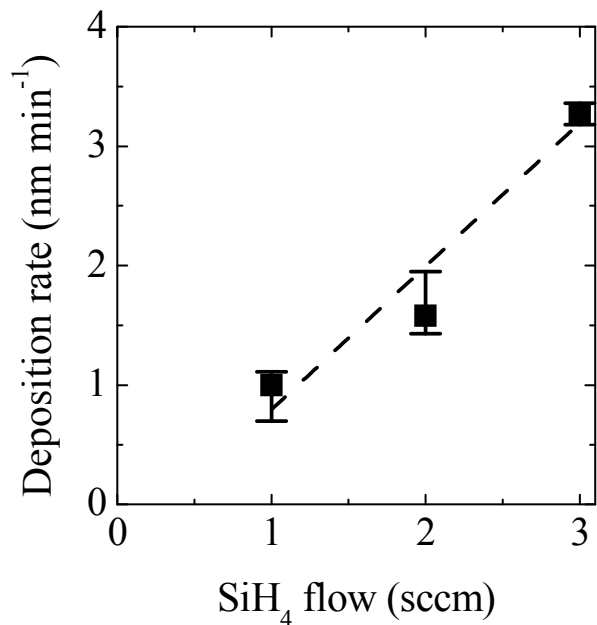


Fig. 3.8 Deposition rate of Si thin films on the chamber wall as a function of the SiH₄ flow rate. The dashed line is guide to the eye.

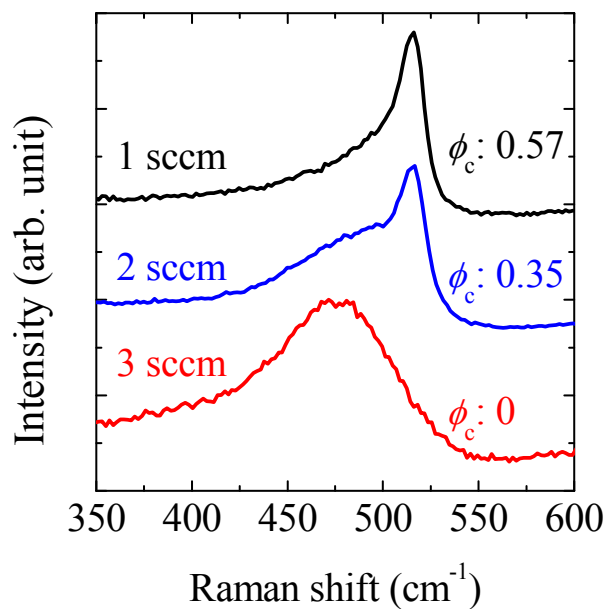
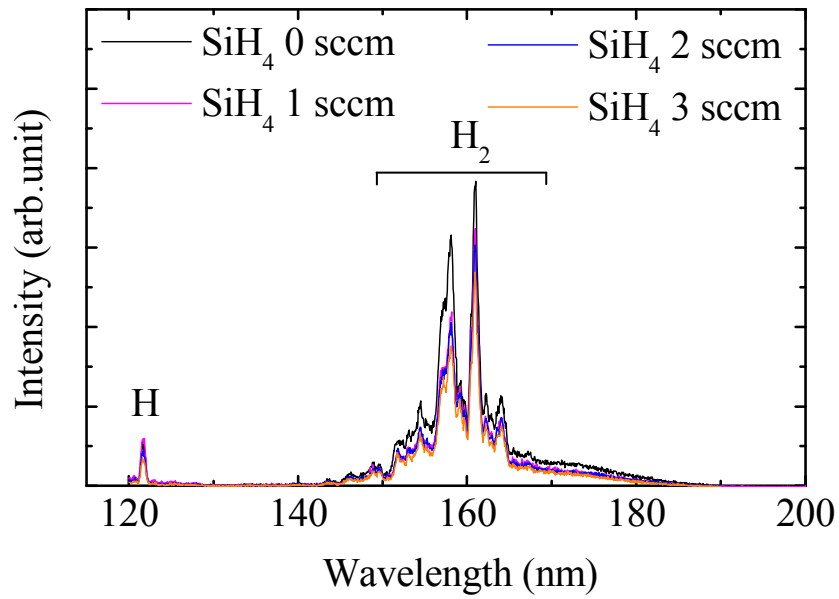


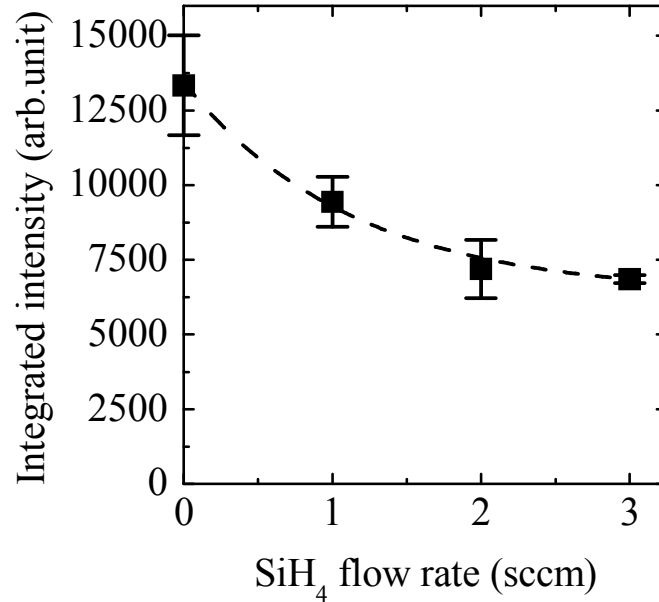
Fig. 3.9 Raman spectra of Si thin films deposited on the chamber wall at various SiH₄ flow rates.

3.3.5 Measurement of VUV radiation from SiH₄/H₂ plasma

The photon energy of VUV radiation from the plasma is sufficient to break and activate chemical bonds on the surface of the film. A synergetic effect of radicals and VUV photons is reported to contribute to chemical reactions in the field of plasma etching, wherein etch rates obtained by radicals and VUV irradiation are higher than those obtained with only radicals.³⁸ Therefore, there is a possibility that VUV photons influence the surface condition during plasma discharge, so that the surface loss probability of H radicals is changed by the VUV irradiation. Actually, VUV photons have been reported to influence the surface loss probabilities of H and N radicals in H₂/N₂ plasma.²² To investigate the effect of VUV on the surface loss probability, the optical emission intensities in the VUV region were measured. Figure 3.10(a) shows optical emission spectra measured below the wavelength of 200 nm. Peaks in the spectra for various SiH₄ flow rates were estimated to be due to H (121.6 nm) or H₂ (150–170 nm). The integrated intensities of the spectra are shown as a function of the SiH₄ flow rate in Fig. 3.10(b). The intensity decreased with increasing SiH₄ flow rate, because the SiH₄ molecule absorbs VUV light.³⁹ The pure H₂ plasma and SiH₄/H₂ mixture plasma have VUV light emission. However, the VUV intensities decreased and the surface loss probability increased with increasing SiH₄ flow rate; therefore, the VUV effects on increasing the surface loss probability was not observed for the SiH₄/H₂ plasma.



(a)



(b)

Fig. 3.10 (a) Optical emission spectra below 200 nm for at various SiH_4 flow rates and (b) integrated intensity of the spectrum as a function of the SiH_4 flow rate. The dashed line is guide to the eye.

3.3.6 Dependence of the absolute density and surface loss probability of H radicals on the temperature of the chamber wall

Si thin films are generally deposited at a substrate temperature of around 473 K. To investigate the surface reaction of H radicals at higher temperatures, the chamber wall was heated to 473 K at a SiH₄ flow rate of 1 sccm. However, the decay time constant could not be obtained at 473 K, because the absorption ratio of H radicals was too low to estimate an accurate density of H radicals in the plasma afterglow. Therefore, the density of H radicals in the plasma was measured instead of that in the plasma afterglow. Figure 3.11 shows a significant reduction in the H radical density by heating the chamber wall up to 473 K in the plasma. The density of H radicals in the steady-state plasma is given by:

$$N(\text{H}) = \frac{n_e [\langle \sigma_{\text{H}_2} v_e \rangle N(\text{H}_2) + \langle \sigma_{\text{SiH}_4} v_e \rangle N(\text{SiH}_4)]}{1/\tau_d + k_2 N(\text{SiH}_4)}. \quad (3.17)$$

The diffusion lifetime of H radicals at a wall temperature of 473 K was calculated to be 0.15 ms using Eq. (3.17), and the density of H radicals at 473 K. $n_e [\langle \sigma_{\text{H}_2} v_e \rangle N(\text{H}_2) + \langle \sigma_{\text{SiH}_4} v_e \rangle N(\text{SiH}_4)]$ and $k_2 N(\text{SiH}_4)$ were estimated from the diffusion lifetime, the density of H radicals at 310 K, and assuming that the gas temperature is 473 K and that the electron density and electron temperature are the same at both temperatures. The surface loss probability of H radicals at 473 K was estimated to be ca. 1 from the estimated diffusion lifetime. Thus, the increase of surface loss probability is due to the increased activation of surface reactions at higher temperatures.

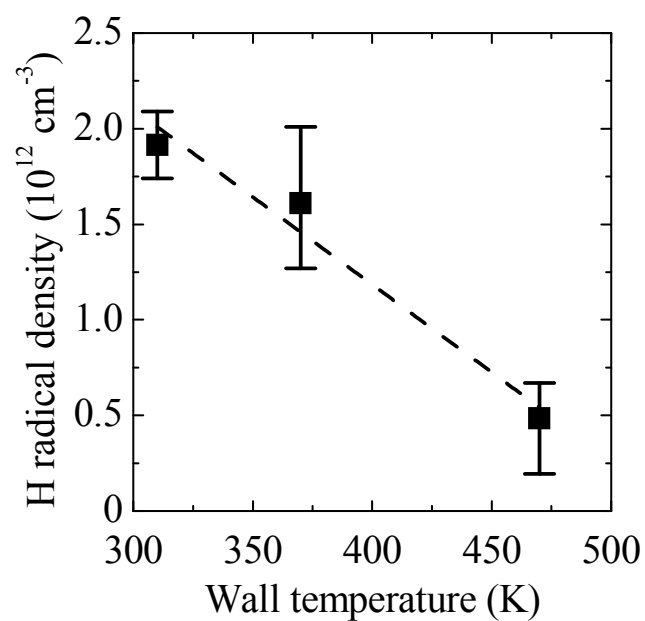


Fig. 3.11 H radical density in the plasma as a function of the wall temperature at a SiH_4 flow rate of 1 sccm, pressure at 40 Pa and rf power at 350 W. The dashed line is guide to the eye.

3.4. Discussion

Kinetic models for the surface reactions of H radicals in SiH₄/H₂ plasma are listed as follows: (a) physical adsorption and desorption; (b) surface diffusion after physical adsorption; (c) chemical adsorption and desorption at chemically active vacant sites on the surface; (d) the reaction of physisorbed H radicals with physisorbed or chemisorbed H and SiH₃, which leads to the formation of H₂ and SiH₄; (e) insertion in Si–Si bonds; (f) diffusion in Si thin films.

The loss mechanisms of H radicals on Si surface in pure H₂ plasma are recombination reactions with physisorbed or chemisorbed H atoms on the surface (a, b, c, d), insertions into Si–Si bonds followed by Si etching ($4\text{H} + \text{Si} \rightarrow \text{SiH}_4$) (e), and diffusion into the subsurface (f). In a SiH₄/H₂ mixture plasma, species generated from SiH₄, such as SiH_x radicals and ions, have an additional influence on the surface loss probability. SiH₃ radicals can abstract a H atom from the surface, which leaves a dangling bond on which H radicals adsorb (c). During deposition, SiH₃ is constantly adsorbed on the surface. The reaction between H radicals and adsorbed SiH₃ occurs more easily than the insertion of H radicals in Si–Si bonds (d). Therefore, the surface loss probability of H radicals increases with the SiH₄ flow rate.

The deposition rate dependence on the SiH₄ flow rate shown in Fig. 3.8 supports the increase in SiH₃ radicals, which are a dominant film precursor, with increasing SiH₄ flow rate. The crystallinity decreased with increasing SiH₄ flow rate, as shown in Fig. 3.9, and the degradation of crystallinity is probably due to change of the surface reactions during deposition. When there are many dangling surface bonds or the surface coverage of H atoms is low, SiH₃ radicals are unable to diffuse long distances, which leads to degradation of the crystallinity. Furthermore, reactions of physisorbed H radicals with physisorbed or chemisorbed SiH₃ increase with the SiH₄ flow rate. Consequently, the surface conditions and reactions of H radicals that induce

crystallization, such as the surface coverage, etching of the amorphous phase, and modification of the Si–Si network, are relatively decreased.

SiH_x ions are heavier than H_x ions, so that the formation of surface dangling bonds seems to be enhanced by SiH_x ion bombardment during plasma discharge. VUV photons have been reported to influence the surface loss probabilities of H and N radicals in H_2/N_2 plasma²². VUV emissions were observed in SiH_4/H_2 plasma, and VUV photons possibly influence the surface reactions of H radicals. However, the VUV intensities decreased and the surface loss probability increased with increasing SiH_4 flow rate; therefore, the VUV effects are smaller than other factors that increase the surface loss probability with increasing SiH_4 flow rate.

The diffusion lifetime was calculated, with some assumptions, on the basis of the decrease in the H radical density by heating the wall surface. The surface loss probability was estimated to be ca. 1 at the high temperature of 473 K, as shown in section 3.3.6. This is due to the activation of reactions by heating. Thus, the surface loss probability of H radicals during practical deposition process of Si thin film is almost unity, because the substrate is generally heated up to around 473 K. Furthermore, this indicates that cooling of the chamber wall is a key factor for achieving a high density of H radicals. Although low temperatures favor high H radical densities, they do not favor high film quality because surface diffusion of SiH_3 is slow¹ and surface reactions of H radicals are suppressed at low temperature. Therefore, substrate temperatures are individually heated up to ca. 473 K to achieve high film quality and other parts of a chamber such as inner walls and powered electrodes are oppositely cooled down to obtain enough high H radical density in deposition processes of Si thin film.

3.5. Conclusion

The surface loss probability of H radicals in SiH₄/H₂ plasma afterglow was investigated using VUVAS. The decay of H radicals in the afterglow plasma was measured and the diffusion lifetime was calculated by considering the reaction between H radicals and SiH₄ molecules. The surface loss probability was estimated from the diffusion lifetime and was higher in the SiH₄/H₂ mixture plasma than in H₂ pure plasma and increased with increasing SiH₄ flow rate. The surface condition was investigated by analyzing the deposition rate and the crystallinity of Si thin films deposited on the chamber wall. On the basis of these results and with consideration of the reactions on the surface, it was concluded that deposition species such as SiH₃ radicals generated from SiH₄ influence the surface loss probability of H radicals. Furthermore, the density of H radicals was significantly decreased by heating the chamber wall. Surface reactions are enhanced by heating and the surface loss probability is ca. 1 at 473 K. The quantitative results for the surface loss probability of H radicals obtained in this study are important to understand not only plasma-surface reactions, but will also contribute to improvements in the control of plasma processing and the design of equipment.

3.6 References

- ¹ A. Matsuda, *J. Non-Cryst. Solids* **338-340**, 1 (2004).
- ² Y. Toyoshima, K. Arai, A. Matsuda, and K. Tanaka, *Appl. Phys. Lett.* **56**, 1540 (1990).
- ³ C. C. Tsai, G. B. Anderson, R. Thompson, and B. Wacker, *J. Non-Cryst. Solids* **114**, 151 (1989).
- ⁴ S. Kumar, B. Drevillon, and C. Godet, *J. Appl. Phys.* **60**, 1542 (1986).
- ⁵ R. Nozawa, H. Takeda, M. Ito, M. Hori, and T. Goto, *J. Appl. Phys.* **85**, 1172 (1999).
- ⁶ I. Solomon, B. Drévillon, H. Shirai, and N. Layadi, *J. Non-Cryst. Solids* **164-166**, 989 (1993).
- ⁷ O. Vetterl, F. Finger, R. Carius, P. Hapke, L. Houben, O. Kluth, A. Lambertz, A. Mück, B. Rech, and H. Wagner, *Sol. Energy Mater. Sol. Cells* **62**, 97 (2000).
- ⁸ A. D. Tserepi and T. A. Miller, *J. Appl. Phys.* **75**, 7231 (1994).
- ⁹ S. Takashima, K. Takeda, S. Kato, M. Hiramatsu, and M. Hori, *Jpn. J. Appl. Phys.* **49**, 076101 (2010).
- ¹⁰ N. Itabashi, N. Nishiwaki, M. Magane, S. Naito, T. Goto, A. Matsuda, C. Yamada, and E. Hirota, *Jpn. J. Appl. Phys.* **29**, L505 (1990).
- ¹¹ M. Shiratani, H. Kawasaki, T. Fukuzawa, Y. Watanabe, Y. Yamamoto, S. Suganuma, M. Hori, and T. Goto, *J. Phys. D: Appl. Phys.* **31**, 776 (1998).
- ¹² C. Suzuki, K. Sasaki, and K. Kadota, *Jpn. J. Appl. Phys.* **36**, L824 (1997).
- ¹³ Y. Hikosaka, H. Toyoda, and H. Sugai, *Jpn. J. Appl. Phys.* **32**, L690 (1993).
- ¹⁴ M. Shiratani, J. Jolly, H. Vidjelot, and J. Perrin, *Jpn. J. Appl. Phys.* **36**, 4752 (1997).
- ¹⁵ K. Sasaki, K. Usui, H. Furukawa, C. Suzuki, and K. Kadota, *Jpn. J. Appl. Phys.* **37**, 5047 (1998).
- ¹⁶ H. Ito, K. Teii, H. Funakoshi, M. Hori, T. Goto, M. Ito, and T. Takeo, *J. Appl. Phys.* **88**, 4537 (2000).
- ¹⁷ H. Nagai, M. Hiramatsu, M. Hori, and T. Goto, *Rev. Sci. Instrum.* **74**, 3453 (2003).

- ¹⁸ J. P. Booth and N. Sadeghi, *J. Appl. Phys.* **70**, 611 (1991).
- ¹⁹ K. Sasaki, Y. Kawai, C. Suzuki, and K. Kadota, *J. Appl. Phys.* **82**, 5938 (1997).
- ²⁰ S. Takashima, M. Hori, T. Goto, A. Kono, and K. Yoneda, *J. Appl. Phys.* **90**, 5497 (2001).
- ²¹ J. Jolly and J. P. Booth, *J. Appl. Phys.* **97**, 103305 (2005).
- ²² C. S. Moon, K. Takeda, S. Takashima, M. Sekine, Y. Setsuhara, M. Shiratani, and M. Hori, *J. Appl. Phys.* **107**, 103310 (2010).
- ²³ Y. Abe, S. Kawashima, K. Takeda, M. Sekine, and M. Hori, *Appl. Phys. Express* **3**, 106001 (2010).
- ²⁴ G. A. Curley, L. Gatilova, S. Guilet, S. Bouchoule, G. S. Gogna, N. Sirse, S. Karkari, and J. P. Booth, *J. Vac. Sci. Technol. A* **28**, 360 (2010).
- ²⁵ P. Kae-Nune, J. Perrin, J. Jolly, and J. Guillon, *Surf. Sci.* **360**, L495 (1996).
- ²⁶ S. Takashima, M. Hori, T. Goto, A. Kono, M. Ito, and K. Yoneda, *Appl. Phys. Lett.* **75**, 3929 (1999).
- ²⁷ S. Takashima, M. Hori, T. Goto, and K. Yoneda, *J. Appl. Phys.* **89**, 4727 (2001).
- ²⁸ B. Gordiets, C. M. Ferreira, M. J. Pinheiro, and A. Ricard, *Plasma Sources Sci. Technol.* **7**, 363 (1998).
- ²⁹ J. Perrin, O. Leroy, and M. C. Bordage, *Contrib. Plasma Phys.* **36**, 3 (1996).
- ³⁰ P. J. Chantry, *J. Appl. Phys.* **62**, 1141 (1987).
- ³¹ R. C. Reid, J. M. Prausnitz, and T. K. Sherwood, *The Properties of Gases and Liquids* (McGraw-Hill, New York, 1977).
- ³² R. A. Svehla, NASA Lewis Research Center Technical Report No. R-132, 1962.
- ³³ C. Droz, E. Vallat-Sauvain, J. Bailat, L. Feitknecht, J. Meier, and A. Shah, *Sol. Energy Mater. Sol. Cells* **81**, 61 (2004).
- ³⁴ B. Strahm, A. A. Howling, L. Sansonnens, and C. Hollenstein, *Plasma Sources Sci. Technol.* **16**, 80 (2007).
- ³⁵ S. Nunomura and M. Kondo, *J. Phys. D* **42**, 185210 (2009).

Chapter 3

- ³⁶ G. Dingemans, M. N. van den Donker, D. Hrunski, A. Gordijn, W. M. M. Kessels, and M. C. M. van de Sanden, *Appl. Phys. Lett.* **93**, 111914 (2008).
- ³⁷ Y. Abe, A. Fukushima, K. Takeda, H. Kondo, K. Ishikawa, M. Sekine, and M. Hori, *Appl. Phys. Lett.* **101**, 172109 (2012).
- ³⁸ C. S. Moon, K. Takeda, M. Sekine, Y. Setsuhara, M. Shiratani, and M. Hori, *J. Appl. Phys.* **107**, 113310 (2010).
- ³⁹ U. Itoh, *J. Chem. Phys.* **85**, 4867 (1986).

Chapter 4 Investigation of H and SiH₃ Radicals in Microcrystalline Silicon Deposition

4.1 Introduction

Hydrogenated microcrystalline silicon ($\mu\text{c-Si:H}$) thin film fabricated by plasma enhanced chemical vapor deposition (PECVD) is a promising material for photovoltaic applications. H radicals play an important role in the deposition of $\mu\text{c-Si:H}$ thin films. Some models have been proposed for the reactions of H radicals on the film-growth surface. During deposition of a silicon film, H radicals cover the growth surface and the surface dangling-bonds undergo reduction. H radicals induce local heating through recombination reaction to produce hydrogen molecules. These two events occur on the surface and enhance surface diffusion of the film growth precursors. Precursors can then find stable adsorption sites and form stable Si–Si bonds.¹ H radicals etch the weakly bonded Si atoms in amorphous phase and assist in the reconstruction of the Si–Si bond network in H-rich subsurface regions.^{2–4} Thus, the phase transition of amorphous silicon (a-Si:H) to $\mu\text{c-Si:H}$ is induced by a sufficient supply of H radicals.

The process margin to obtain high quality $\mu\text{c-Si:H}$ thin films for solar cells is very narrow just prior to entering the a-Si:H growth regime.⁵ The transition from $\mu\text{c-Si:H}$ to a-Si:H growth has been recognized as being determined by the ratio of H radical flux to silicon deposition flux. It was reported that the flux ratio was 40 by employing an etch product detection technique and the flux ratio was 100 by deducing the H radical density from the decomposition process of SiH₄ molecules.^{6,7} However, these techniques are not the measurement of the absolute density of radicals. Therefore, in the present work, the absolute density and the translational temperature of H radicals were measured using vacuum ultraviolet laser absorption spectroscopy (VUVLAS). The absolute density of SiH₃ radicals are also measured by cavity ring-down spectroscopy

Chapter 4

(CRDS). From these results, fluxes of H and SiH₃ radicals were estimated. Experiments were conducted under high pressure and high power discharge for high rate deposition of $\mu\text{c-Si:H}$ thin films.

4.2 Experimental details

Figure 4.1 shows a schematic diagram of the capacitively coupled plasma (CCP) chamber with (a) a VUVLAS system for measurement of the H radical density and (b) a CRDS system for measurement of the SiH₃ radical density. A VHF (60 MHz) power of 400 W was supplied to the upper electrode to sustain plasma discharge. The SiH₄ gas flow rate was varied from 7 to 15 sccm and the H₂ gas flow rate was fixed at 470 sccm. The gas mixture was introduced from a shower-head in the cathode plate of the CCP system. The total pressure was maintained at 1200 Pa (9 Torr) by controlling the vacuum conductance of pumping system. Glass (Corning, EAGLE XG™) and quartz substrates were placed on the grounded electrode, and heated to 523 K. The gap between the cathode plate and substrate was fixed at 10 mm. The crystallinity factor and preferential orientation of Si films deposited on the glass substrate were analyzed using Raman spectroscopy and X-ray diffraction (XRD), respectively. The defect density of the films deposited on quartz substrates was measured using electron spin resonance (ESR) spectroscopy.

The VUVLAS system for the Lyman α line at 121.6 nm consists of a two-dye-laser system and a Kr gas cell. The VUV laser was generated by employing the two-photon-resonance four-wave-sum frequency mixing technique, which was passed through the CCP and then focused on the slit of the VUV monochromator (Acton Research Corp., ARC VM-520) with MgF₂ lens and detected by the photomultiplier tube (Hamamatsu, R8487). Slits were used as the end caps of the ceramic pipes for adjustment of the absorption length to 100 mm, because MgF₂ window was inapplicable owing to the film deposition on any window. H₂ gas was introduced in the pipes at a flow rate of 30 sccm to prevent silicon deposition on the MgF₂ lenses after the gas cell and in front of the VUV monochromator. Thus, the total flow rate of H₂ gas was 500 sccm.

Chapter 4

Optical cavity for CRDS consists of two plano-concave highly reflective mirrors (Laser optik). The cavity mirrors were also blown by H₂ of 30 sccm to prevent film deposition. The cavity length, determined by the distance between the cavity mirrors was 170 cm. Two sets of narrow-bandwidth high-reflectivity mirrors have been used. One set optimized for the 220 nm range with reflectivity R=99.2%, and the other one was optimized for the 280 nm range with reflectivity R=99.2%. The CRD laser light pulses at wavelengths of 220 and 280 nm are obtained by optical parametric oscillator (OPO) laser pumping by the frequency-tripled output of a Nd:YAG laser. The pulse duration and repetition rate are 8 ns and 10 Hz, respectively. The light leaking out of the cavity at the back mirror was detected by the photomultiplier (Hamamatsu, R928) with the bandpass filter. The cavity ring-down transients are recorded with a digital oscilloscope. A delay generator and pulse generator are used to tune the delay time between the plasma ignition and the generation of the laser pulse.

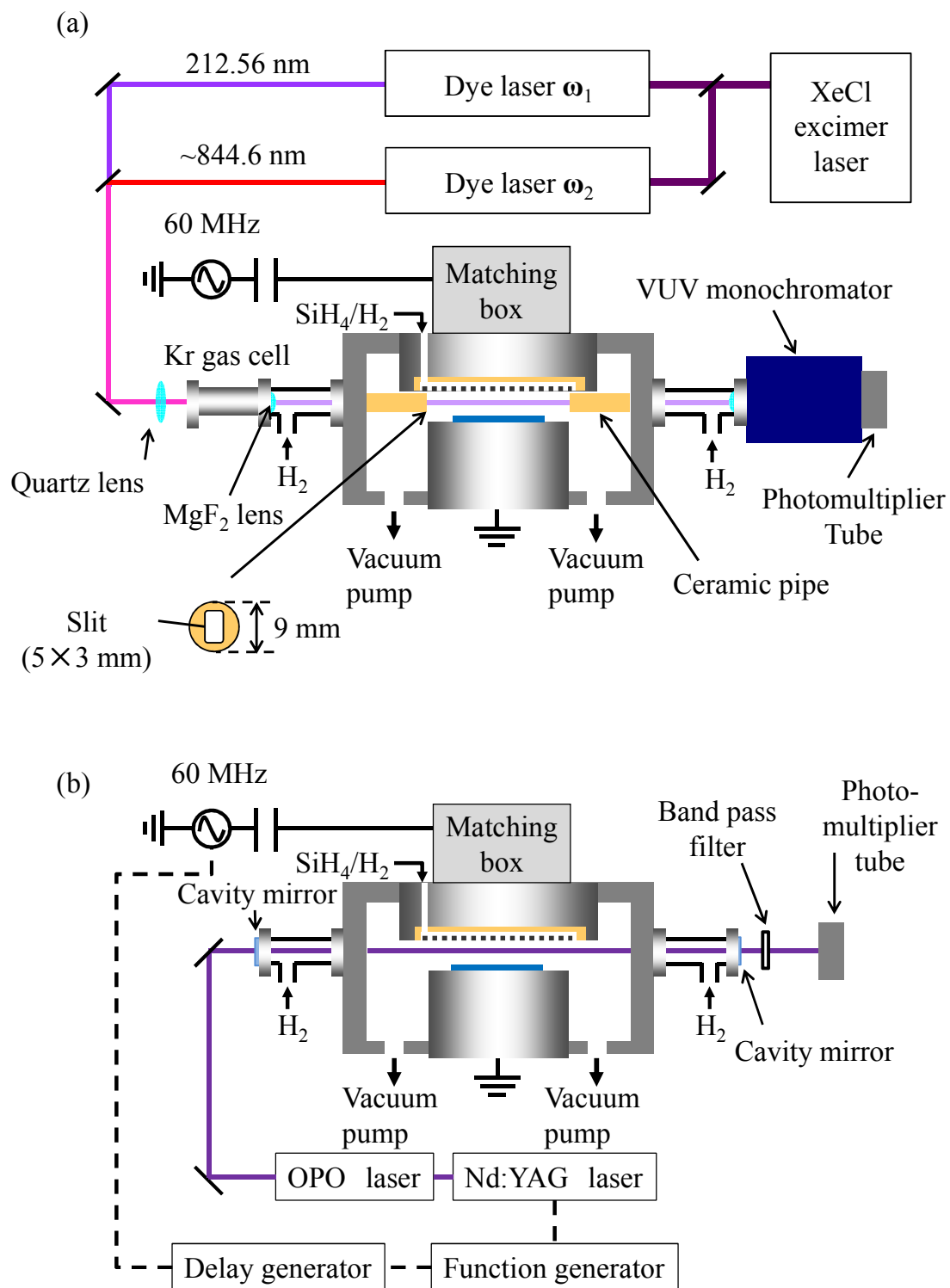


Fig. 4.1 Schematic diagrams of each experimental setup for CCP with (a) VUVLAS system and (b) CRDS system.

4.3 Results and discussion

4.3.1 Measurement of H radicals

Figure 4.2 shows typical absorption spectra of the Lyman α line measured by varying the frequency (ν_1) of the laser. These absorption spectra are fitted by

$$\alpha(\nu_1) = \frac{\int f_a(\nu) [1 - \exp\{-k_0 f_a(\nu)L\}] d\nu}{\int f_a(\nu) d\nu}, \quad (4.1)$$

where $f_a(\nu)$ is the absorption line profile function, k_0 is the absorption coefficient at the center frequency (ν_0) of $f_a(\nu)$, and L is the absorption length. $f_a(\nu)$ is assumed to be a Gaussian form. Firstly, the line width for instrumentation was checked by measuring the absorption profile of the Xe line at 129.56 nm, and the full width at half maximum ($\Delta\nu$) of the laser source was obtained as 0.4 cm^{-1} . In the other contribution, Doppler broadening is a main factor given by

$$\Delta\nu = 2\sqrt{2 \ln 2} \left(\frac{kT}{Mc^2} \right)^{\frac{1}{2}} \nu_0, \quad (4.2)$$

where k is the Boltzmann constant, T is the translational temperature, M is mass, and c is the speed of light. The values of k_0 and $\Delta\nu$ of f_a were parameterized, so that both the absolute density and the translational temperature of the H radicals were determined. The absorptions in Fig. 4.2 were saturated near the center frequency. In this instance, the translational temperature cannot be accurately determined if two temperature distribution exist, which inhibits fitting the absorption profile to a Gaussian profile.⁸ In the present results, the shoulders of the measured absorption profile could be fitted to a Gaussian profile. Therefore, a two temperature distribution was not apparent.

Figure 4.3 shows the dependence of the absolute density and translational temperature of H radicals on the SiH_4 flow rate. The density was constant at around

$5.5 \times 10^{12} \text{ cm}^{-3}$ and the translational temperature was constant at around 770 K. SiH_4 molecules act as scavengers of H radicals through the following reaction:



However, the measured density of H radical did not decrease with increasing SiH_4 flow rate, which is probably due to that SiH_4 was sufficiently depleted and the annihilation of H radicals was prevented. The high depletion of SiH_4 is due to the high electron density obtained effectively by the VHF power source.⁹

The flux of H radicals was evaluated from the measurement results and is shown in Fig. 4.4. The H radical flux Γ_{H} , was calculated using the following equation:

$$\Gamma_{\text{H}} = \frac{1}{4} n \sqrt{\frac{8k_{\text{B}}T}{\pi m}}, \quad (4.4)$$

where n , T , and m represent the absolute density, translational temperature, and the atomic mass of H atom ($m = 1.66 \times 10^{-27} \text{ kg}$), respectively, and k_{B} is the Boltzmann constant. The surface reaction probability of H radicals was assumed to be 1.0 which is estimated from the afterglow measurement in Chapter 3. The flux of effective H radicals to the surface reactions was estimated to be constant at $5.7 \times 10^{17} \text{ cm}^{-2} \text{ s}^{-1}$.

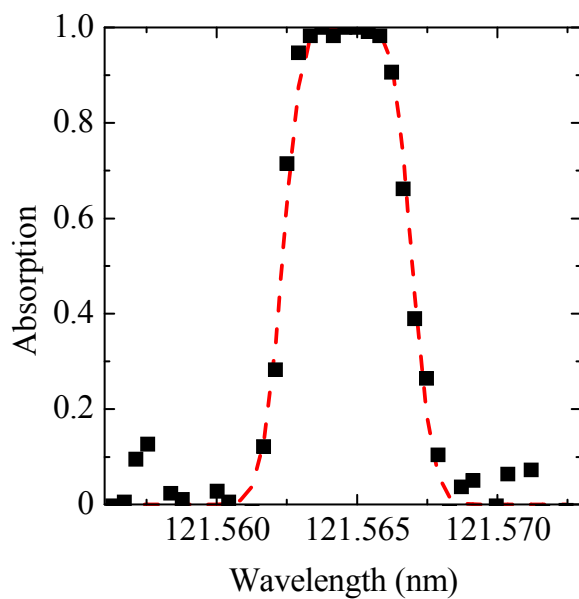


Fig 4.2 Typical absorption spectra of the Lyman α line

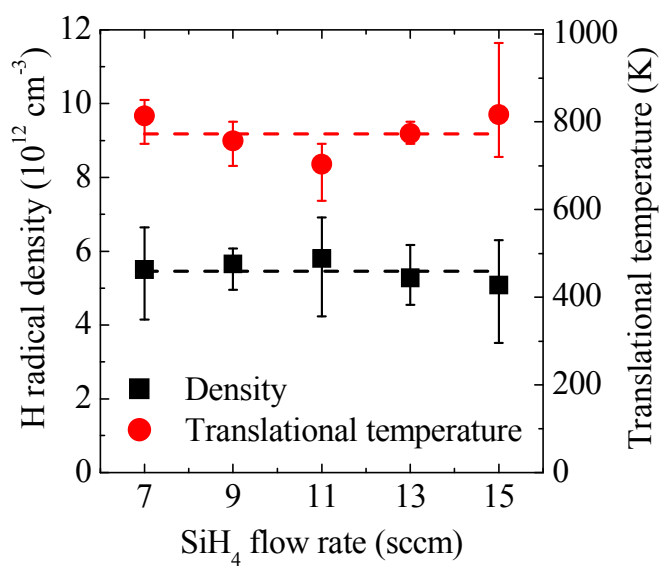


Fig. 4.3 Absolute density and translational temperature of H radicals as a function of the SiH₄ flow rate. The dashed line is guide to the eye.

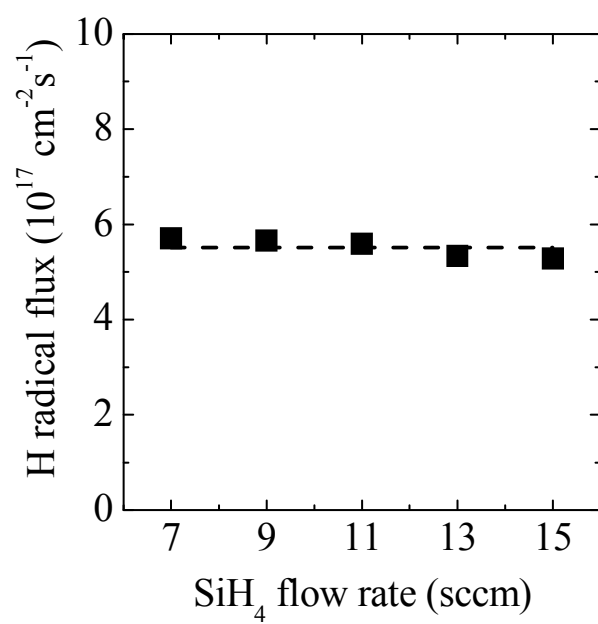


Fig. 4.4 Flux of H radicals as a function of the SiH_4 flow rate. The dashed line is guide to the eye.

4.3.2 Investigation of the behavior of the H radical density on the basis of the calculation

The behavior of the H radical density was investigated on the basis of the calculation, in particular, focusing on the fact that the H radical density was almost constant against SiH₄ flow rate as shown in Fig. 4.3. The density of H radicals was estimated from following rate equations:

$$\frac{dN(\text{H}_2)}{dt} = \Phi_{\text{H}_2} + k_3 N(\text{H})N(\text{SiH}_4) - (2k_1 n_e + 1/\tau_{\text{pump}})N(\text{H}_2), \quad (4.5)$$

$$\frac{dN(\text{SiH}_4)}{dt} = \Phi_{\text{SiH}_4} - (k_2 n_e + k_3 N(\text{H}) + 1/\tau_{\text{pump}})N(\text{SiH}_4), \quad (4.6)$$

$$\frac{dN(\text{H})}{dt} = k_1 n_e N(\text{H}_2) + k_2 n_e N(\text{SiH}_4) - (k_3 N(\text{SiH}_4) + 1/\tau_d)N(\text{H}), \quad (4.7)$$

where Φ_x is the input molecular flow rates per unit of volume of x, k_x for x=1, 2, 3 is the rate constant for the reaction described by the each equation of (3.1), (3.2), and (4.1), $N(x)$ is the density of x, τ_{pump} is the loss time by pumping action, and τ_d is the diffusion lifetime of H radicals. k_1 is $1.7 \times 10^{-11} \text{ cm}^{-6} \text{ s}^{-1}$, k_2 is $4.2 \times 10^{-10} \text{ cm}^{-6} \text{ s}^{-1}$, and k_3 is $2 \times 10^{-12} \text{ cm}^{-6} \text{ s}^{-1}$, respectively, when the electron energy distribution function is assumed to be Maxwellian at the electron temperature of 1.5 eV and gas temperature is 473 K.¹⁰⁻¹²

Prior to the calculation of the H radical density, behaviors of $k_1 n_e$ and $k_2 n_e$ were evaluated from the optical emission of Xe. The threshold energy of the Xe emission (823.1 nm) is 9.82 eV which is close to those of the electron impact dissociation of SiH₄ (8.75 eV) and H₂ (8.8 eV), therefore behaviors of $k_1 n_e$ and $k_2 n_e$ can be estimated from the behavior of Xe emission intensity.¹³ Figure 4.5 (a) shows the optical emission spectrum when a small amount (1 sccm) of Xe was added to the parent gases, in which emission lines of Xe were observed at 823.1 and 828.0 nm. As seen in Fig. 4.5 (b), the

Xe emission intensity was constant against SiH₄ flow rate, therefore k_1n_e and k_2n_e are estimated to be constant in the experimental condition.

Figure 4.6 shows the measured H radical density and the calculated H radical density as a function of SiH₄ flow rate, where the calculation was carried out with assuming the electron density to be 10^{10} cm^{-3} . The behavior of the calculated H radical density approximately agrees with that of measured H radical density. From the calculating result, the consideration that the loss of H radicals by the reaction with SiH₄ is not significant in the present conditions is theoretically supported.

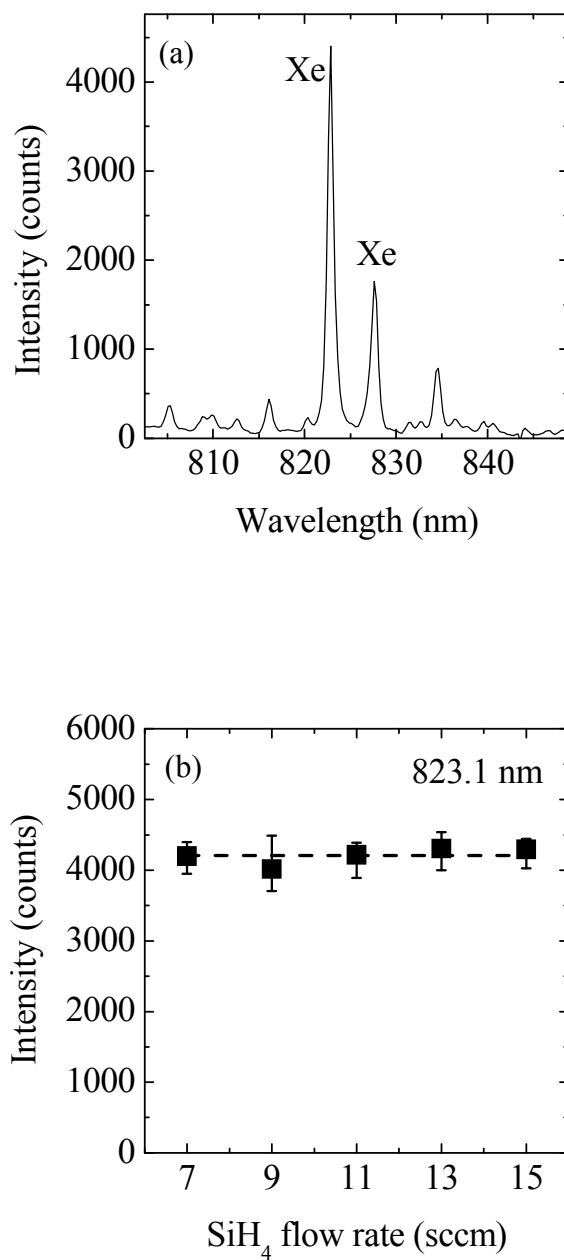


Fig. 4.5 (a) Optical emission spectrum at around 825 nm when a small amount (1 sccm) of Xe was added to the parent gases, (b) emission intensity at 823.1 nm as a function of SiH₄ flow rate. The dashed line is guide to the eye.

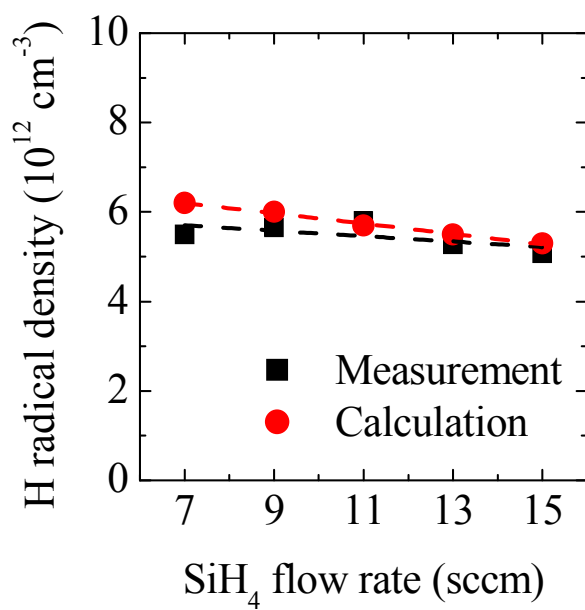


Fig. 4.6 Measured H radical density and the calculated H radical density as a function of SiH_4 flow rate. The dashed line is guide to the eye.

4.3.3 Measurement of SiH₃ radicals

Figure 4.7 shows typical cavity decay profiles with and without plasma. The decay profile with plasma was measured at 6 ms after the plasma ignition. The cavity-ring-down signals represent exponentially decreases with time. The cavity loss reflects absorption and scattering during multiple reflections between the mirrors. The cavity loss at laser wavelength of 220 nm reflects light-absorbing by SiH₃ radicals and light-scattering or light-absorbing by nano-particles that gradually grew with time after the plasma ignition. The cavity loss at 280 nm reflects light-scattering or light-absorbing by nano-particles because the absorption range of SiH₃ is from ~200 to ~260 nm.¹⁴ Therefore, we measured the cavity loss at the laser wavelength of 220 and 280 nm. Figure 4.8 shows time-evolution of the cavity loss after plasma ignition at 220 and 280 nm. The detection limit was determined by the standard deviation of the distribution of ring-down time in vacuum over 1000 shots of laser. At 2 ms, the cavity loss was observed only at the wavelength of 220 nm but not at 280 nm. Besides, at 8 ms, the cavity losses at both represented similar values. This indicated that the loss was mainly occurred by scattering originated from nano-particles growth. Therefore on the basis of results taken at 2 ms, we could estimate a density of SiH₃ radicals in SiH₄/H₂ plasma.

It has been reported that the cavity loss at the laser wavelength of 280 nm was observed after a few seconds at 133 Pa.¹⁴ Although the difference of pressure is only one order of magnitude, the growth speed of nano-particles is three orders of magnitude higher in the present conditions. The formation of nano-particles starts from the insertion reactions between short lifetime species SiH_x and SiH₄, and then the growth speed of nano-particles can be expressed as

$$\frac{dN_{\text{nano}}}{dt} \propto k_5 [k_4 n_e N(\text{SiH}_4)] N(\text{SiH}_4), \quad (4.8)$$

where N_{nano} is the density of nano-particles, and k_4 and k_5 are reaction rate constants for generation of $\text{SiH}_{x \leq 2}$ and for reactions between $\text{SiH}_{x \leq 2}$ and SiH_4 , respectively. The density of SiH_4 is proportional to the pressure; therefore, at least the growth speed of nano-particles becomes two orders of magnitude higher when the pressure is one orders of magnitude higher. Furthermore, the electron density probably increases with increase in the pressure and some of k_5 shows a pressure dependence.¹⁵ Consequently, there is the possibility that the growth speed of nano-particle is three orders of magnitude higher than that in the one order of magnitude lower pressure.

Figure 4.9 shows the density of SiH_3 radicals as a function of SiH_4 flow rate. The increase in SiH_3 radicals is due to the increase of feed gas SiH_4 and that the gas phase reaction of SiH_3 with SiH_4 is not significant.

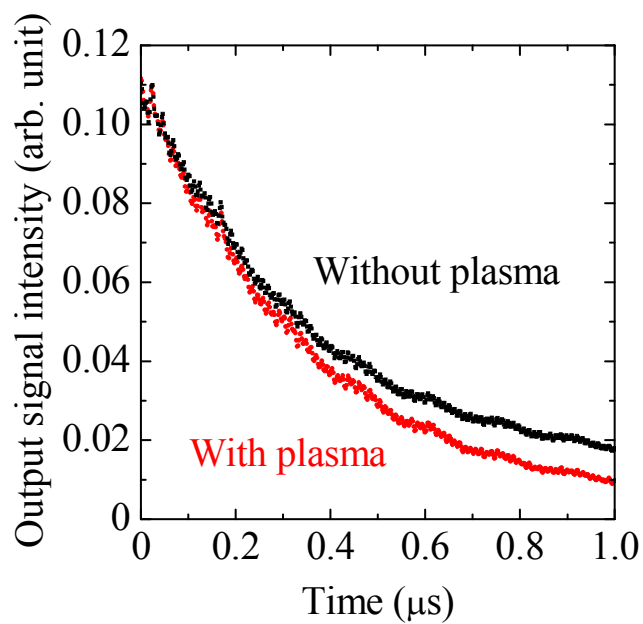


Fig. 4.7 Typical cavity decay profiles with and without plasma.

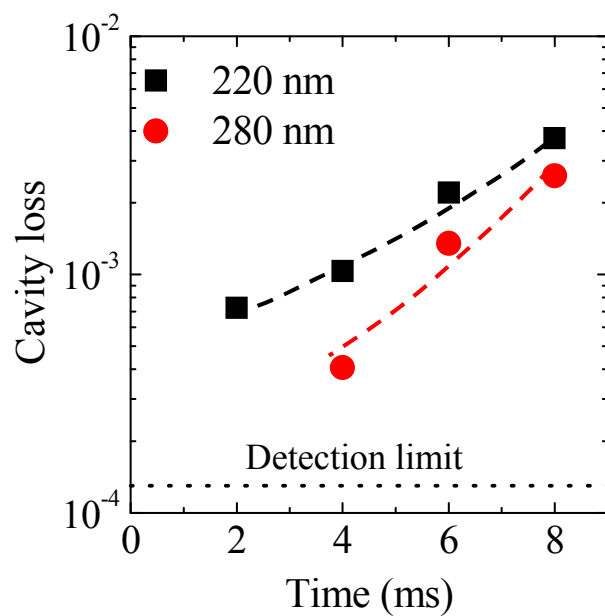


Fig. 4.8 Time-evolution of the cavity loss after plasma ignition at 220 and 280 nm. The dashed lines are guide to the eye.

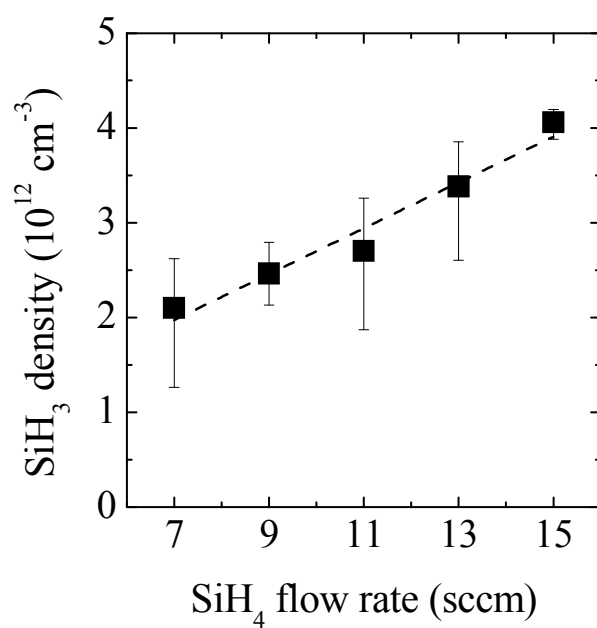


Fig. 4.9 The density of SiH₃ radicals as a function of SiH₄ flow rate. The dashed line is guide to the eye.

4.3.4 Film deposition characteristic

Raman spectra of Si films deposited at different SiH₄ flow rate ranging from 7 to 15 sccm are shown in Fig.4.10 (a). The spectra include three peaks corresponding to crystalline (520 cm⁻¹), defective crystalline (510 cm⁻¹), and amorphous (480 cm⁻¹) phases. The crystallinity factor was calculated using:

$$\phi_c = \frac{I_{520} + I_{510}}{I_{520} + I_{510} + I_{480}} \quad (4.9)$$

where I_k is the area under the Gaussian function centered at a Raman shift of k .¹⁶ As shown in Fig. 4.10 (b), the crystallinity factor decreased with increasing SiH₄ flow rate.

Figure 4.11 (a) shows XRD patterns of Si thin films deposited at different SiH₄ flow rate. The degree of <110> preferential orientation was evaluated from XRD patterns. $I(hkl)$ represents the integrated intensity of the (hkl) phase; therefore, the $I(220)/I(111)$ ratio indicates the degree of <110> preferential orientation. $I(220)/I(111)$ for the randomly oriented polycrystalline Si powder is 0.67. The $I(220)/I(111)$ ratio increased from 1.7 to 4.8 with increasing SiH₄ flow rate, followed by a decrease to 0.6 as shown in Fig. 4.11 (b).

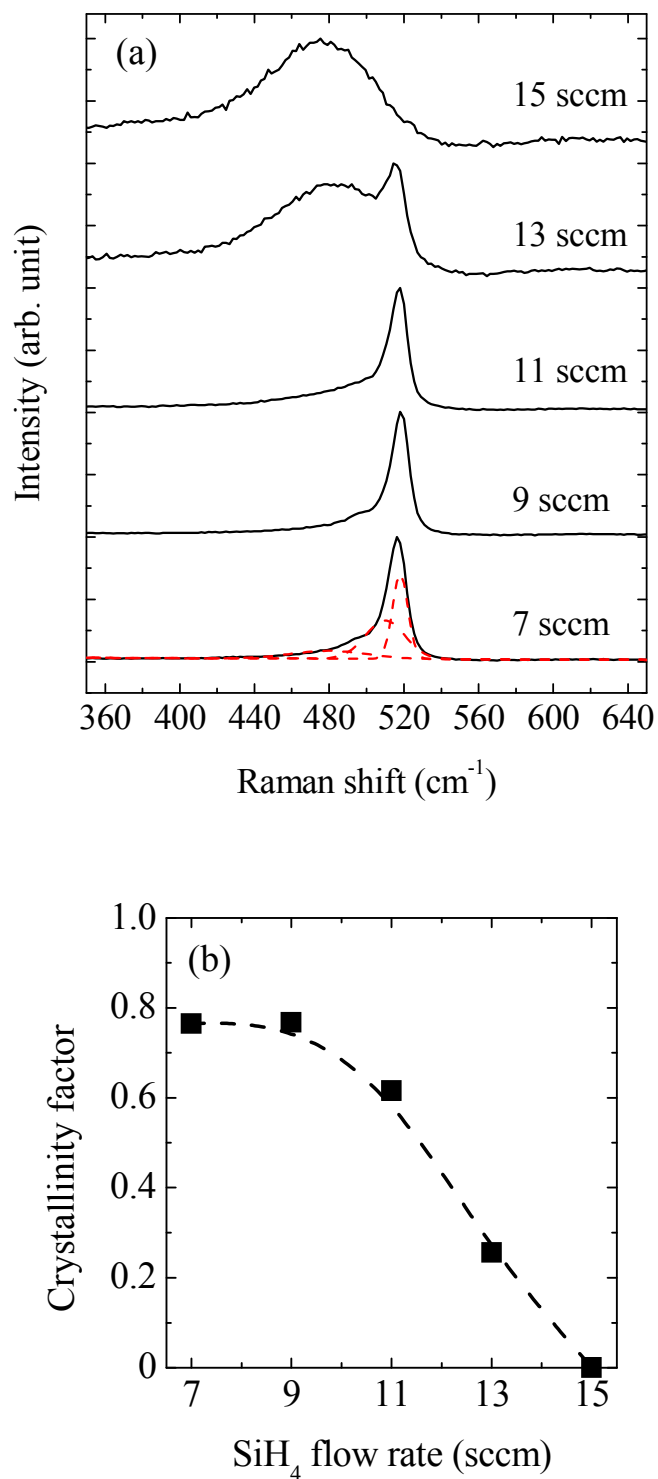


Fig. 4.10 (a) Raman spectra of Si thin films deposited at different SiH₄ flow rate. Dashed lines on spectrum of 7 sccm shows three peaks used for deconvolution. (b) Crystallinity factor as a function of SiH₄ flow rate. The dashed line is guide to the eye.

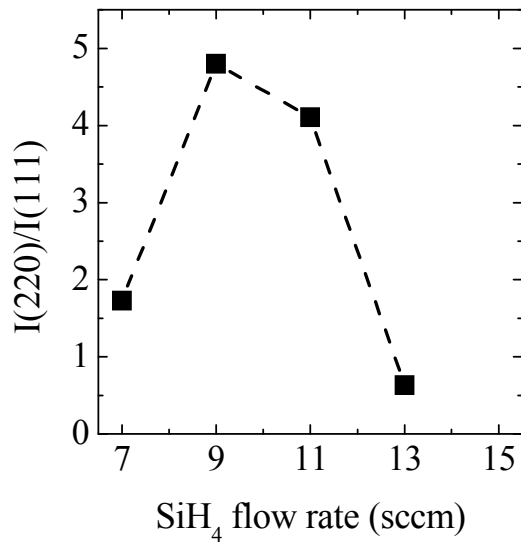
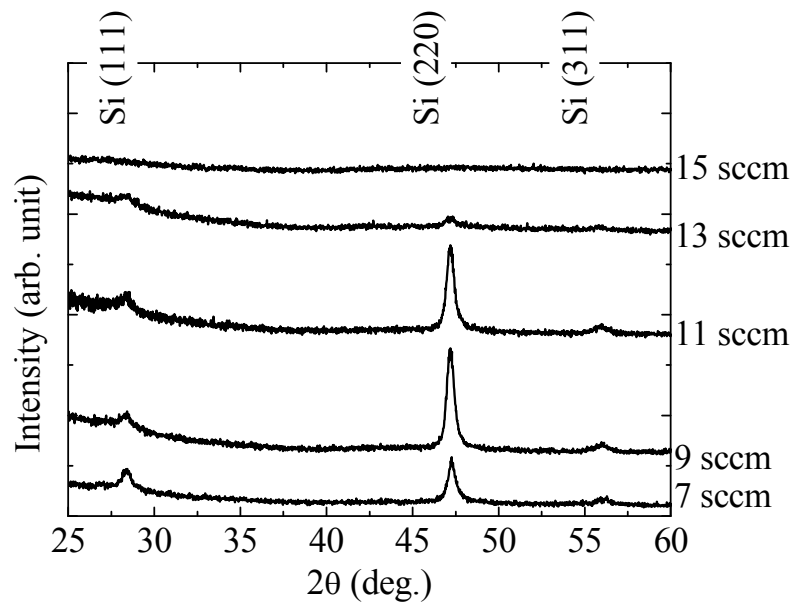


Fig. 4.11 (a) XRD patterns of Si thin films deposited at different SiH_4 flow rate (b) Ratio of the integrated intensity of the (220) and (111) as a function of SiH_4 flow rate. The dashed line is guide to the eye.

4.3.5 Relation between flux of radicals and film deposited property

Based on the results of preceding sections, the relation between the important film properties of $\mu\text{c-Si:H}$ and the fluxes of H radicals and film precursors will be discussed below.

Figure 4.12 shows the deposition rate and the flux of deposited precursor as a function of the SiH_4 flow rate. The deposition rate increased linearly with the SiH_4 flow rate, which also supports the depletion of SiH_4 . The flux of deposited precursor Γ_{P} , is given by:

$$\Gamma_{\text{P}} = \frac{R_{\text{d}}\rho}{m_{\text{Si}}}, \quad (4.10)$$

where R_{d} is the deposition rate, ρ is the film density ($\rho=2.18 \text{ g cm}^{-3}$),¹⁷ and m_{Si} is the atomic mass of silicon ($m_{\text{Si}}=4.69 \times 10^{-23} \text{ g}$).

Figure 4.13(a) shows that ϕ_{C} increased with $\Gamma_{\text{H}}/\Gamma_{\text{P}}$. The I(220)/I(111) ratio increased from 0.6 to 4.8 with $\Gamma_{\text{H}}/\Gamma_{\text{P}}$, followed by a decrease to 1.7. Si films deposited at $\Gamma_{\text{H}}/\Gamma_{\text{P}}$ of 65–80 exhibited strong $\langle 110 \rangle$ preferential orientation as shown in Fig. 4.13 (b). The etch rate of Si by H radicals is known to be dependent on the orientation; the etch rate of the (111) facet is smaller than those of other facets; therefore, at high $\Gamma_{\text{H}}/\Gamma_{\text{P}}$ I(220)/I(111) becomes small.¹⁸ In addition, it has been reported that the species of deposition radicals may influence determination of the growing facets.¹⁹ The ratio of deposition radicals would presumably be changed with variation of the SiH_4 flow rate. The defect density N_{D} was almost constant at $1.0 \times 10^{16} \text{ cm}^{-3}$, which is sufficiently low for device-applicable film quality. $\langle 110 \rangle$ -oriented $\mu\text{c-Si:H}$ with ϕ_{C} of approximately 0.5–0.6, or near the phase transition region from a-Si:H to $\mu\text{c-Si:H}$, is generally suitable for the i-layer of a solar cell.²⁰ Therefore, the critical $\Gamma_{\text{H}}/\Gamma_{\text{P}}$ to obtain film properties suitable for solar cell devices is so important and it was determined to be approximately 65–70 by this research.

Moreover, the ratio of SiH₃ radicals in the flux of film precursors was estimated. The flux of SiH₃ radicals deposited as films was calculated assuming the sticking probability of 0.09 (Ref. ²¹) and temperature of 473 K and using following equation;

$$\Gamma_{\text{SiH}_3} = \frac{s}{4} n_{\text{SiH}_3} \sqrt{\frac{8k_{\text{B}}T_{\text{SiH}_3}}{\pi m}}, \quad (4.11)$$

where s is sticking probability of SiH₃. Figure 4.14 shows the flux of SiH₃ radicals deposited as films as a function of SiH₄ flow rate. The ratio of SiH₃ radicals in the flux of film precursors was estimated to be 45%. Actually, the flux of SiH₃ radicals deposited as films is more accurately given by

$$\Gamma_{\text{SiH}_3} = \frac{1}{4} \frac{s}{1-\alpha} n'_{\text{SiH}_3} \sqrt{\frac{8k_{\text{B}}T_{\text{SiH}_3}}{\pi m}}, \quad (4.12)$$

where α is the surface loss probability of SiH₃ radicals, and n'_{SiH_3} is the density of SiH₃ radicals at the surface of the substrate. However, the spatial distribution of SiH₃ radicals cannot be measured in the present work, therefore the flux was estimated from Eq. (4.11). The surface loss probability of SiH₃ radicals has been reported to be ca. 0.5 in the case of $\mu\text{c-Si:H}$ at the substrate temperature of around 200°C.¹ From Eq. (4.12) and the surface loss probability of 0.5, a maximum possible flux can be estimated to be 1.3 times higher than the flux estimated from Eq. (4.11) because n'_{SiH_3} should be lower than n_{SiH_3} . A maximum possible ratio of SiH₃ radicals in the flux of film precursors is 59%; it is concluded that the film precursors is not only SiH₃ radicals. The results and considerations indicate that high order radicals Si_xH_y seems to be predominant precursors under the relatively higher pressure conditions.

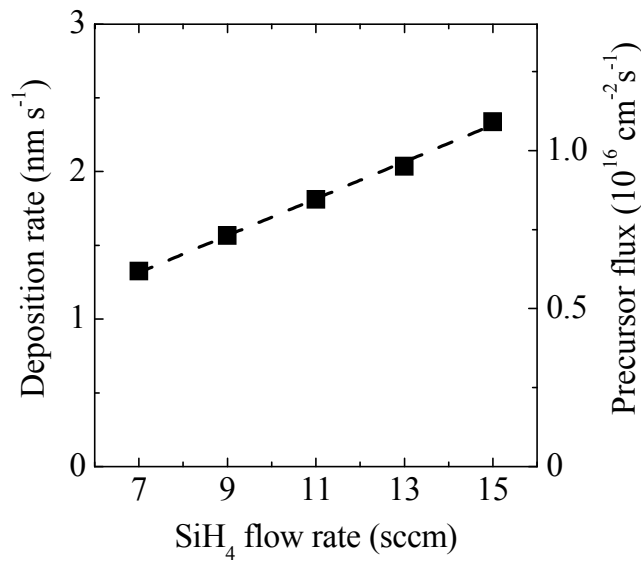


Fig. 4.12 Deposition rate and the flux of precursor deposited on the film as a function of the SiH₄ flow rate. The dashed line is guide to the eye.

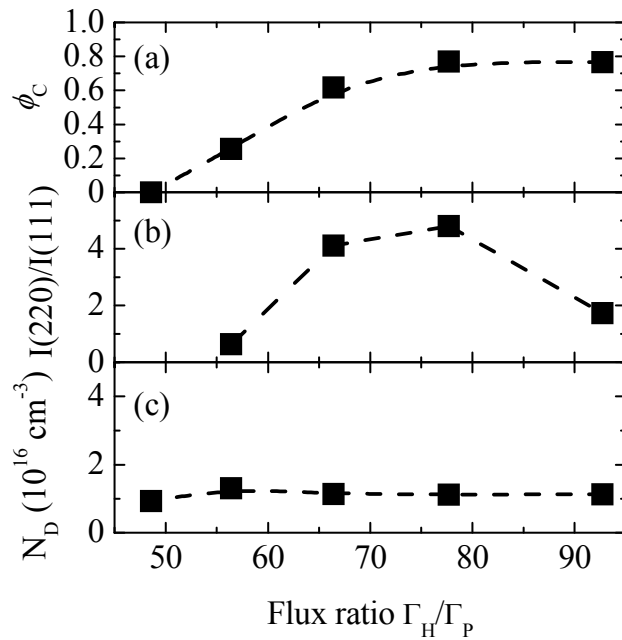


Fig. 4.13 Film properties interpreted in terms of the flux ratio Γ_H/Γ_P . Dashed lines are guide to the eye.

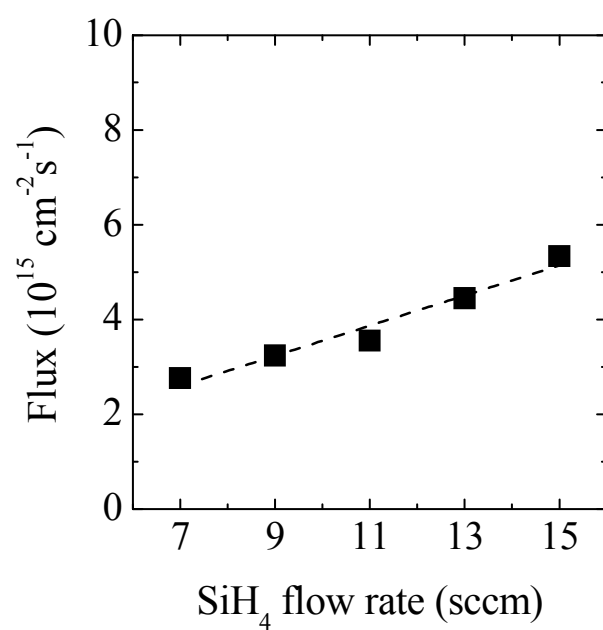


Fig. 4.14 Flux of SiH₃ radicals deposited as thin films. The dashed line is guide to the eye.

4.4 Conclusion

In conclusion, the flux ratio of H radicals to precursors that deposited as a film in SiH₄/H₂ plasma was investigated using tunable VUVLAS. The absolute density of H radicals was $5.5 \times 10^{12} \text{ cm}^{-3}$ and the translational temperature was around 770 K. The behavior of the calculated H radical density from rate equations approximately agrees with that of measured H radical density. The flux of H radicals was estimated to be $5.7 \times 10^{17} \text{ cm}^{-2} \text{ s}^{-1}$ from the measured H radical density. The flux of precursor deposited as a film was estimated to be in the order of $10^{15} - 10^{16} \text{ cm}^{-2} \text{ s}^{-1}$. The critical flux ratio to obtain film properties suitable for the i-layer of a solar cell was found to be approximately 65–70. Moreover, from the CRDS measurement, the ratio of SiH₃ radicals in the flux of film precursors was estimated to be 45%, and the growth speed of nano-particles is significantly-fast. These results indicate that the range of the flux ratio of H radicals to film precursors to obtain suitable film properties is very narrow and the 65–70 times higher flux of H radicals than film precursors is necessary. Therefore, achieving the sufficient H radical density is crucial issue for the high-rate deposition of $\mu\text{c-Si:H}$. In the case of the relatively higher pressure condition, not only SiH₃ radicals but also high order radicals seem to be predominant precursors, and then the behaviors of high order radicals are important for further understanding the deposition process.

4.5 References

- ¹ A. Matsuda, *J. Non-Cryst. Solids* **338-340**, 1 (2004).
- ² C. C. Tsai, G. B. Anderson, R. Thompson, and B. Wacker, *J. Non-Cryst. Solids* **114**, 151 (1989).
- ³ F. Kaïl, A. Fontcuberta I Morral, A. Hadjadj, P. Roca I Cabarrocas, and A. Beorchia, *Philos. Mag.* **84**, 595 (2004).
- ⁴ K. Nakamura, K. Yoshino, S. Takeoka, and I. Shimizu, *Jpn. J. Appl. Phys.* **34**, 442 (1995).
- ⁵ O. Vetterl, F. Finger, R. Carius, P. Hapke, L. Houben, O. Kluth, A. Lambertz, A. Mück, B. Rech, and H. Wagner, *Sol. Energy Mater. Sol. Cells* **62**, 97 (2000).
- ⁶ G. Dingemans, M. N. van den Donker, D. Hrunski, A. Gordijn, W. M. M. Kessels, and M. C. M. van de Sanden, *Appl. Phys. Lett.* **93**, 111914 (2008).
- ⁷ S. Nunomura and M. Kondo, *J. Phys. D: Appl. Phys.* **42**, 185210 (2009).
- ⁸ D. Wagner, B. Dikmen, and H. F. Döbele, *Rev. Sci. Instrum.* **67**, 1800 (1996).
- ⁹ M. Fukawa, S. Suzuki, L. Guo, M. Kondo, and A. Matsuda, *Sol. Energy Mater. Sol. Cells* **66**, 217 (2001).
- ¹⁰ S. J. B. Corrigan, *J. Chem. Phys.* **43**, 4381 (1965).
- ¹¹ E. Meeks, *J. Vac. Sci. Technol. A* **16**, 544 (1998).
- ¹² J. Perrin, O. Leroy, and M. C. Bordage, *Contrib. Plasma Phys.* **36**, 3 (1996).
- ¹³ S. Takashima, M. Hori, T. Goto, and K. Yoneda, *J. Appl. Phys.* **89**, 4727 (2001).
- ¹⁴ T. Nagai, A. H. M. Smets, and M. Kondo, *Jpn. J. Appl. Phys.* **47**, 7032 (2008).
- ¹⁵ H. Nomura, K. Akimoto, A. Kono, and T. Goto, *J. Phys. D: Appl. Phys.* **28**, 1977 (1995).
- ¹⁶ C. Droz, E. Vallat-Sauvain, J. Bailat, L. Feitknecht, J. Meier, and A. Shah, *Sol. Energy Mater. Sol. Cells* **81**, 61 (2004).

Chapter 4

- ¹⁷ B. Strahm, A. A. Howling, L. Sansonnens, and C. Hollenstein, *Plasma Sources Sci. Technol.* **16**, 80 (2007).
- ¹⁸ M. Ishii, K. Nakashima, I. Tajima, and M. Yamamoto, *Jpn. J. Appl. Phys.* **31**, 4422 (1992).
- ¹⁹ K. Saito and M. Kondo, *Physica Status Solidi (a)* **207**, 535 (2010).
- ²⁰ T. Matsui, M. Tsukiji, H. Saika, T. Toyama, and H. Okamoto, *Jpn. J. Appl. Phys.* **41**, 20 (2002).
- ²¹ A. Matsuda, K. Nomoto, Y. Takeuchi, A. Suzuki, A. Yuuki, and J. Perrin, *Surf. Sci.* **227**, 50 (1990).

Chapter 5 Fabrication of Microcrystalline Silicon Thin Film by H Radical-Injection Plasma

5.1 Introduction

Hydrogenated microcrystalline silicon ($\mu\text{c-Si:H}$) thin film is a promising material for the bottom cell of a tandem solar cell, because it can absorb higher wavelength light towards the infrared region of the solar spectrum and has excellent stability against light soaking compared to amorphous silicon (a-Si:H) thin films, which are used for the top cell.¹⁻⁴

Low temperature plasma-enhanced chemical vapor deposition (PECVD) processes employing SiH_4/H_2 plasma are commonly used for the deposition of $\mu\text{c-Si:H}$ films. However, the optical transition of $\mu\text{c-Si:H}$ is indirect; therefore, film thicknesses greater than 2 μm are required for sufficient absorption of sunlight. Consequently, the high-rate growth of high-quality $\mu\text{c-Si:H}$ films is required to reduce the cost of solar cell fabrication.

H radicals are recognized as a key factor that influences the crystallinity of Si thin films. Sufficient supply of H radicals to a growing Si thin film surface induces crystallization. Some models have been proposed for the reaction of H radicals on a growing Si film surface. During Si thin film deposition, H radicals cover the growth surface and induce local heating by recombination to hydrogen molecules.^{4,5} These two events on the surface enhance surface diffusion of the film growth precursors, so that the precursors can find stable adsorption sites and make stable Si-Si bonds. H radicals etch weakly bonded Si atoms in the amorphous phase, which results in the reconstruction of a Si-Si bond network in H-rich subsurface regions.⁶⁻⁸ In Chapter 4, the behavior of H radicals in SiH_4/H_2 plasma has been investigated using a vacuum ultraviolet laser absorption spectroscopy (VUVLAS). The results in Chapter 4 have indicated that the

range of the flux ratio of H radicals to film precursors to obtain suitable film properties is very narrow, and that the 65–70 times higher flux of H radicals than film precursors is necessary. Therefore, achieving the sufficient H radical density is crucial issue for the high-rate deposition of $\mu\text{c-Si:H}$.

A growth rate of approximately 2 nm/s was reported using a capacitively coupled plasma (CCP) system with a high input power of very-high-frequency (VHF as power-source frequency), a high working pressure (ca. 1000 Pa), and a narrow electrode gap.^{9–11} The high pressure and the high input power of VHF-power source provide a high-electron density, which leads to the efficient generation of a film precursor. The high pressure also suppresses high ion energy which causes the formation of defect in films. In addition, the high electron density is effective to achieve SiH_4 depletion, even at a relatively high working pressure. SiH_4 depletion is useful for the survival of H radicals, because SiH_4 is a H radical scavenger.^{4,12,13}

The optoelectronic properties of $\mu\text{c-Si:H}$ films are degraded with an increase in the film growth rate (>2 nm/s),¹⁴ due to an increase in the density of dangling-bond defects in the film.^{12,15} A high depletion of SiH_4 causes an increase in the contribution of short-lifetime species such as SiH_2 , SiH , and Si during film growth. Short-lifetime species have high reactivity and adhere to the growing film surface without surface diffusion by insertion reactions into Si-H bonds. An increase in the contribution of short-lifetime species causes an increase in the number density of dangling-bond defects in the films. Moreover, further high-pressure has a problem on a mass production. Increasing pressure reduces electrode spacing between cathode and anode to produce stable plasma in the CCP reactor, causing non-uniform plasma production and non-uniform film growth.⁴ As shown in Chapter 4, the growth speed of nano-particles is significantly increased by the increase in the high pressure, which reduces the up-time of large-area plasma deposition systems. This is because a maintenance time becomes frequent to clean nano-particles in chambers.

In this study, H radical-injection (RI)-PECVD for the high-rate deposition of $\mu\text{c-Si:H}$ thin films. The RI-system enables the individual control of multiple species. The RI-PECVD system has a H_2 plasma as a radical source in addition to a deposition plasma (SiH_4/H_2 plasma); H radicals in the deposition plasma are increased by the injection from the radical source. Therefore, the RI-PECVD has a potential to fabricate $\mu\text{c-Si:H}$ films under low depletion of SiH_4 and to increase the deposition rate without increasing the pressure and the input power. In fact, the effect on the morphology and growth rate of carbon nanowalls (CNWs) has been demonstrated by controlling the H radical density in $\text{C}_2\text{F}_6/\text{H}_2$ CCP using an RI-system that employs inductively coupled plasma.^{16,17} Another RI-PECVD system was developed to achieve large area growth of CNWs with a reasonable growth rate using a surface wave microwave excited H_2 plasma as a radical source.^{18,19}

The plasma parameters and film-growth characteristics obtained using the PECVD system with and without the RI-system are compared in this study. The electron density, electron temperature, and H radical density were measured to evaluate the features of the RI-system. The crystallinity factor, preferential orientation, defect density, microstructure, and post-deposition oxidation of the resultant thin Si film were analyzed to evaluate and to discuss the effect of the RI-system.

5.2 Experimental details

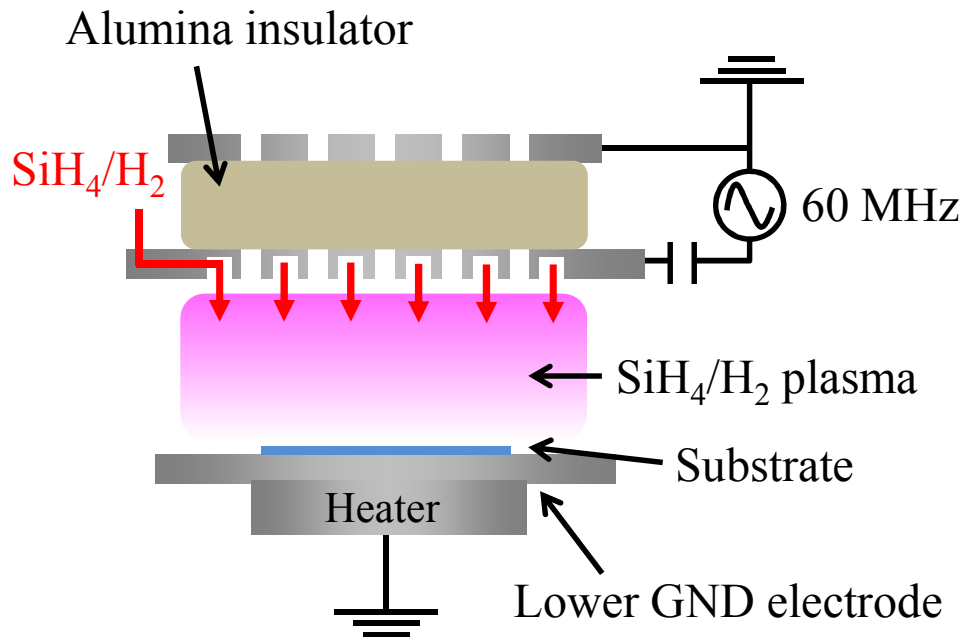
Figure 5.1 shows schematic illustrations of the PECVD reactors with (a) conventional capacitively coupled plasma (C-CCP) source and (b) CCP source with RI (RI-CCP). Both sources have a shower-head VHF electrode, to which 60 MHz VHF power was applied, and a lower grounded (GND) electrode. A hydrogen diluted silane (SiH_4/H_2) plasma was generated between these electrodes. In the case of C-CCP, H_2 gas was introduced through the VHF electrode together with SiH_4 gas and an alumina (Al_2O_3) insulator was placed between the upper GND and VHF electrodes. In the case of RI-CCP, the H_2 gas was introduced into the upper region through the upper GND electrode to generate the H_2 plasma between the upper GND and VHF electrodes. Then, the H_2 gas and H radicals generated in the H_2 plasma are supplied to the H_2 plasma. The distance between the VHF and lower GND electrodes was 10 mm, and that between the VHF and upper GND electrodes was 5 mm.

Three different substrates, glass (Corning EAGLE XGTM), quartz, and Si(100) were placed on the lower GND electrode. 1 μm thick Si thin films were deposited on these substrates. The crystallinity factor and preferential orientation of the Si thin films deposited on the glass substrates were then analyzed by Raman spectroscopy and X-ray diffraction (XRD). The defect density of the films deposited on quartz substrates was measured by electron spin resonance (ESR) spectroscopy. Post-deposition oxidation of films deposited on Si(100) substrates was evaluated by Fourier-transform infrared spectroscopy (FTIR). The microstructure of films was observed by transmission electron microscopy (TEM). For conductivity measurements, a comb electrode of Al, patterned as shown in Fig. 5.2, was deposited on the Si thin films by electron beam evaporation. Photo conductivity was measured under solar simulator (SERIC LTD. XL-03E50K *kai*) illumination (air mass 1.5 and 100 mW/cm^2).

Chapter 5

The electron density in the SiH_4/H_2 plasma region was measured using a 35 GHz microwave interferometer.²⁰ A multi-channel spectrometer was used to observe the optical emission intensity of the $\text{Si}^*(288 \text{ nm})$ and $\text{SiH}^*(414 \text{ nm})$ lines. The absolute density of H radicals was measured by vacuum ultraviolet laser absorption spectroscopy (VUVLAS).

(a) C-CCP



(b) RI-CCP

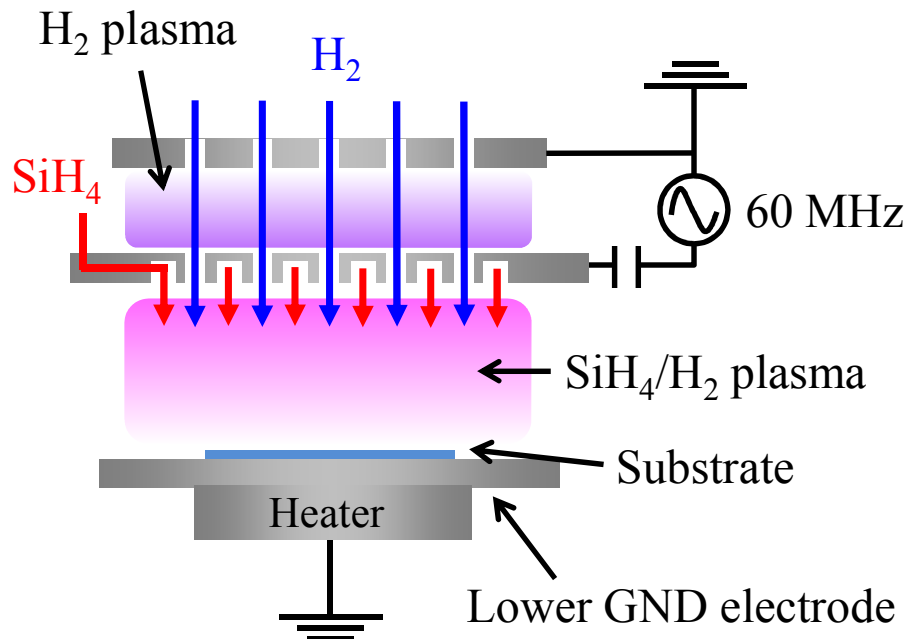


Fig. 5.1 Schematic illustrations of the PECVD reactors (a) conventional capacitively coupled plasma (C-CCP) source and (b) CCP source with RI (RI-CCP).

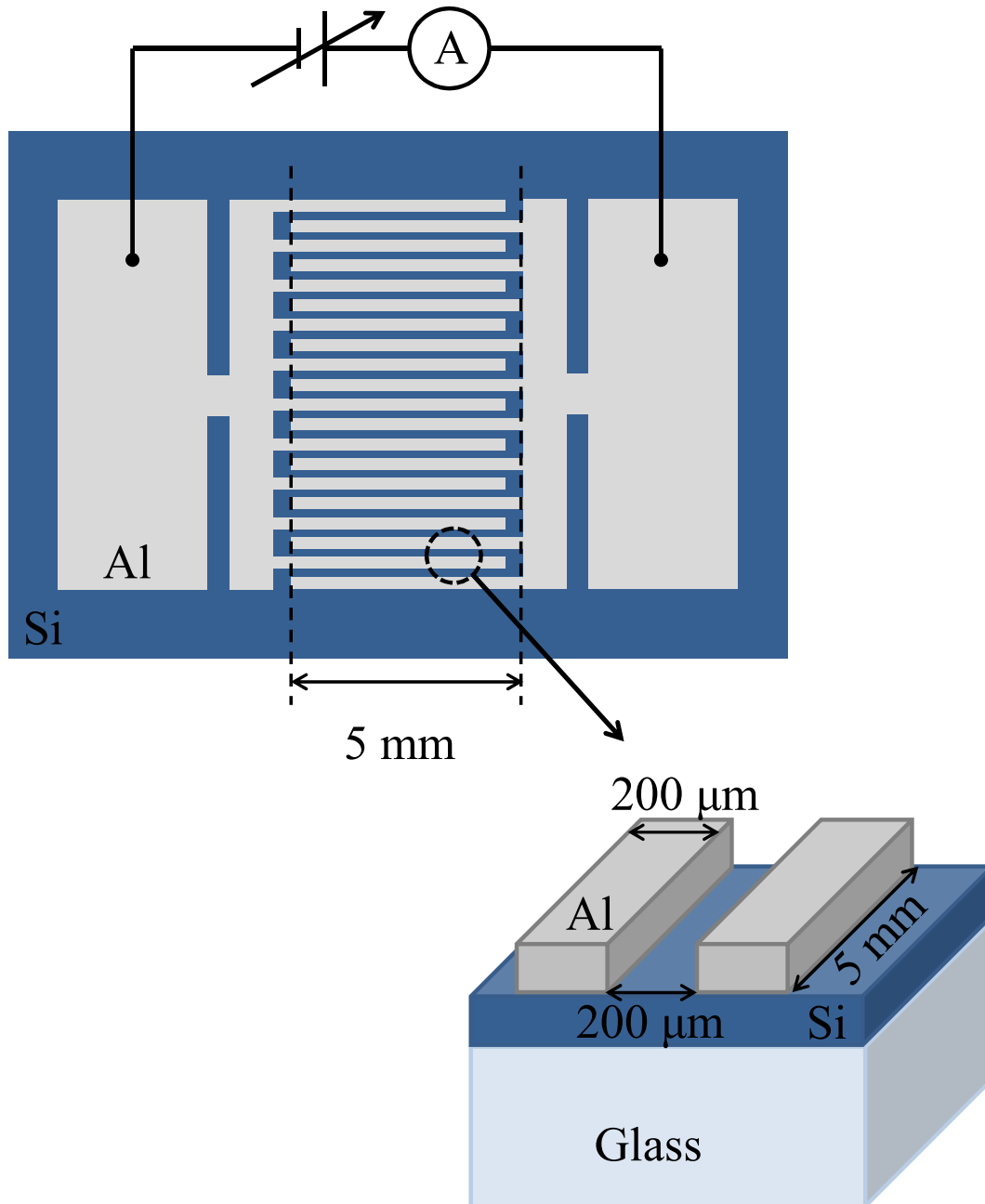


Fig. 5.2 Schematic illustration of the comb electrode of Al deposited on the Si thin films.

5.3 Results and discussion

5.3.1 Plasma diagnostics

Measurements of the electron density as a function of the VHF power in the SiH₄/H₂ plasma region were carried out for comparison of RI-CCP and C-CCP under the same plasma conditions. For RI-CCP, both the SiH₄/H₂ and H₂ plasmas are produced with one VHF power; therefore, the electron density should be different from that for C-CCP at the same VHF power. Figure 5.3 shows the electron density in the SiH₄/H₂ plasma for both C-CCP and RI-CCP as a function of the VHF power. The electron density increased from 4.7×10^{10} to $12.8 \times 10^{10} \text{ cm}^{-3}$ for C-CCP and from 2.0×10^{10} to $9.3 \times 10^{10} \text{ cm}^{-3}$ for RI-CCP with an increase in the VHF power from 200 to 700 W. The SiH₄/H₂ gas mixture ratio was 3% with a total gas flow rate of 1000 sccm, and the total pressure was kept at 1200 Pa. The densities for RI-CCP are lower (44–72%) than those for C-CCP at the same VHF power. Therefore, to evaluate the effect of the RI-system, at least it is necessary to compare RI-CCP and C-CCP at the same electron density.

SiH₄ and H₂ are dissociated by electron impact with threshold energies of 8.75 eV and 8.8 eV, respectively. Therefore, electrons in the high-energy tail region of the electron-energy distribution-function play an important role in the production of species such as SiH₃ and H radicals. The electron temperature was estimated by optical emission spectroscopy. It has been reported that the Si* and SiH* emissive species are produced through the one-electron-process of SiH₄ molecules with energies of more than 10.35–11.5 and 10.33–10.5 eV, respectively.²¹ Therefore, the optical emission intensity ratio [Si*/SiH*] gives information on the slope of the high-energy tail region of the electron-energy distribution-function for a plasma and can be used as a estimation of behavior of the electron temperature.²²

The optical emission intensity ratios $[Si^*/SiH^*]$ for C-CCP and RI-CCP were measured to compare the electron temperatures. Figure 5.4 shows the optical emission intensity ratios $[Si^*/SiH^*]$ in the SiH_4/H_2 plasma region as a function of the VHF power. Both emission intensity ratios for C-CCP and RI-CCP were almost constant at 0.5. These measurements indicate that the electron temperatures in the SiH_4/H_2 plasma regions of C-CCP and RI-CCP are almost the same, whereas the electron densities are different. Therefore, it is reasonable to compare those two plasma sources at the same electron density under a constant electron temperature.

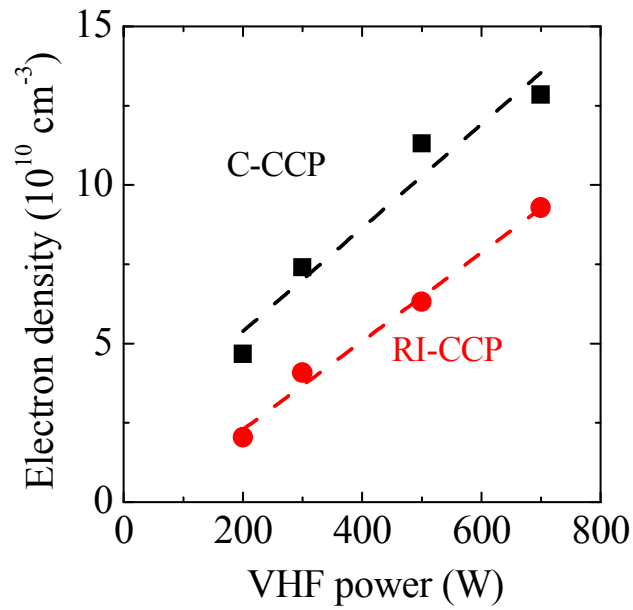


Fig. 5.3 Electron density in the SiH_4/H_2 plasma regions as a function of VHF power. The dashed lines are guide to the eye.

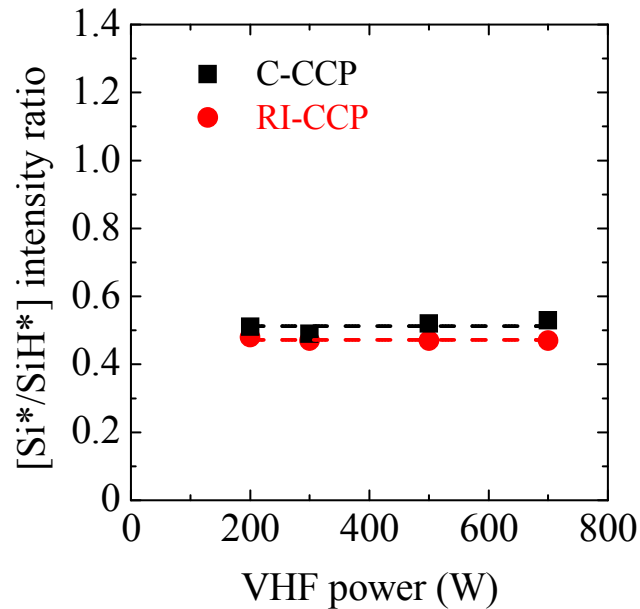


Fig. 5.4 Optical emission intensity ratio $[\text{Si}^*/\text{SiH}^*]$ in the SiH_4/H_2 plasma regions as a function of VHF power. The dashed lines are guide to the eye.

H radicals play an important role in the formation of Si thin films. The absolute density of H radical in the SiH₄/H₂ plasma was measured using the VUVLAS technique to evaluate the effect of the RI-system on the H radical density. Absorption measurements were conducted with variation of the VHF power. Figure 5.5 shows the absolute density of H radical in the SiH₄/H₂ plasma regions of C-CCP and RI-CCP as a function of the electron density. The density of H radicals increased from 4.8×10^{12} to 8.2×10^{12} cm⁻³ for C-CCP and from 5.5×10^{12} to 8.3×10^{12} cm⁻³ for RI-CCP with an increase in the electron density. The density of H radicals with RI-CCP is ca. 1.4 times higher than that with C-CCP compared at the same electron density, because H radicals were supplied from the H₂ plasma in the case of RI-CCP. Therefore, the RI-system enables an increase in the H radical density at the same electron density and temperature.

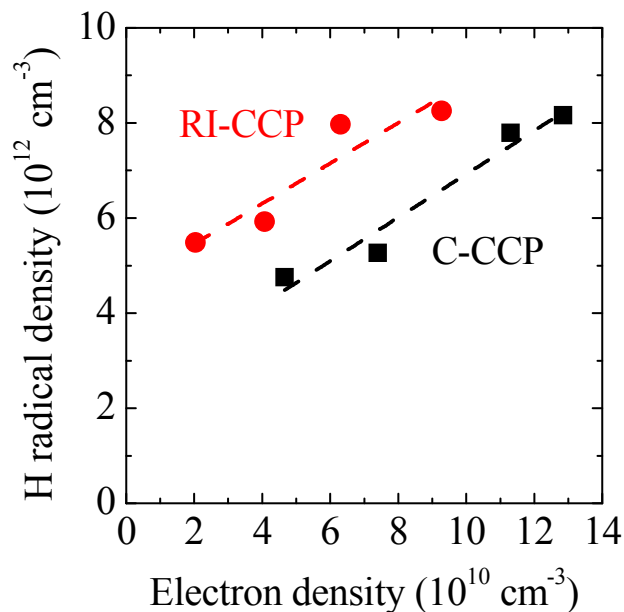


Fig. 5.5 Absolute density of H radical in the SiH₄/H₂ plasma regions as a function of electron density. The dashed lines are guide to the eye.

5.3.2 Film deposition characteristics

Figure 5.6 shows deposition rates for C-CCP and RI-CCP as a function of the electron density. The substrate temperature was 373 K. The deposition rate for C-CCP increased slightly from 2.8 to 3.2 nm/s with increasing electron density, and then became saturated. Similarly, the deposition rate for RI-CCP increased from 2.0 to 3.0 nm/s with increasing electron density and became saturated. The deposition rate with both plasmas satisfies the production level required for the fabrication of solar cell devices.

The increase in the deposition rate is due to enhanced dissociation of SiH_4 by the increase in the electron density. Saturation of the deposition rate indicates that the silane species is depleted. The deposition rates for both plasmas were equal at the same electron density. These results indicate that only the production of the film growth precursors is strongly dependent on the plasma density.

In contrast, the etching effect of H radicals is ignorable. Si etch yield of H radicals is enough low as 0.01,²³ and H radical flux is $10^{17} \text{ cm}^{-2} \text{ s}^{-1}$ from the results of VUVLAS measurement. Compared with the estimated etching rate of 0.1 nm/s here, the deposition rates of more than 1 nm/s were one order higher in magnitude. Therefore, the H etching effect has no significant contribution on deposition even though the H radical density was 1.4 times higher for the RI-CCP than that for C-CCP.

Figure 5.7 shows the crystallinity factors ϕ_C of Si thin films deposited by C-CCP and RI-CCP as a function of the electron density. The crystallinity factor is determined from

$$\phi_C = \frac{I_{520} + I_{510}}{I_{520} + I_{510} + I_{480}}, \quad (5.1)$$

where I_k is the area under Gaussian centered at k and k is the Raman shift.²⁴ ϕ_C for C-CCP increased from 0 to 0.68 with increasing electron density from 4.7×10^{10} to

$7.4 \times 10^{10} \text{ cm}^{-3}$, followed by a slight decrease to 0.60 at a density of $12.8 \times 10^{10} \text{ cm}^{-3}$. ϕ_C for RI-CCP increased from 0.20 to 0.78 with increasing electron density from 2.0×10^{10} to $6.3 \times 10^{10} \text{ cm}^{-3}$ and decreased to 0.70 at a density of $9.3 \times 10^{10} \text{ cm}^{-3}$. H radicals enhance the crystallinity of Si thin films, and the generation of H radicals by dissociation of feed gases increases with increasing electron density. Furthermore, a loss of H radicals, which is due to the main reaction between H and SiH_4 , decreases with increasing electron density due to the depletion of SiH_4 . The H radical density increased with increasing electron density, as shown in Fig.5.5. However, with increasing VHF power, ion bombardment also increased, which causes a decrease in the crystallinity.⁴ The decrease in crystallinity is probably due to the increase in ion bombardment and/or the depletion of SiH_4 , which increases the short-lifetime of SiH_2 , SiH , and Si species. The ϕ_C values for RI-CCP and C-CCP are compared in Fig. 5.7, which indicate that crystallization was enhanced for RI-CCP. In particular, crystallization occurs with RI-CCP even at lower electron densities where no crystallization occurs for C-CCP. These results indicate that crystallization can occur under low depletion of SiH_4 for RI-CCP, due to the higher H radical densities in RI-CCP than C-CCP, as shown in Fig. 5.5.

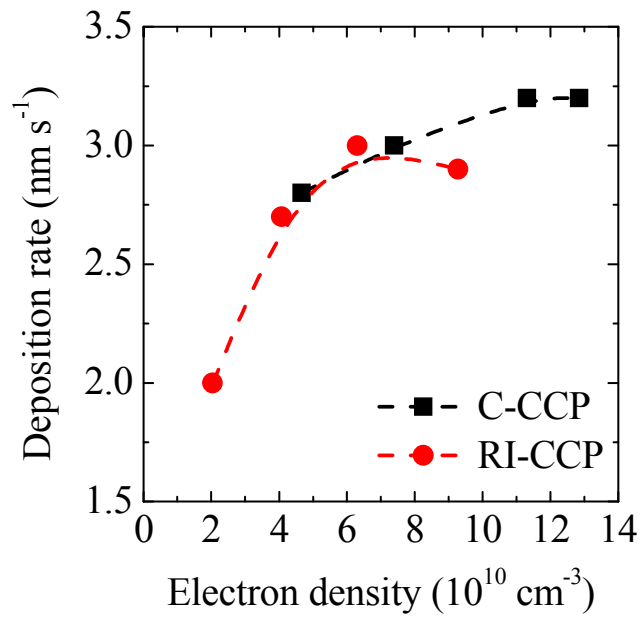


Fig. 5.6 Deposition rate as a function of electron density. The dashed lines are guide to the eye.

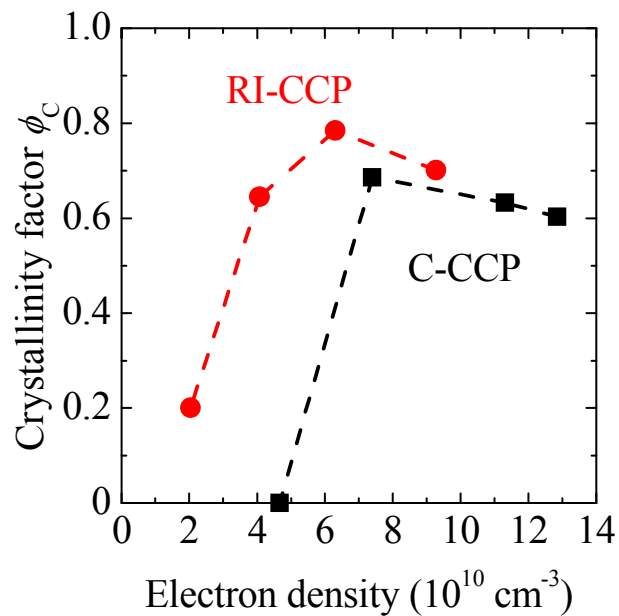


Fig. 5.7 Crystallinity factors for Si thin films deposited by C-CCP and RI-CCP as a function of the electron density, determined from Raman spectroscopy. The dashed lines are guide to the eye.

The degree of $\langle 110 \rangle$ preferential orientation, $I(220)/I(111)$, where $I(hkl)$ denotes the integrated intensity of the (hkl) phase in the XRD pattern is shown in Fig. 5.8. The dotted line represents $I(220)/I(111)$ for randomly oriented polycrystalline Si powder. Figure 5.8 shows that the Si thin film grown at an electron density of $6.3 \times 10^{10} \text{ cm}^{-3}$ by RI-CCP has weak $\langle 110 \rangle$ preferential orientation. The mechanism to determine the crystalline orientation is not yet completely understood. However, it has been reported that the composition of deposition radicals (SiH_3 and polysilane radicals) may play an important role in the determination of the growth facets.^{25,26} For RI-CCP, crystallization occurs under low depletion of SiH_4 . Therefore, the ratio of SiH_3 radicals to polysilane radicals may be different from that for C-CCP.

Figure 5.9 shows the defect densities of Si thin films deposited by C-CCP and RI-CCP as a function of the electron density. The defect density increased from 4.6×10^{16} to $8.7 \times 10^{17} \text{ cm}^{-3}$ for C-CCP and from 5.1×10^{16} to $2.5 \times 10^{17} \text{ cm}^{-3}$ for RI-CCP with increasing electron density. It is supposed that the short-lifetime species increased with increasing electron density, because SiH_4 , which acts as the scavenger of such species, was depleted when the electron density was high. In addition, the effect of ion bombardment on the film growth possibly increased with an increase in the electron density. Ion bombardment is one of the causes for the generation of dangling-bond defects. This indicates that RI-CCP enables to deposit the crystallized Si films with low defect densities, because sufficient H radicals can be obtained even under low electron density which leads to low depletion of SiH_4 and less ion bombardment.

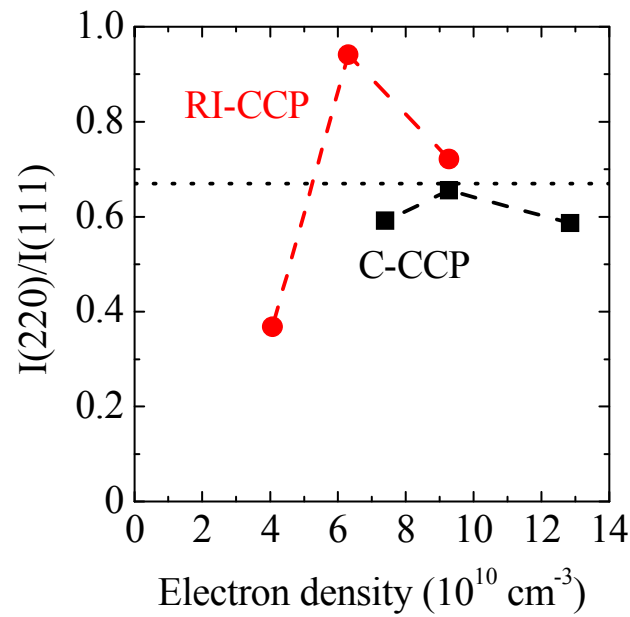


Fig. 5.8 Degree of $\langle 110 \rangle$ preferential orientation $I(220)/I(111)$ for Si thin films deposited with C-CCP and RI-CCP as a function of the electron density. The dashed lines are guide to the eye.

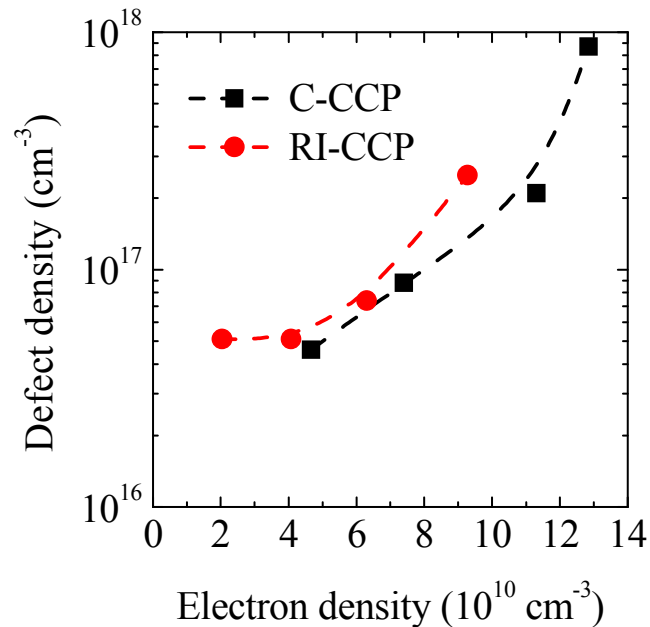


Fig. 5.9 Defect densities of Si thin films deposited by C-CCP and RI-CCP as a function of the electron density. The dashed lines are guide to the eye.

The microstructural characteristics of Si thin films deposited with C-CCP and RI-CCP were investigated. Bright-field images of cross-sectional samples for the films deposited by C-CCP and RI-CCP at 300 W are shown in Fig. 5.10. Dark regions and bright regions correspond to crystallites and voids, respectively.²⁷ The crystallinity factors of these samples are similar around 0.7, as shown in Fig. 5.7; however, the microstructures appear to be much different. The microstructure of the film deposited with RI-CCP near the film-substrate interface is quite different from that deposited with C-CCP and columnar structure was observed. This is probably due to crystallization occurring near the film-substrate interface. For RI-CCP, crystallization occurs under a lower electron density or lower ion bombardment than for C-CCP. High ion bombardment prevents nucleation at the initial stage.²⁸ Therefore, crystalline grains are present near the film-substrate interface in the case of RI-CCP.

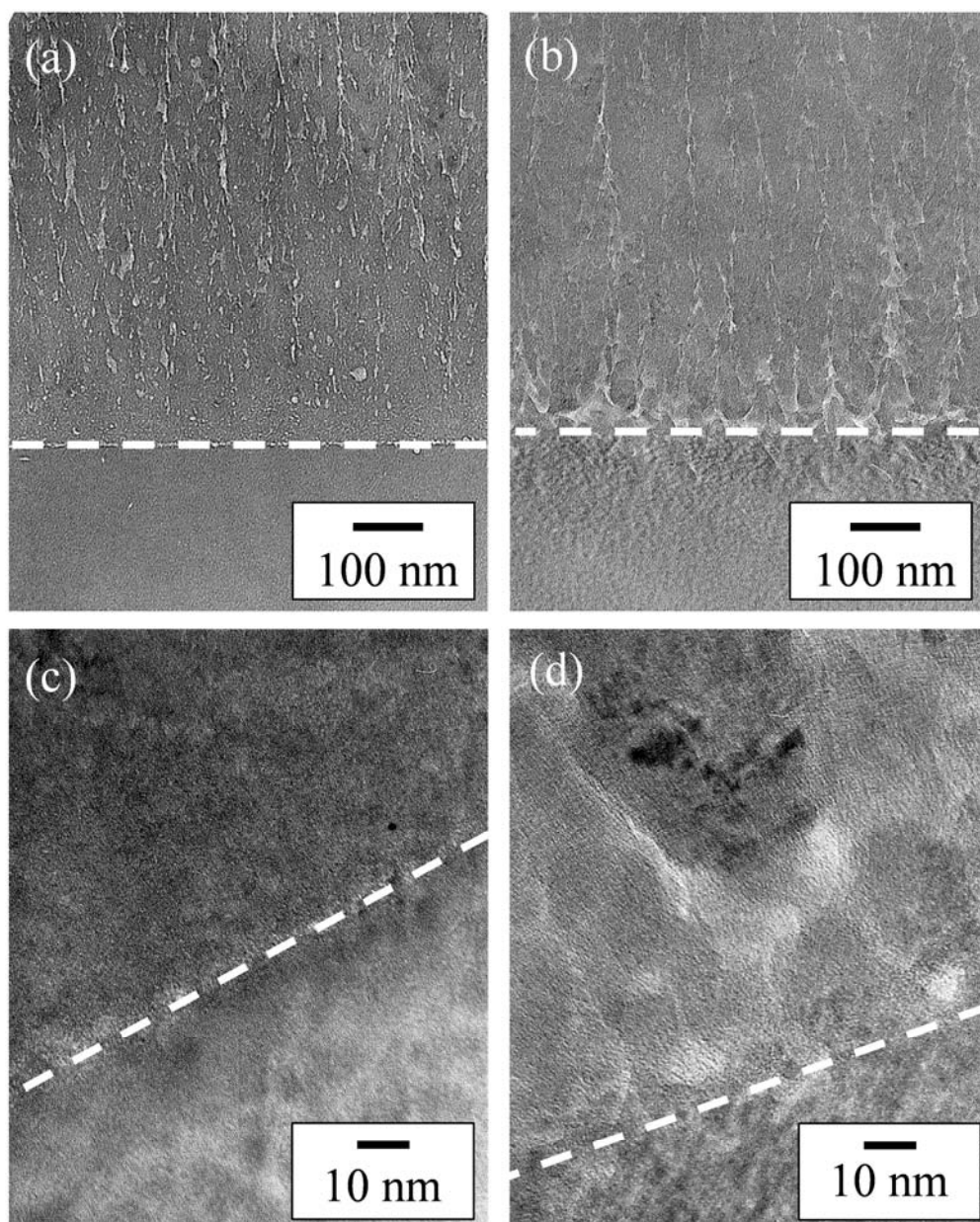


Fig. 5.10 Bright-field images of cross-sectional films deposited with (a),(c) C-CCP at 300 W (electron density: $7.4 \times 10^{10} \text{ cm}^{-3}$) and (b),(d) RI-CCP at 300 W (electron density: $4.1 \times 10^{10} \text{ cm}^{-3}$). White dashed lines represent the film-substrate interfaces.

Figure 5.11 shows FTIR spectra in the range of 800–1250 cm^{-1} for Si thin films deposited by C-CCP and RI-CCP at 300 W measured 16 days after deposition. The absorption bands at 840–890 cm^{-1} are attributed to the dihydride bending modes and those at 950–1200 cm^{-1} are attributed to the Si–O–Si stretching modes. The increase in the Si–O–Si stretching modes shows that the Si thin films are oxidized during exposure to the ambient air. The intensities of the Si–O–Si stretching modes for the Si thin film deposited with C-CCP increased more than those with RI-CCP in 16 days after deposition. Post-deposition oxidation occurs in voids and cracks connected to the film surface. There are possibly many voids in the film deposited with C-CCP, which is due to higher ion bombardment.²⁹ Thus, RI-CCP is more effective to avoid post-deposition oxidation.

Figure 5.12 shows deposition rate and crystallinity factor as a function of SiH_4 flow rate at VHF power of 400 W and pressure of 1200 Pa. Deposition rates for both C-CCP and RI-CCP increased with increasing SiH_4 flow rate, however the crystallized films can be obtained at higher SiH_4 flow rate using RI-CCP. It is due to that H radical density was increased by RI-system, therefore crystallization occurred at higher SiH_4 flow rate with RI-CCP. From this result, it was demonstrated that RI-CCP is useful for increase in the deposition rate with keeping the crystallinity factor.

Figure 5.13 shows the dark conductivity σ_{dark} , the photo conductivity σ_{photo} , and the photosensitivity $\sigma_{\text{photo}}/\sigma_{\text{dark}}$ of Si thin films deposited by RI-CCP as a function of ϕ_{C} . σ_{dark} and σ_{photo} increased and $\sigma_{\text{photo}}/\sigma_{\text{dark}}$ decreased with increasing ϕ_{C} ; this behavior is typical in Si thin films deposited by PECVD. In addition, the $\sigma_{\text{photo}}/\sigma_{\text{dark}}$ of the order of 10^2 seems to be high enough to apply the $\mu\text{c-Si:H}$ films to solar cells.³⁰

Crystallization was realized under a low electron density or low depletion of SiH_4 with RI-CCP, due to a sufficient H radicals supplied by the RI-system. The effect of the RI-system on the increase in H radicals was confirmed from VUVLAS measurements. Only the Si thin film deposited with RI-CCP had weak $\langle 110 \rangle$ preferential

orientation. It is necessary to measure deposition radicals to investigate the mechanism of $\langle 110 \rangle$ preferential orientation. $\mu\text{c-Si:H}$ films with low defect densities ($5.1 \times 10^{16} \text{ cm}^{-3}$) and low post-deposition oxidation can be achieved using RI-CCP, due to less short-lifetime species and less ion bombardment. RI-CCP can deposit the $\mu\text{c-Si:H}$ film at high deposition rate. $\mu\text{c-Si:H}$ films deposited by RI-CCP have good photosensitivity of the order of 10^2 . Thus, RI-CCP has a high possibility to realize high-quality $\mu\text{c-Si:H}$ films for the fabrication of solar cell devices with high deposition rate.

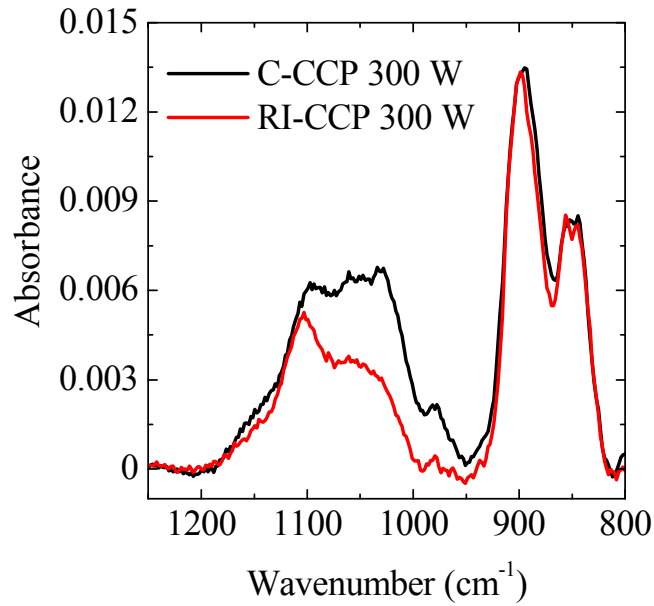


Fig. 5.11 FTIR spectra in the range of 800-1250 cm^{-1} for Si thin films deposited by C-CCP and RI-CCP at 300 W, measured in 16 days after deposition.

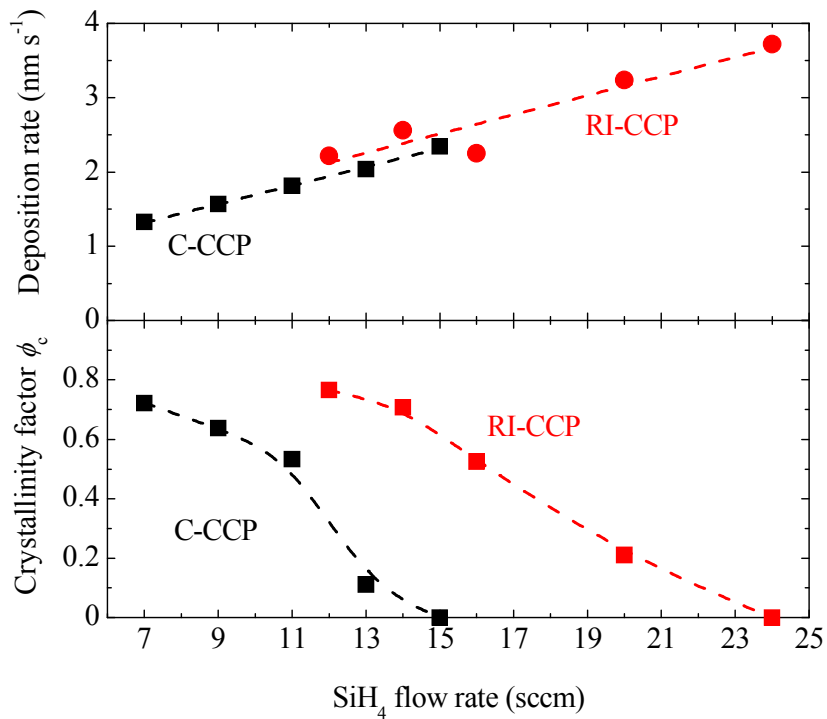


Fig. 5.12 Deposition rate and crystallinity factor as a function of SiH_4 flow rate. The dashed lines are guide to the eye.

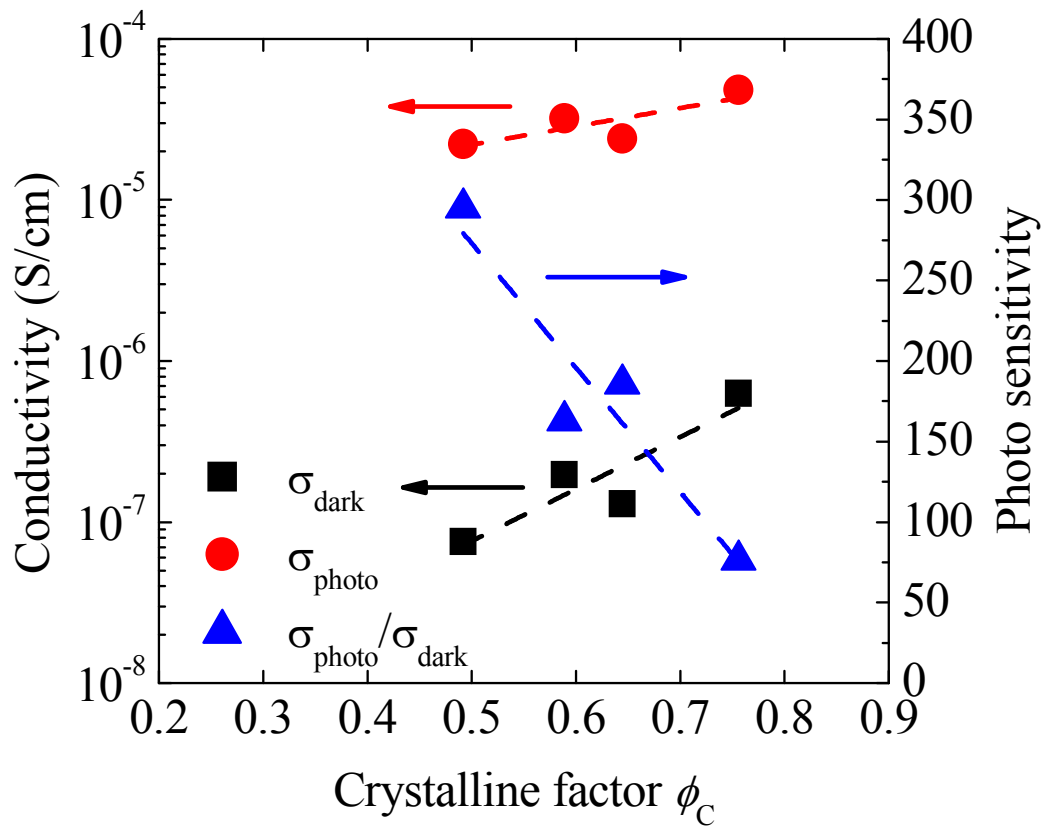


Fig. 5.13 Dark conductivity σ_{dark} , photo conductivity σ_{photo} , and photosensitivity $\sigma_{\text{photo}}/\sigma_{\text{dark}}$ of Si thin films deposited by RI-CCP as a function of crystalline factor ϕ_C .

5.4 Conclusion

PECVD at 60 MHz with a RI-system for the fabrication of Si thin films for solar cell devices was proposed to achieve selective enhancement of the H radical densities for crystallization of the films under low depletion of SiH₄. The plasma parameters and film growth characteristics of RI-CCP were compared with C-CCP. The electron density and temperature were measured using a microwave interferometer and by optical emission spectroscopy, respectively. The absolute density of H radicals was measured by VUVLAS. The crystallinity factor, preferential orientation, defect density, microstructure, and the post-deposition oxidation of deposited Si thin films were investigated by Raman spectroscopy, XRD, ESR, TEM and FTIR, respectively. From these results, the following features of the RI-system were determined:

1. The density of H radicals in RI-CCP was ca. 1.4 times higher than that in C-CCP at the same electron density ($5.5 \times 10^{12} - 8.3 \times 10^{12} \text{ cm}^{-3}$).
2. A crystallinity factor of 0.6 was achieved under a low electron density ($4.1 \times 10^{10} \text{ cm}^{-3}$).
3. Si thin film deposited with RI-CCP showed weak $\langle 110 \rangle$ preferential orientation ($I(220)/I(111)=0.9$).
4. The defect density by crystallization with RI-CCP is lower than that with C-CCP ($5.1 \times 10^{16} \text{ cm}^{-3}$).
5. There were less voids in the films deposited with RI-CCP, and therefore less post-deposition oxidation.
6. RI-CCP can deposit crystallized Si thin films at higher deposition rate than C-CCP.
7. $\mu\text{c-Si:H}$ films deposited by RI-CCP have good photosensitivity of the order of 10^2 .

Chapter 5

The high performance of RI-CCP for the deposition of Si thin films for solar cell devices has been demonstrated. As a first step, the RI-PECVD system was constructed with one power supply of 60 MHz, which is divided into two regions, so that equipment costs and size could be kept down. This equipment is a novel system for the fabrication of $\mu\text{c-Si:H}$ films for solar cell devices. Furthermore, the results obtained in this study should be useful and give the guideline from viewpoints of basic and applied research for the development of high quality films.

5.5 References

- ¹J. Meier, R. Flückiger, H. Keppner, and A. Shah, *Appl. Phys. Lett.* **65**, 860 (1994).
- ²H. Keppner, J. Meier, P. Torres, D. Fischer, and A. Shah, *Appl. Phys. A* **69**, 169 (1999).
- ³K. Yamamoto, T. Suzuki, M. Yoshimi, and A. Nakajima, *Jpn. J. Appl. Phys.* **36**, L569 (1997).
- ⁴A. Matsuda, *J. Non-Cryst. Solids* **338-340**, 1 (2004).
- ⁵Y. Toyoshima, K. Arai, A. Matsuda, and K. Tanaka, *Appl. Phys. Lett.* **56**, 1540 (1990).
- ⁶C. C. Tsai, G. B. Anderson, R. Thompson, and B. Wacker, *J. Non-Cryst. Solids* **114**, 151 (1989).
- ⁷F. Kaïl, A. F. I. Morral, A. Hadjadj, P. R. I. Cabarrocas, and A. Beorchia, *Philos. Mag.* **84**, 595 (2004).
- ⁸K. Nakamura, K. Yoshino, S. Takeoka, and I. Shimizu, *Jpn. J. Appl. Phys.* **34**, 442 (1995).
- ⁹L. Guo, M. Kondo, M. Fukawa, K. Saitoh, and A. Matsuda, *Jpn. J. Appl. Phys.* **37**, L1116 (1998).
- ¹⁰M. Kondo, M. Fukawa, L. Guo, and A. Matsuda, *J. Non-Cryst. Solids* **266-269**, 84 (2000).
- ¹¹U. Graf, J. Meier, U. Kroll, J. Bailat, C. Droz, E. Vallat-Sauvain, and A. Shah, *Thin Solid Films* **427**, 37 (2003).
- ¹²M. Fukawa, S. Suzuki, L. Guo, M. Kondo, and A. Matsuda, *Sol. Energy Mater. Sol. Cells* **66**, 217 (2001).
- ¹³A. Gordijn, M. Vanecek, W. J. Goedheer, J. K. Rath, and R. E. I. Schropp, *Jpn. J. Appl. Phys.* **45**, 6166 (2006).
- ¹⁴Y. Sobajima, S. Nakano, T. Toyama, and H. Okamoto, *Jpn. J. Appl. Phys.* **46**, L199 (2007).
- ¹⁵M. Kondo, *Sol. Energy Mater. Sol. Cells* **78**, 543 (2003).

- ¹⁶M. Hiramatsu, K. Shiji, H. Amano, and M. Hori, *Appl. Phys. Lett.* **84**, 4708 (2004).
- ¹⁷K. Shiji, M. Hiramatsu, A. Enomoto, M. Nakamura, H. Amano, and M. Hori, *Diamond Relat. Mater.* **14**, 831 (2005).
- ¹⁸S. Kondo, M. Hori, K. Yamakawa, S. Den, H. Kano, and M. Hiramatsu, *J. Vac. Sci. Technol. B* **26**, 1294 (2008).
- ¹⁹W. Takeuchi, M. Ura, M. Hiramatsu, Y. Tokuda, H. Kano, and M. Hori, *Appl. Phys. Lett.* **92**, 213103 (2008).
- ²⁰G. Neumann, U. Bänziger, M. Kammeyer, and M. Lange, *Rev. Sci. Instrum.* **64**, 19 (1993).
- ²¹A. Matsuda and K. Tanaka, *Thin Solid Films* **92**, 171 (1982).
- ²²T. Nishimoto, M. Takai, H. Miyahara, M. Kondo, and A. Matsuda, *J. Non-Cryst. Solids* **299-302**, 1116 (2002).
- ²³G. Dingemans, M. N. van den Donker, D. Hrunski, A. Gordijn, W. M. M. Kessels, and M. C. M. van de Sanden, *Appl. Phys. Lett.* **93**, 111914 (2008).
- ²⁴C. Droz, E. Vallat-Sauvain, J. Bailat, L. Feitknecht, J. Meier, and A. Shah, *Sol. Energy Mater. Sol. Cells* **81**, 61 (2004).
- ²⁵K. Saito and M. Kondo, *Phys. Status Solidi A* **207**, 535 (2010).
- ²⁶H. Kakinuma, M. Mohri, M. Sakamoto, and T. Tsuruoka, *J. Appl. Phys.* **70**, 7374 (1991).
- ²⁷L. Houben, M. Luysberg, P. Hapke, R. Carius, F. Finger, and H. Wagner, *Philos. Mag. A* **77**, 1447 (1998).
- ²⁸K. Murata, M. Ito, M. Hori, and T. Goto, *J. Vac. Sci. Technol. B* **17**, 1098 (1999).
- ²⁹B. Kalache, A. I. Kosarev, R. Vanderhaghen, and P. R. i Cabarrocas, *J. Appl. Phys.* **93**, 1262 (2003).
- ³⁰O. Vetterl, F. Finger, R. Carius, P. Hapke, L. Houben, O. Kluth, A. Lambertz, A. Mück, B. Rech, and H. Wagner, *Sol. Energy Mater. Sol. Cells* **62**, 97 (2000).

Chapter 6 Conclusions and Future Works

6.1 Conclusions of present research

The motivation of this thesis is understanding the relation between behaviors of radicals in plasma and properties of deposited $\mu\text{-Si:H}$ thin films and the development of high-rate deposition method of $\mu\text{-Si:H}$ thin films. We have estimated the flux of H and SiH_3 radicals from the measurement of the absolute density and investigated the relation between the flux and film structure. This study has also developed H radical injection (RI) plasma enhanced chemical vapor deposition for a high-rate deposition of $\mu\text{-Si:H}$ thin films.

In Chapter 1, the trend in solar cells has been shown as introduction: the thin-film silicon solar cells, plasma process and previous studies of plasma diagnostics were also introduced. Purposes and overview of this thesis were also described.

In Chapter 2, theories of plasma diagnostics such as VUVAS, VUVLAS, CRDS and microwave interferometer were described. Theories of film characterization technique such as Raman spectroscopy, X-ray diffraction (XRD), Fourier transform infrared absorption spectroscopy (FTIR), Electron spin resonance (ESR), and Transmission electron microscopy (TEM) used as measurement methods of silicon thin film were introduced.

In Chapter 3, the surface loss probability of H radicals in SiH_4/H_2 plasma afterglow was investigated using VUVAS. The decay of H radicals in the afterglow plasma was measured and the diffusion lifetime was calculated by considering the reaction between H radicals and SiH_4 molecules. The surface loss probability was estimated from the diffusion lifetime and was higher in the SiH_4/H_2 mixture plasma than in H_2 pure plasma and increased with increasing SiH_4 flow rate. The surface condition was investigated by analyzing the deposition rate and the crystallinity of silicon thin

films deposited on the chamber wall. On the basis of these results and with consideration of the reactions on the surface, it was concluded that deposition species such as SiH_3 radicals generated from SiH_4 influence the surface loss probability of H radicals. Furthermore, the density of H radicals was significantly decreased by heating the chamber wall. Surface reactions are enhanced by heating and the surface loss probability is ca. 1 at 473 K.

In Chapter 4, the flux ratio of H radicals to precursor deposited as a film in SiH_4/H_2 plasma was investigated using a tunable VUVLAS. The absolute density of H radicals was $5.5 \times 10^{12} \text{ cm}^{-3}$ and the translational temperature was around 770 K. The flux of H radicals was estimated to be $5.7 \times 10^{17} \text{ cm}^{-2} \text{ s}^{-1}$ from quantitative measurements. The flux of precursor deposited as a film was estimated to be in the order of $10^{15} - 10^{16} \text{ cm}^{-2} \text{ s}^{-1}$. The critical flux ratio to obtain film properties suitable for the i-layer of a solar cell was found to be approximately 65–70. Moreover, the ratio of SiH_3 radicals in the flux of film precursors was estimated to be 45%. These results indicate that the range of the flux ratio of H radicals to film precursors to obtain suitable film properties is very narrow and the 65–70 times higher flux of H radicals than film precursors is necessary. Therefore, achieving the sufficient H radical density is crucial issue for the high-rate deposition of $\mu\text{c-Si:H}$. In the case of high pressure condition, not only SiH_3 radicals but also high order radicals seem to be predominant precursors.

In Chapter 5, RI-PECVD system excited by a 60 MHz was proposed for the fabrication of Si thin films for solar cell devices to achieve selective enhancement of the H radical densities for crystallization of the films under low depletion of SiH_4 . The plasma parameters and film growth characteristics of RI-CCP were compared with C-CCP. The electron density and temperature were measured using a microwave interferometer and by optical emission spectroscopy, respectively. The absolute density of H radicals was measured by VUVLAS. The crystallinity factor, preferential orientation, defect density, microstructure, the post-deposition oxidation, and the photo

Chapter 6

sensitivity of deposited Si thin films were investigated by Raman spectroscopy, XRD, ESR, TEM, FTIR, and solar simulator, respectively. From these results, the high performance of RI-CCP for the high-rate deposition of Si thin films has been demonstrated. As a first step, the RI-system was constructed with one power supply of 60 MHz, which is divided into two regions, so that equipment costs and size could be reduced. This equipment is a novel system for the fabrication of $\mu\text{c-Si:H}$ films for solar cell devices. Furthermore, the results obtained in this study should be useful and give the guideline from viewpoints of basic and applied research for the development of high quality films.

6.2 Scopes for future works

In this thesis, the behaviors of H and SiH₃ radicals in gas phase and relation of them and film property of $\mu\text{c-Si:H}$ were studied based on plasma diagnostics and high-rate deposition method was developed based on controlling radicals by using H radical-injection (RI) system.

In Chapter 3, the surface loss probability of H radicals in SiH₄/H₂ plasma afterglow was investigated using VUVAS. The surface loss probability increased with increasing SiH₄ and the surface temperature. From these results, we have confirmed that the reaction probability of H radicals on the deposition surface is almost unity. Moreover, it is important to control the temperature of the chamber wall for high density of H radicals. The quantitative results for the surface loss probability of H radicals obtained in this study are important to not only understand plasma-surface reactions, but also contribute to improvements in the control of plasma processing and the design of equipment.

In Chapter 4, the flux ratio of H radicals to precursor deposited as a film in SiH₄/H₂ plasma was investigated using a tunable VUVLAS. The critical flux ratio to obtain film properties of $\mu\text{c-Si:H}$ suitable for the i-layer of a solar cell was found to be approximately 65–70. This result will be useful for the design of equipment using plasma simulation. However, other plasma species such as Si_xH_y ions and radicals would help our farther understanding. *In situ* film characterization such as FTIR and spectroscopic ellipsometry would also give important information. From these results, the mechanism of $\mu\text{c-Si:H}$ deposition will be completely clarified.

In Chapter 5, RI-PECVD system excited by a 60 MHz was proposed for the fabrication of Si thin films for solar cell devices to achieve selective enhancement of the H radical densities for crystallization of the films under low depletion of SiH₄. Effects of RI-system on increase in H radicals and enhancing crystallization have been

demonstrated. It was found that the deposition rate can be increased with keeping film property using RI-system. However, the magnitude of increase of H radicals is still 1.4 times. As a future works, the RI-system will be improved to obtain much higher H radical density. If higher H radical density is realized, higher deposition rate would be also obtained. The photovoltaic property of $\mu\text{-Si:H}$ deposited by RI-PECVD has not been evaluated. The information of the photovoltaic property must be feedback to the development of RI-system.

It is very important to obtain the behaviors of activated species in reactive plasmas for realizing high quality and high rate deposition process. However, in order to measure the activated species quantitatively, some specialized equipments such as laser systems are necessary and expensive at the present, and difficult to be applied to every plasma processes. Therefore, novel plasma monitoring techniques and apparatuses with simple and easy use should be developed to measure activated species at any plasma equipment for the future. These techniques would realize the deep understanding of the deposition processes and development of plasma equipment which can deposit high-quality silicon thin films at high deposition rates.

Acknowledgements

The present research has been performed in Prof. Hori and Prof. Sekine Laboratory, Department of Electrical Engineering and Computer Science, Nagoya University. The research results presented in this thesis could not have been obtained without the support of the following people.

First and foremost, I would like to express my deep appreciation to Prof. Masaru Hori, Department of Electrical Engineering and Computer Science, Nagoya University, for having given me the opportunity to pursue a Ph.D. in his group. I could not progress rapidly in my understanding of this research without his guidance, valuable advices, and encouragements. I would also like to deeply appreciate my co-supervisor, Prof. Makoto Sekine, Plasma Nanotechnology Research Center, Nagoya University, for providing his wealth of experience and wonderful discussions. At same time, I wish to express my sincere gratitude to the vice-adviser, Prof. Hirotaka Toyoda, Department of Electrical Engineering and Computer Science, Nagoya University, for his valuable suggestions and discussions in progressing this research. I also thank to the vice-adviser, Prof. Shigeaki Zaima, Department of Department of Crystalline Materials Science, Nagoya University, for giving the big motivation for the passionate research.

I am also grateful to the entire staff in Hori and Sekine's Lab., Prof. Kenji Ishikawa, Associate Prof. Hiroki Kondo, Associate Prof. Satomi Tajima, Assistant Prof. Keigo Takeda, Dr. Noboru Ebizuka, Dr. Fengdong Jia, Dr. Hiromasa Tanaka, Dr. Jagath Kularatne, Dr. Jerome Jolibois, and Ms. Hiroko Mizuno for their fruitful discussion and valuable comments. I would like to express my gratitude to Prof. Masafumi Ito, Department of Electrical and Electronic Engineering, Meijo University, Prof. Mineo Hiramatsu, Department of Electrical and Electronic Engineering, Meijo University, Associate Prof. Takayuki Ohta, Department of Electrical and Electronic Engineering, Meijo University, Dr. Seigo Takashima, Plasma Center for Industrial Applications, Dr.

Masaru Izawa, Hitachi High-Technologies Corporation, Dr. Masanaga Fukasawa, Sony corporation, and Kei Hattori, Toshiba corporation.

I would like to acknowledge Dr. Shoji Den, Dr. Koji Yamakawa, and Dr. Shunji Takahashi in Katagiri Engineering Co., Ltd., Dr. Hiroyuki Kano in NU Eco-Engineering Co., Ltd., for constructing and modifying the experimental equipments.

I am indebted to Dr. Ikuo Sawada, Dr. Masaaki Matsukuma, and Dr. Takashi Matsumoto in Tokyo Electron Ltd., for collaborating and giving regular and valuable advices.

I am deeply grateful to Dr. Shota Nunomura in National Institute of Advanced Industrial Science and Technolory, for collaborating and giving useful advices and encouragements.

I appreciate Prof. Uwe Czarnetzki, Ruhr University Bochum, for giving me the opportunity to study in her group. His guidance and valuable advices allowed me to progress in my understanding on plasma physics. I would like to appreciate deeply Mr. Edmund Schüngel and Dr. Shinya Iwashita for collaborating and giving valuable advices. A big thanks to all members of Prof. Czarnetzki's group.

I appreciate Prof. Bill Graham, Queen's University Belfast, for giving me the opportunity to study in her group. His guidance and valuable advices allowed me to progress in my understanding on plasma physics. I would like to appreciate deeply Mr. Wameedh Adress for collaborating and giving valuable advices. A big thanks to all members of Prof. Graham's group.

I have warm thanks to Prof. Makoto Konagai and all members in his group, Tokyo Institute of Technology, for giving me the opportunity to discuss and much useful advice.

The author thanks sincerely Mr. Lee Myung Ryong, Mr. Sho Kawashima, Ms. Ya Lu, Mr. Atsushi Fukushima, Mr. Keita Miwa, and Dr. Youn Joon Kim who aided their experimental works carried out in this thesis and also expressed their valuable

suggestions and discussions.

A big thanks to my colleagues in Prof. Hori and Prof. Sekine's Lab, Dr. Saburo Uchida, Dr. Masahiro Iwasaki, Dr. Wakana Takeuchi, Dr. Chang Soon Moon, Dr. Shingo Kondo, Dr. Tsuyoshi Yamaguchi, Dr. Hirotohi Inui, Dr. Hiroshi Yamamoto, Dr. Arkadiusz Malinowski, Mr. Eiji Takahashi, Mr. Hajime Sasaki, Mr. Satoshi Kono, Mr. Shigetoshi Maruyama, Mr. Takuma Machino, Mr. Tomomi Obayashi, Ms. Emi Shibata, Mr. Masayoshi Kashihara, Mr. Kenichi Ando, Ms. Sachiko Iseki, Mr. Tetsuya Kimura, Mr. Hiroki Kuroda, Mr. Hiroyuki Mikuni, Mr. Kota Mase, Mr. Yuto Matsudaira, Dr. Shang Chen, Mr. Hyung Jun Cho, Mr. Hitoshi Watanabe, Mr. Takuya Takeuchi, Mr. Yudai Miyawaki, Mr. Takehiro Hiraoka, Mr. Lu Yi, Mr. Tokushige Kino, Mr. Yoshihiro Itani, Mr. Toshiyuki Kuroda, Mr. Hironao Shimoeda, Mr. Toshiya Suzuki, Mr. Koji Yasuda, Mr. Leyong Yu, Mr. Masanori Kato, Mr. Naoya Sumi, Mr. Tatsuya Hagino, Mr. Shinpei Amasaki, Mr. Takayuki Kanda, Mr. Yusuke Kondo, Mr. Minyoung Ahn, Mr. Kohei Asano, Mr. Jun Kuki, Mr. Ryosuke Kometani, Mr. Takeyoshi Horibe, Mr. Tomohiro Takahashi, Mr. Jiadong Cao, Mr. Kuangda Sun, Mr. Makoto Isobe, Mr. Takashi Kako, Mr. Ryo Gonda, Mr. Masayuki Nakamura, Mr. Hiroki Nagano for giving the big pleasure in life and creating a most enjoyable work atmosphere. I also appreciate the enough secretarial supports to Ms. Tomoko Yokoi, Ms. Rie Nozaki, Ms. Megumi Oshigane, Ms. Azusa Ohta, Ms. Mitsuko Era, Ms. Rie Kamiya, Ms. Masakot Takahashi, and Ms. Naoko Kataoka for helping me to concentrate on the research without any problem of administrative task.

Finally, I would like to dedicate this thesis to my parents, my brothers, and good friends.

Yusuke Abe

January 2013

List of Papers

1. Original Paper

	Title	Jounal	Authors
1	Dependence of Surface-Loss Probability of Hydrogen Atom on Pressures in Very High Frequency Parallel-Plate Capacitively Coupled Plasma	Applied Physics Express, 3 , 106001 (2010).	Y. Abe, S. Kawashima, K. Takeda, M. Sekine, M. Hori (Chapter 4)
2	Critical flux ratio of hydrogen radical to film precursor in microcrystalline silicon deposition for solar cells	Applied Physics letters, 101 , 172109 (2012).	Y. Abe, A. Fukushima, K. Takeda, H. Kondo, K. Ishikawa, M. Sekine, M. Hori (Chapter 4)
3	Surface loss probability of H radicals on silicon thin films in SiH ₄ /H ₂ plasma	Journal of Applied Physics, 113 , 013303 (2013).	Y. Abe, A. Fukushima, K. Takeda, H. Kondo, K. Ishikawa, M. Sekine, M. Hori (Chapter 3)

List of papers

	Title	Jounal	Authors
4	Impact of hydrogen radical-injection plasma on fabrication of microcrystalline silicon thin film for solar cells	Journal of Applied Physics, 113 , 033304 (2013)	Y. Abe, S. Kawashima, A. Fukushima, Y. Lu, K. Takeda, H. Kondo, K. Ishikawa, M. Sekine, M. Hori (Chapter 5)
5	Behaviors of H and SiH ₃ radicals in deposition of microcrytalline silicon	Journal of Applied Physics (to be Submitted)	Y. Abe, A. Fukushima, K. Takeda, H. Kondo, K. Ishikawa, M. Sekine, M. Hori (Chapter 4)

2. International Conferences

	Title	Conference	Authors
1	Absolute density and translational temperature of hydrogen atoms in the high pressure VHF capacitively coupled plasma	The IUMRS International Conference in Asia 2008, QP-28, Nagoya, Japan, December 9-13, 2008.	Y. Abe, K. Takeda, M. Sekine, M. Hori
2	Behaviors of H atoms in VHF plasma for flexible electronics	The 8 th International Workshop of Advanced Plasma Processing and Diagnostics Joint Workshop with Plasma Application Monodzukuri, Gifu, Japan, Jan. 20-21, 2009.	Y. Abe, K. Takeda, M. Sekine, M. Hori
3	Measurements of Absolute Density and Translational Temperature of Hydrogen Atoms in the High Pressure VHF Capacitively Coupled Plasma	The 2nd International Conference on Plasma-Nano Technology & Science, P-44, Nagoya, Japan, Jan. 22-23, 2009.	Y. Abe, K. Takeda, M. Sekine, M. Hori
4	Absolute Density of Hydrogen Atoms in the High Pressure VHF Capacitively Coupled Plasma for Solar Cell Devices	1st International Symposium on Advanced Plasma Science and its Applications, Mo-5, p. 135, Nagoya, Japan, Mar. 8-11, 2009.	Y. Abe, S. Kawashima, K. Takeda, M. Sekine, M. Hori
5	Behaviors of hydrogen atoms in SiH ₄ /H ₂ plasma for solar cell devices	Memorial Symposium for the Retirement of Professor Tachibana (ISPC-19 Pre-Symposium in Japan), Poster session 15, Kyoto, Japan, May 30, 2009.	Y. Abe, S. Kawashima, K. Takeda, M. Sekine, M. Hori

List of papers

	Title	Conference	Authors
6	Behavior of hydrogen atoms in plasma enhanced chemical vapor deposition of microcrystalline silicon film	62nd Annual Gaseous Electronics Conference, GT3 6, p. 25, Saratoga Springs, New York, USA, October 20-23, 2009.	Y. Abe, S. Kawashima, K. Takeda, M. Sekine, M. Hori
7	Surface Loss Probabilities of H Atom on Various Silicon Thin Films	2nd International Symposium on Advance Plasma Science and its Application, PA015A, p. 124, Nagoya Japan, Mar. 7-10, 2010.	Y. Abe, Chang S. Moon, S. Kawashima, K. Takeda, H. Kondo, K. Ishikawa, M. Sekine, M. Hori
8	Measurement of surface loss probabilities of hydrogen radicals in plasma-enhanced Si CVD process for solar cell	63rd Gaseous Electronics Conference & 7th International Conference on Reactive Plasmas, SF3 5, p. 160, Paris, France, Oct. 4-8, 2010.	Y. Abe, K. Takeda, K. Ishikawa, H. Kondo, M. Sekine, M. Hori
9	Surface Loss Probability of Hydrogen Radical in SiH ₄ /H ₂ Plasma	3rd International Symposium on Advanced Plasma Science and its Applications for Nitrides and Nanomaterials, P2-001A, p. 97, Nagoya, Japan, Mar. 6-9, 2011.	Y. Abe, K. Takeda, K. Ishikawa, H. Kondo, M. Sekine, M. Hori
10	Crystallinity control of microcrystalline silicon film employing hydrogen radical-injection Plasma-enhanced chemical vapor deposition	3rd International Symposium on Advanced Plasma Science and its Applications for Nitrides and Nanomaterials, P4-002A, p. 177, Nagoya, Japan, Mar. 6-9, 2011.	S. Kawashima, Y. Abe, K. Takeda, K. Ishikawa, H. Kondo, M. Sekine, M. Hori

List of papers

	Title	Conference	Authors
11	Surface reaction of hydrogen radical on plasma enhanced chemical vapor deposition of silicon thin films	30th International Conference on Phenomena in Ionized Gases, D13-6, Belfast, United Kingdom, Aug. 28-Sep. 2, 2011.	Y. Abe, K. Takeda, M. Hori, K. Ishikawa, H. Kondo, M. Sekine
12	Effect of Hydrogen Radical Injection on Growth Property and Crystallinity of Microcrystalline Silicon Thin Film	2011 International Conference on Solid State Devices and Materials, L-2-6, pp. 1359-1360, Nagoya, Japan, Sep. 27-30, 2011.	Y. Abe, A. Fukushima, Y. Lu, K. Takeda, H. Kondo, K. Ishikawa, M. Sekine, M. Hori
13	Behavior of radicals in SiH ₄ /H ₂ plasma for fabrication of solar cell using silicon thin film	64th Annual Gaseous Electronics Conference, ET1 4, p. 24, Salt Lake City, Utah, USA, Nov. 14-18, 2011.	Y. Abe, A. Fukushima, Y. Lu, K. Takeda, H. Kondo, K. Ishikawa, M. Sekine, M. Hori
14	Relationship between Radicals in Gas Phase and Film Property of Silicon Thin Films in SiH ₄ /H ₂ plasma CVD	15th International Conference on Thin Films, P-S2-01, p. 50, Kyoto, Japan, Nov. 8-11, 2011.	A. Fukushima, Y. Abe, K. Takeda, H. Kondo, K. Ishikawa, M. Sekine, M. Hori
15	Loss kinetics of hydrogen radicals in silane plasma	4th International Symposium on Advanced Plasma Science and its Applications for Nitrides and Nanomaterials, P2009A, p. 129, Nagoya, Japan, Mar. 4-8, 2012.	Y. Abe, A. Fukushima, K. Takeda, H. Kondo, K. Ishikawa, M. Sekine, M. Hori

List of papers

	Title	Conference	Authors
16	Relationship between silicon thin film property and flux ratio of H radical to silicon growth precursor in SiH ₄ /H ₂ plasma CVD	4th International Symposium on Advanced Plasma Science and its Applications for Nitrides and Nanomaterials, 5p-A040A, p. 7, Nagoya, Japan, Mar. 4-8, 2012.	A. Fukushima, Y. Abe, K. Takeda, H. Kondo, K. Ishikawa, M. Sekine, M. Hori
17	Relationship between Silicon Thin Film Property and Flux Ratio of H Radical in SiH ₄ /H ₂ Plasma CVD	5th International Conference on PLASMA-NanoTechnology & Science, P-60, Aichi, Japan, Mar. 9-10, 2012.	A. Fukushima, Y. Abe, K. Takeda, H. Kondo, K. Ishikawa, M. Sekine, M. Hori
18	The Effect of the Deposition Rate of Microcrystalline Silicon Deposition Using a Hydrogen Radical Injection Plasma Source	5th International Conference on PLASMA-NanoTechnology & Science, P-61, Aichi, Japan, Mar. 9-10, 2012.	Y. Lu, A. Fukushima, Y. Abe, Y. J. Kim, K. Takeda, K. Ishikawa, H. Kondo, M. Sekine, M. Hori
19	Spectroscopic Determination of Radical Densities in SiH ₄ /H ₂ Plasma	The 11th Asia Pacific Conference on Plasma Science and Technology and 25th Symposium on Plasma Science for Materials, 1-P19, p. 137, Kyoto, Japan, Oct. 2-5, 2012.	Y. Abe, A. Fukushima, Y. Lu, Y. Kim, K. Takeda, H. Kondo, K. Ishikawa, M. Sekine, M. Hori
20	Evaluation of Relationship between $\mu\text{c-Si}$ Film Property and Flux Ratio of H Radicals to Film Precursors	The 11th Asia Pacific Conference on Plasma Science and Technology and 25th Symposium on Plasma Science for Materials, 2Gr-O07, p. 28, Kyoto, Japan, Oct. 2-5, 2012.	A. Fukushima, Y. Abe, Y. Lu, K. Takeda, H. Kondo, K. Ishikawa, M. Sekine, M. Hori

List of papers

Title	Conference	Authors
21 Microcrystal Orientation of Silicon Thin Film Deposited with Hydrogen Radical Injection Plasma Enhanced CVD	The 11th Asia Pacific Conference on Plasma Science and Technology and 25th Symposium on Plasma Science for Materials, 2-P14, p. 253, Kyoto, Japan, Oct. 2-5, 2012.	Y. Lu, A. Fukushima, Y. Abe, Youn J. Kim, K. Takeda, K. Ishikawa, H. Kondo, M. Sekine, M. Hori
22 High performances of microcrystalline Si thin film formation for a solar cell by measurement and control of hydrogen radicals in the SiH ₄ /H ₂ plasma	34th International Symposium on Dry Process, E-2, pp. 41-42, Tokyo, Japan, Nov. 15-16, 2012.	Y. Abe, A. Fukushima, Y. Lu, Youn J. Kim, K. Takeda, H. Kondo, K. Ishikawa, M. Sekine, M. Hori

3. Research Project

- International Training Program (Program for incubating young researchers on plasma nanotechnology materials and device processing, conducted by Japan Society for the Promotion of Science) in Ruhr University Bochum, Bochum, Germany, from October to November, 2010.
- International Training Program (Program for incubating young researchers on plasma nanotechnology materials and device processing, conducted by Japan Society for the Promotion of Science) in Queen's University Belfast, Belfast, United Kingdom, from January to March, 2012.